INNOVATIONS IN ALIGNED AND OVERMOLDED LONG FIBER THERMOPLASTIC COMPOSITES

A Dissertation Presented for the

Doctor of Philosophy

Degree

The University of Tennessee, Knoxville

Shailesh P. Alwekar

December 2021

DEDICATION

I dedicate my dissertation work to my professors, and friends who shared their words of advice and encouragement to finish this study. A special feeling of gratitude to my beloved parents who continually provide their moral, spiritual, emotional, and financial support. To my beloved wife, Seema, for her eternal love and support. I wish to express my heartfelt love to my little girls Aayushi and Aarya for coping with the undue paternal deprivation during my study. Most of all to Almighty God, who always give me guidance, strength, power of mind, knowledge, and wisdom in everything I do.

ACKNOWLEDGEMENTS

First and foremost, I would like to express my sincere and heartfelt gratitude to my supervisor, Dr. Uday K. Vaidya, for his expert advice, guidance, encouragement, for being the supportive, insightful, and wonderful human being that he is, without whom this PhD journey would not have been possible. His personality, work style, and mentoring has always inspired me and helped me not only to become more independent and develop professionally, but also has influenced me to become a better person. I have been extremely lucky to have such a supervisor who has provided better level of support, flexibility, and guidance during different phases of this journey.

Further, I would like to thank my dissertation committee, Dr. Chad E. Duty, Dr. Amit K. Naskar, and Dr. Kenneth D. Kihm, for their great support and allowing me to use their facilities for my thesis work. I would like to extend my sincere thanks to Seokpum Kim, Ahmed Arabi Hassen, Vipin Kumar, David Nuttall, and Vlastimil Kunc at the Manufacturing Demonstration Facility, ORNL for all the insightful discussions, ideas, and the wealth of knowledge they shared on modeling, non-destructive, and processing techniques. I would also like to thank Stephen A. Fore from American Renolit Corporation and Anthony Ciringione from Concordia Fibers for material support.

I would like to thank Stephen Young, JC Chin, and Josh Crabtree at the university of Tennessee for assisting me with experimental testing at SERF. I would like to thank Stephen Sheriff, and Vanina Ghossein at the Fibers and composites manufacturing facility for their assistance and support. Special thanks to my lab mates Caleb weatherly, Ryan Ogle, Alexander Haug, Ryan Spencer, and Pritesh Yeole for their timely help with sample preparation, characterization, and insightful discussions. I would also like to thank my current and past fellow graduate students and friends who have given more than can be expressed, especially Benjamin Willis, Nitilaksha Hiremath, Hicham Ghossein, Kaustubh Mungale, Saurabh Pethe, Vidya Hiremath, Alex Stiles, and Surbhi Kore.

I am greatly appreciated for the funding support and resources that were provided by the US Department of Energy (DOE), Institute for Advanced Composites Manufacturing Innovation (IACMI), Manufacturing Demonstration Facility (MDF), Oak Ridge National Laboratory (ORNL) and University of Tennessee.

None of this would have been possible without the love and support from my pillars of strength in life, my mother Ranjana Alwekar, my father Pandurang Alwekar, my father-in-law Pratap Genjage, and my mother-in-law Pratibha Genjage for their love, motivation support, encouragement, patience, sacrifice, and confidence in me. I am extremely thankful to my dearest wife, Seema Alwekar, who has always been there for me during all the ups and downs in my life. I am thankful for her love, support, constructive criticism, which has been helping me to learn more and grow both professionally and as a person.

ABSTRACT

Long fiber thermoplastic (LFT) composite materials are increasingly used in high performance lightweight automotive, sporting, and industrial applications. LFT composites are processed with extrusion-compression molding (ECM) and/or injection molding (IM). Melt extrusion offers unique opportunities to align long fibers in a thermoplastic polymer melt. The properties of LFT materials are highly influenced by processing techniques which leads to different porosity content, fiber length distribution, and fiber orientation distribution. Hence, it is important to understand the various LFT processing techniques and their effect on mechanical, thermal, and microscopic properties.

The fundamental process-property relationships in LFT composites are investigated in this dissertation. Additionally, there is a genuine need for efficient and reliable composite manufacturing techniques which can provide reduced weight, superior crashworthiness, improved efficiency, reduced processing complexity and cost-effective structures.

The aim of this work is to explore aligned long fibers and enhance the performance of long fiber composites through innovations in overmolding process. The overmolding approach offers an efficient alternative process to traditional sheet molding compound (SMC), glass mat thermoplastic (GMT), and rib reinforced thermoplastic composites.

In this work, aligned LFT sheets processed via melt extrusion with continuous fiber like properties were considered. Additionally, LFTs are processed utilizing extrusion compression molding (ECM) process, and overmolded with continuous fiber reinforcement to evaluate the structural performance. The melt extruded and overmolded

LFT samples were characterized using nondestructive and destructive techniques to evaluate fiber alignment, fiber distribution, manufacturing defects, interfacial bonding, and the effect of continuous reinforcement on LFT composite.

Keywords: Long fiber thermoplastic, Extrusion compression molding, Filament winding Destructive testing, Non-destructive testing, Computational modeling

TABLE OF CONTENTS

LIST OF TABLES

LIST OF FIGURES

1. CHAPTER 1

INTRODUCTION

1.1 Motivation

Long fiber thermoplastics (LFTs) are discontinuous fiber thermoplastic intermediates that bridge the gap between short (< 3mm) and continuous fiber reinforced thermoplastic composites. LFT composites provide ease of processability, recyclability, and possess superior specific modulus and strength, excellent impact resistance, excellent corrosion resistance, and infinite shelf life. These advantages enable their increasing use in various applications and make LFT composites one of the most advanced lightweight engineering materials[1].

LFTs typically comprise fibers of 3 mm to 25.4 mm in length and reinforced with a variety of crystalline and amorphous thermoplastic polymers [2]. LFT have fiber aspect ratios (length/diameter) varying from 300 to 2000 [3]. LFT possesses the fiber length above the critical fiber length which is necessary for effective strengthening and stiffening of LFT composites. The critical fiber length (l_c) is defined by Eq. (1.1) [4].

$$l_{\mathrm{c}} = \frac{\sigma_{max} * d}{2\tau} \qquad \text{(Eq 1.1)}$$

where σ_{max} is tensile stress acting on the fiber, d is fiber diameter and τ is interfacial shear strength.

As seen from Equation (1.1), the strength of the LFTs is related to the critical fiber length. However, stiffness depends typically on the fiber content and fiber alignment present in the composite. Typically, LFTs processed utilizing extrusion compression molding (ECM) results in randomly oriented (based on mold geometry and charge location) and LFTs processed utilizing melt extrusion results in alignment with continuous fiber-like properties [5].

Although LFT composites with high mechanical, thermal, and functional properties have been developed and characterized, there is still a lack of understanding the process-microstructure-property relationships and mechanisms. This dissertation investigates LFT processing techniques (ECM, aligned extrusion) and their effect on mechanical, thermal, and microscopic properties.

Even though, perfectly aligned LFTs implement continuous fiber-like properties, it is usually laborious to perfectly align fibers in LFT composite utilizing aligned extrusion process. Therefore, partial fiber alignment is typical in any molded LFT composite [6]. Moreover, there is a genuine need for an efficient as well as a reliable composite manufacturing technique which can provide improvement over the imposed loads without considerable increase in weight, superior crashworthiness, improved efficiency, reduced processing complexity and compelling cost element for structural and semi-structural applications. Therefore, this project also proposes innovative overmolding approach which is a hybrid process that utilizes pre-consolidated continuous fiber-reinforced thermoplastic (CFRTP) tapes/commingled fibers and extrusion-compression molded LFTs. The proposed study will improve our understanding of the process and its relationship with microstructure and associated properties.

1.2 LFT Pellets Fabrication Process and its Market

The highly viscous thermoplastic polymers even though it is melted, makes it challenging to impregnate fibers and mold the final product in a one-step process. Hence, an intermediate form, generally pre-impregnate pellets manufacturing prior the final product. LFT pellets are typically manufactured by hot melt impregnation [7]. In the hot-melt impregnation process, continuous fiber tows are pulled under tension into an extrusion die, where the dry fibers are impregnated with an extruded thermoplastic polymer. The material is then cooled rapidly as it exits the die, pulled, and pelletized to desired pellet length [8]. Hartness et al. [7] reported the details of LFT pellet production utilizing hot melt impregnation line. The impregnation line is comprised of a fiber creel with a tension control, impregnation die which uses thermoplastic polymer to impregnate, Cooled rollers to cool the prepreg, a puller than control the line speed, and pelletizer that chops the continuous rod into desired pellet size, typically 3–25.4 mm (0.12”–1”). Figure 1.1 shows the hot melt impregnation process line for manufacturing LFT pellets.

In global market, LFT production has experienced rapid growth from year 2004 to 2009 of total 137 million kg with an annual growth rate of 18% [9]. According to market survey published in Apr 2020, it is estimated that the LFT global market will grow from USD 2.8 billion to USD 4.6 billion by year 2025 at an annual growth rate of 10.5% due to its extensive use in automotive, electronics industries [10]. It is estimated that polypropylene (PP) based LFTs have 65% of the global market share. Polyamide (PA) based LFTs have about 20% of the market share and the remaining 15% is comprised of other polymer systems [9]. By fiber type, the global long fiber thermoplastics market is segmented into long glass fiber (GF) thermoplastics and long carbon fiber (CF) thermoplastics. There is intensive demand for long GFs in automotive, electrical and electronics industry due to high performance per cost ratio.

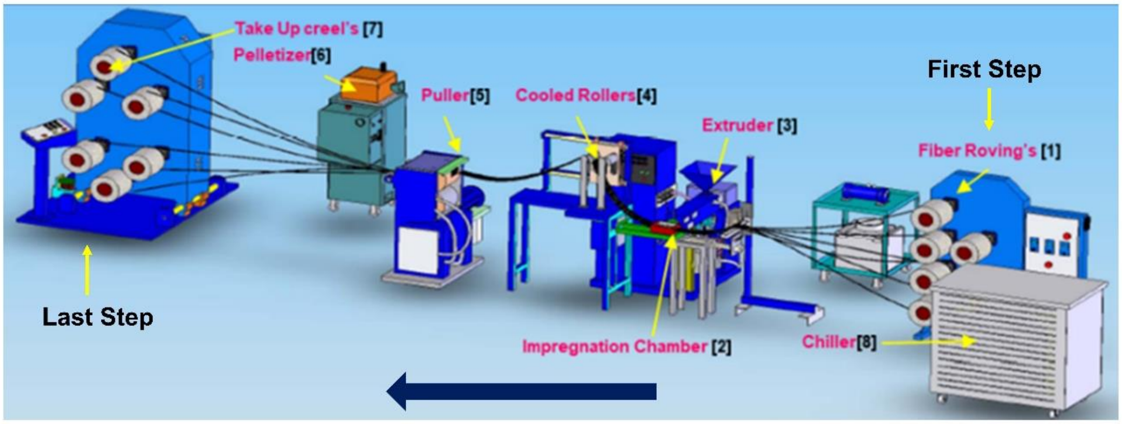

Figure 1.1: Hot melt impregnation process line for producing LFT pellets [8]. Process starts by pulling continuous fiber tows through impregnation chamber equipped with the molten thermoplastic polymer, the material drawn in a rod, cooled, and chopped into pellets of a specific length.

Whereas long CFs used in applications including aerospace and sporting goods that require high performance products [10].

1.3 LFT Pellet Processing Methods

The LFT pellets are molded into the component by typical manufacturing approaches such as injection molding (IM), ECM, and melt extrusion process.

In IM, LFT pellets are melted in an extruder and the resulting charge is injected into a closed cavity mold. The material flows in the cavity and hardens to the configuration of the cavity. The IM process is shown in Figure 1.2. IM results in highly orientated fiber in the direction of flow, which results in improved mechanical properties of a component in the flow direction [11]. However, IM is associated with fiber attrition due to the high shear witnessed by the fibers as they migrate through the screw and injection nozzle(s). Studies by Ning et al. [1], have shown there is a reduction in fiber length from 70% up to 90% depending on the type of fiber. Hence, the mechanical properties of the resulting parts can be influenced in proportion of attrition [12].

ECM is another method to produce LFT products. Whereas in ECM, the low shear screw design of the plasticator minimizes fiber attrition. Here, LFT pellets fed through the gravimetric feeder and plasticated into the hot barrel. A hot LFT charge extruded, which then placed into the mold cavity and molded into the part. Figure 1.3 illustrates the ECM process cycle. ECM provides various benefits over IM, such as- lower fiber attrition, low tooling cost due to simplicity of molds, minimal scrap generation since there are no sprue or runners, low warpage and requires less molding pressure [13], [14].

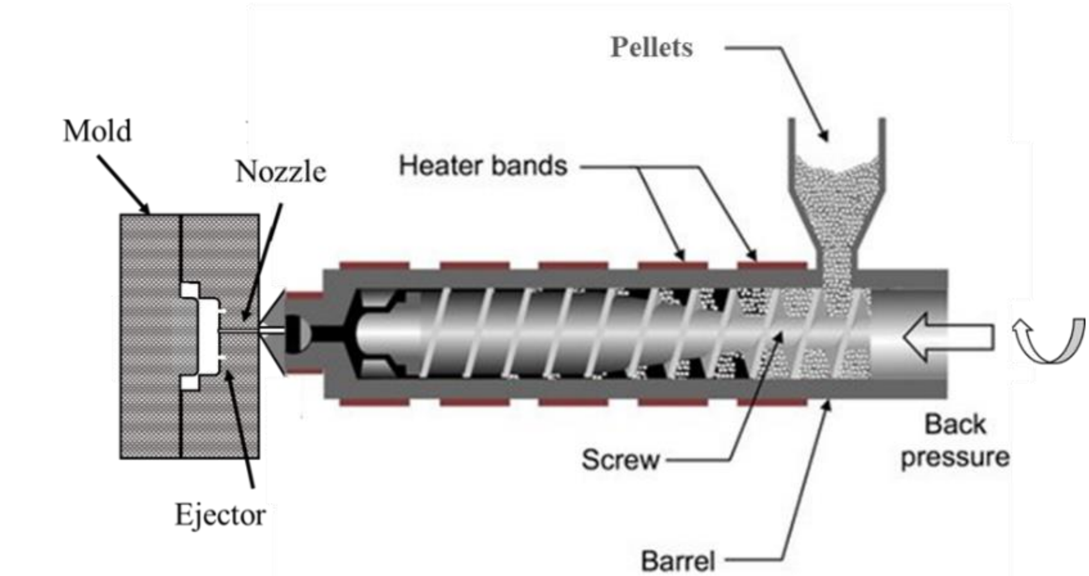

Figure 1.2: Schematic of the IM process. Pellets fed through hopper, melted in barrel, and injected in the closed mold through nozzle under high pressure.

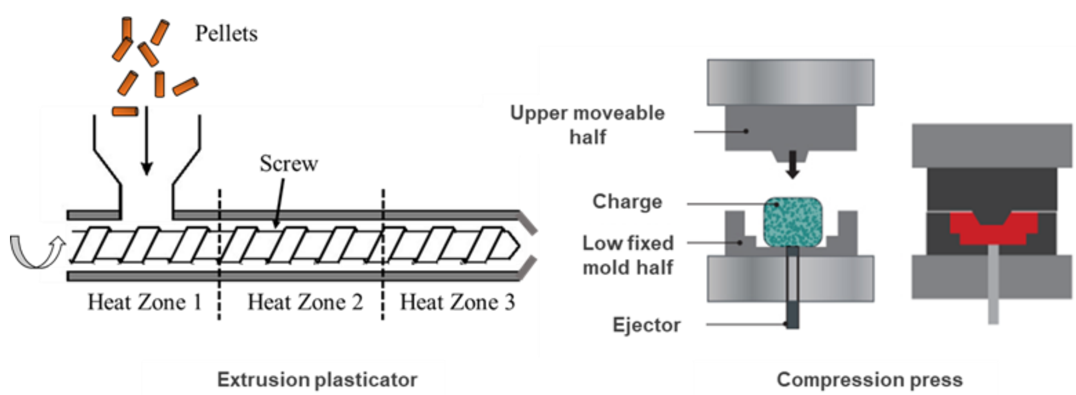

Figure 1.3: Schematic of the ECM process. LFT pellets fed through feeder, plasticated into heated barrel, hot charge extruded, placed into mold and molded into the part.

Melt extrusion process involves melting of LFT pellets through a combination of applied heat and friction. The molten material is forced under high pressure through an extrusion die and molded into desired shape as shown in Figure 1.4 [15]. The function of the extrusion die is to shape the melt as it exits the extruder into the desired cross-section, depending on the extrudate being produced. There are four different shapes for products made by extrusion dies including the extrudate strands, films, sheets, and granules. Melt extrusion process provides high throughput, highly aligned fiber retaining bulk of fiber length compared to IM, and no downstream processing is required [16].

1.4 Continuous Fiber Reinforced Thermoplastic (CFRTP) Tape

CFRTP tape is designed for increasingly demanding component requirements where filled or short fiber-reinforced thermoplastics are unable to meet and where metals are no longer an option [17]. It provides high stiffness and toughness with low weight, superior chemical resistance, corrosion resistance, ecofriendly processing, recyclability, high performance dimensional, mechanical, and thermal properties [18].

CFRTP tapes are typically manufactured using hot melt impregnation process as shown in Figure 1.5. The impregnation process enables continuous impregnation of fiber tows such as carbon, glass, and aramid with a wide range of semicrystalline and amorphous thermoplastic polymers such as PA, PP, PPS, polycarbonate (PC), and polyurethane (PU) etc [18], [19]. In this process, the fibers are pulled from a creel and passed through a collimator. Further, it is pulled through a heated die attached at the end of extruder, which delivers a hot polymer melt to a die.

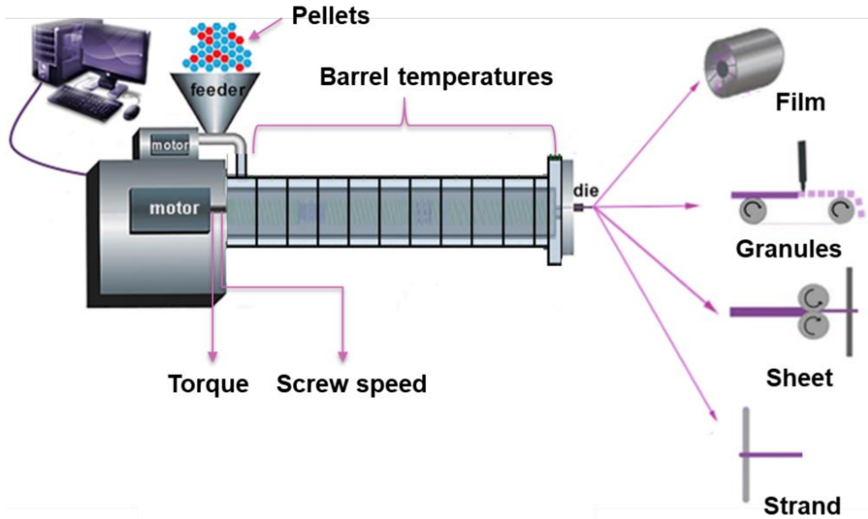

Figure 1.4: Schematic of melt extrusion process. Pellets melted in barrel, afterwards molten material extruded from extrusion die and molded into desired shape [20].

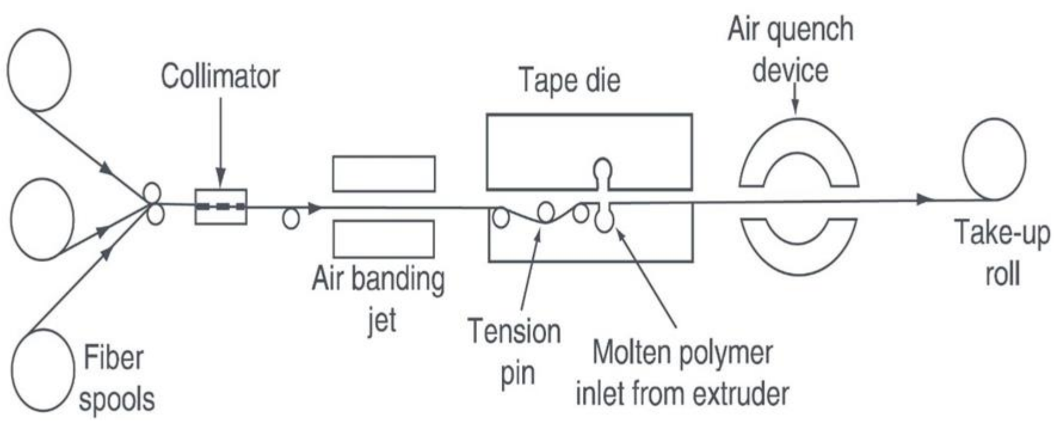

Figure 1.5: Schematics showing CFRTP tape manufacturing process by hot melt impregnation process [21].

Each filament spread using air banding jet for better fiber wet-out and it is exposed to the polymer melt under tension. Each filament spread using air banding jet for better fiber wet-out and it is exposed to the polymer melt under tension. After final calibration to the final fiber content, the impregnated material rapidly cooled down as it exists the die. The finish tape is collected on a take-up roll [22]. Tape is an intermediate material form which can be converted into final product by performing the finishing operation.

1.5 Commingled Fibers

Thermoplastic polymer matrices have 100-1000 times higher melt viscosity compared to that of thermoset resins, which makes it difficult to impregnate a dense fiber network [23]. A solution to overcome this problem is commingled yarns which are based on the principle of homogeneous distribution of continuous matrix filaments and reinforcing fibers during melt spinning. Homogeneous fiber/matrix distribution leads to shorts impregnation paths and low porosity content reflected by high mechanical performance of the thermoplastic fiber composite.

The processing of commingled yarns illustrated in Figure 1.6. In this process, the reinforcing fiber and polymer filaments are simultaneously spun and commingled while passing the sizing applicator. Minimal mechanical load is applied on the yarns ensuring there will be no damage during commingling results in high yarn strength and avoids thermal shrinkage during consolidation [21]. Compared to other intermediate product forms such as powder or pre-impregnated tows, commingled yarns are very attractive because they possess high flexibility which provides ease of molding and processing [19].

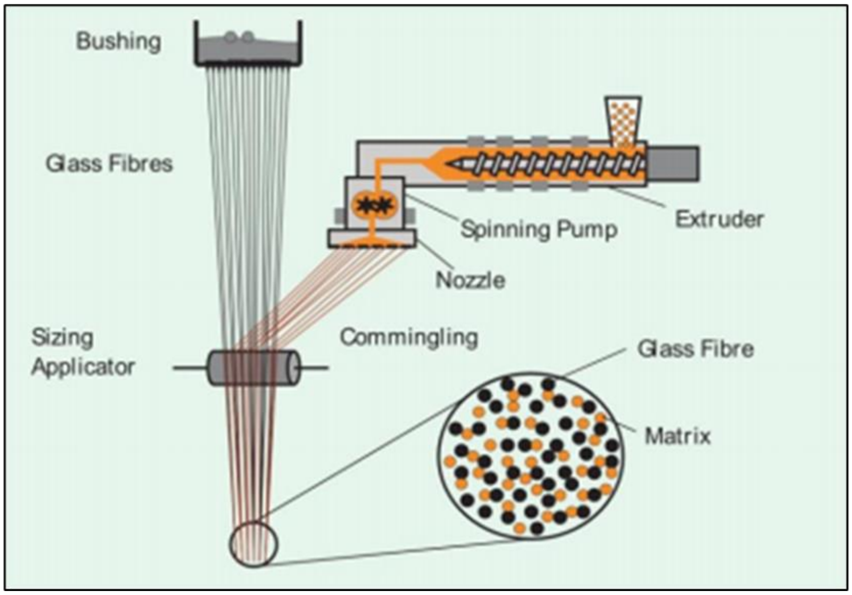

Figure 1.6: Principles of hybrid yarn spinning for commingling of fibers [23]

1.6 Overmolding Process

Overmolding of thermoplastic composites is an efficient alternative process that combines discontinuous fiber reinforced thermoplastics (LFTs) processed via ECM/IM with either pre-consolidated CFRTP tapes or commingled fibers [24]. The hybrid discontinuous-continuous process enhances specific strength and rigidity which enables lightweight complex part fabrication with high structural performance [25].

Further advantages are the potential for a high level of function integration, local or global reinforcement, replaces rib, grid structures, ability to use a greater range of materials, excellent bonding which creates interfaces considered as one structure, infinite shelf life without refrigeration and substantial reduction in tooling [26]. In CFRTP tape overmolding process, pre-consolidated CFRTP tapes were placed in strategically in the areas of high stress concentrations and further tapes are combined with LFT processed with ECM/IM. The thorough details of tape overmolding LFT process provided in the objective 2. In unidirectional commingled fiber overmolding process, the commingled fiber tow winded unidirectionally using filament winder equipment over LFT core processed via ECM/IM. After winding is complete, overall assembly consolidated into overmolded sandwich composite using compression press. However, in triaxial (0°/±60°) braided commingled fiber overmolding process, commingled fabric wrapped over extrusion-compression molded LFT core and spot fused at some locations to avoid wrinkling. Further overall assembly consolidated into overbraided sandwich composite utilizing a compression press. The thorough details of commingled fiber overmolding of LFT process are provided as Objective 3.

1.7 Research Objectives and Organization

This dissertation work investigates three objectives associated with improving performance of LFT composites. Figure 1.7 illustrates the connectivity among the three objectives. Each objective builds on from the other and is consistent with the goal of the entire study. Based on the results from three objectives the work has been divided into three manuscripts. Brief description of the proposed objectives are summarized below:

OBJECTIVE 1: INVESTIGATING THE EFFECTS OF MICROSTRUCTURAL PROPERTIES ON THE MECHANICAL PERFORMANCE OF MELT EXTRUDED, EXTRUSION-COMPRESSION MOLDED LFT COMPOSITES

For this study, two types of LFTs were considered– LFT sheets processed via melt extrusion which offers highly aligned fibers, and LFT composite produced via ECM which offers random distribution of fibers. The properties of LFT materials are highly influenced by processing techniques, which lead to different porosity contents, fiber length distributions, and fiber orientation distributions. Therefore, the work investigates the process-microstructure-property relationships and mechanisms which were very crucial to achieve tuned anisotropy, improved quality, and functionality for end-use applications. This work will be discussed in detail in chapter 2.

OBJECTIVE 2: OPTIMIZING THE MECHANICAL EFFCIENCY OF LFT COMPOSITES UTILIZING CFRTP TAPE OVERMOLDING PROCESS

The primary goal of this objective is to explore innovative overmolding approach which can offer improvement over the imposed loads without considerable increase in weight, superior crashworthiness, improved efficiency, and compelling cost element.

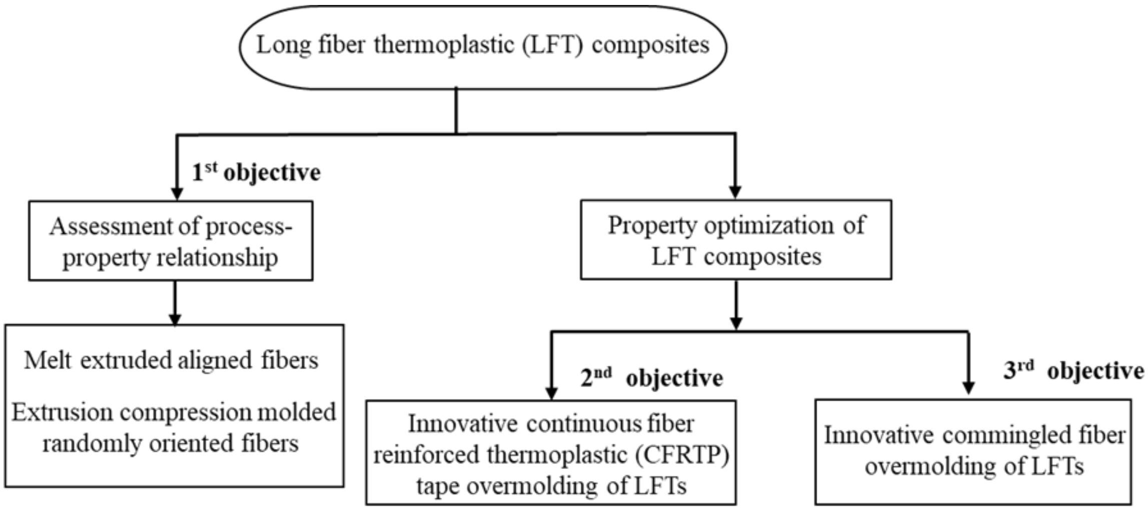

Figure 1.7: Flow chart demonstrating connectivity within the objectives

For that purpose, LFTs are overmolded with strategically placed pre-consolidated CFRTP tapes utilizing ECM process. Thermal, nondestructive, and mechanical characterization performed on overmolded samples to evaluate its performance. The effect of tape thickness on LFT composite were evaluated. A comprehensive microscopic investigation carried out on fractured samples to evaluate the constituent and interface. Flexural results were analyzed computationally. This work will be discussed in detail in chapter 3.

OBJECTIVE 3: OPTIMIZING THE MECHANICAL EFFCIENCY OF LFT COMPOSITES UTILIZING COMMINGLED FIBER OVERMOLDING PROCESS

This task is motivated to investigate forms of continuous fiber reinforcement namely unidirectional and triaxial (0°/±60°) braided commingled fibers for sandwich fabrication utilizing innovative overmolding process. Commingled fibers provide higher potential for advanced mechanical performance, homogeneous distribution of reinforcement and matrix over the yarn cross section, and ease of molding and processing. In this work, unidirectional commingled fiber overmolded LFTs and triaxial braided commingled fiber overmolded LFTs were fabricated. Both sandwich composites were evaluated for thermal, spectroscopic, microscopic, vibrational, and mechanical analysis. Further, tensile results were accurately simulated to predict mechanical behavior of sandwich composites. The simulation model of aerospace wing structure created and analyzed to predict performance. This work will be discussed in detail in chapter 4.

Figure 1.8 shows the organization of the dissertation chapters.

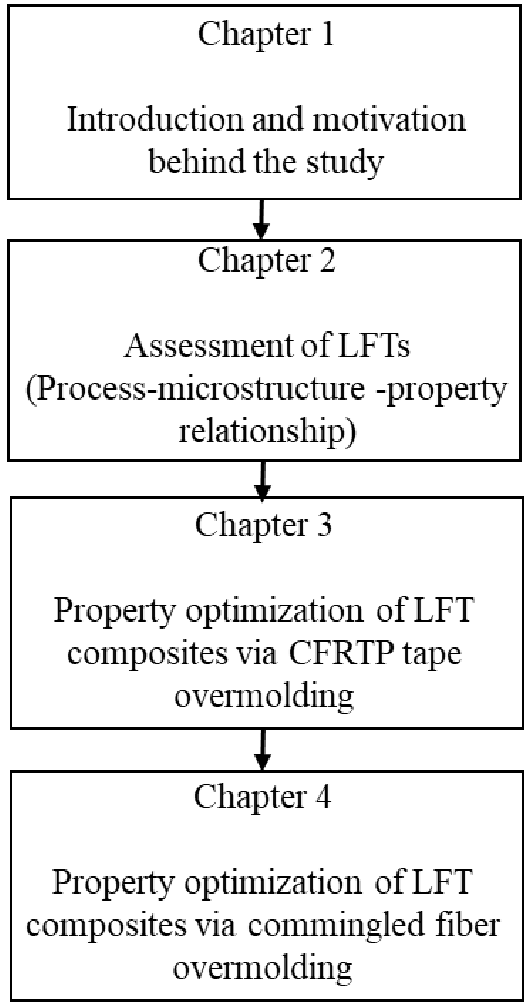

Figure 1.8: Organization of dissertation chapters

References

[1] H. Ning, N. Lu, A. A. Hassen, K. Chawla, M. Selim, and S. Pillay, "A review of Long fibre thermoplastic (LFT) composites," International Materials Reviews, vol. 65, no. 3, pp. 164–188, Apr. 2020.

[2] P. Mallick, Fiber-reinforced composites: materials, manufacturing, and design. 2007.

[3] U. Vaidya, Composites for automotive, truck and mass transit: materials, design, manufacturing. 2011.

[4] K. Chawla, Composite materials: science and engineering. 2012.

[5] R. K. Okine, D. H. Edison, and Little N. K., "Properties and Formability of an Aligned Discontinuous Fiber Thermoplastic Composite Sheet," Journal of Reinforced Plastics and Composites, vol. 9, no. 1, pp. 70–90, 1990.

[6] Fu S.-Y., Lauke B., and Mai Y.-W., 6 - Elastic modulus of short fibre reinforced polymers, in Science and Engineering of Short Fibre Reinforced Polymer Composites. Woodhead Publishing. 2009.

[7] T. Hartness, G. Husman, J. Koenig, and J. Dyksterhouse, "The characterization of low-cost fiber reinforced thermoplastic composites produced by the DRIFT™ process," Composites - Part A: Applied Science and Manufacturing, vol. 32, no. 8, pp. 1155–1160, Aug. 2001.

[8] Hudson Leigh A., V.U.K., Dean Derrick R., Pillay Selvum, and Shih Alan M., "Design, analysis and development of optimized thermoplastic pultruded profiles," 2009.

[9] J. Markarian, “Long fibre reinforcement drives automotive market forward,” Plastics, Additives and Compounding, vol. 7, no. 3, pp. 24–29, May 2005.

[10] “Long Fiber Thermoplastics Market by Resin (PP, PA, PEEK, PPA), Fiber (Glass, Carbon), Manufacturing Process (Injection Molding, Pultrusion, D-LFT), End-use Industry (Automotive, Electrical & Electronics), Region - Global Forecast to 2025,” Apr. 2020.

[11] H. Bijsterbosch and R. J. Gaymans, “Polyamide 6—long glass fiber injection moldings,” Polymer Composites, vol. 16, no. 5, pp. 363–369, Oct. 1995.

[12] S. Advani and K. Hsiao, Manufacturing techniques for polymer matrix composites (PMCs). Woodhead Publishing, 2012.

[13] P. Yeole et al., “Characterization of textile-grade carbon fiber polypropylene composites,” Polymers and Polymer Composites, Jun. 2020.

[14] M. Schemme, “LFT - development status and perspectives,” Reinforced Plastics, vol. 52, no. 1, pp. 32–39, Jan. 2008.

[15] K. D. Nelson, “Absorbable, drug-loaded, extruded fiber for implantation,” in Biomedical Textiles for Orthopaedic and Surgical Applications: Fundamentals, Applications and Tissue Engineering, Elsevier Ltd, 2015, pp. 119–143.

[16] H. Patil, R. v. Tiwari, and M. A. Repka, “Hot-Melt Extrusion: from Theory to Application in Pharmaceutical Formulation,” AAPS PharmSciTech, vol. 17, no. 1, pp. 20–42, Feb. 2016.

[17] “Celstran CFR-TP Thermoplastic Composites - Celanese-Flip eBook Pages 1 - 8| AnyFlip | AnyFlip.” https://anyflip.com/cmgu/rnhj/basic (accessed Aug. 19, 2021).

[18] "Celstran® CFR-TP." https://www.celanese.com/en/engineered-materials/products/celstran-cfrt (accessed Aug. 19, 2021).

[19] U. K. Vaidya and K. K. Chawla, "Processing of fibre reinforced thermoplastic composites," International Materials Reviews, vol. 53, no. 4. 2008. doi: 10.1179/174328008X325223.

[20] Y. Ren, L. Mei, L. Zhou, and G. Guo, "Recent Perspectives in Hot Melt Extrusion-Based Polymeric Formulations for Drug Delivery: Applications and Innovations," AAPS PharmSciTech, vol. 20, no. 3. Springer New York LLC, pp. 1–12, Apr. 01, 2019. doi: 10.1208/s12249-019-1300-8.

[21] A. C. Puitel, B. M. Tofanica, and D. Gavrilescu, "Environmentally friendly vegetal fiber-based materials," Environmental Engineering and Management Journal, vol. 11, no. 3, 2012, doi: 10.30638/eemj.2012.082.

[22] L. Laberge-Lebel and S. van Hoa, "Manufacturing of braided thermoplastic composites with carbon/nylon commingled fibers," Journal of Composite Materials, vol. 41, no. 9, 2007, doi: 10.1177/0021998306067273.

[23] N. Wiegand and E. Mäder, "Commingled yarn spinning for thermoplastic/glass fiber composites," Fibers, vol. 5, no. 3, 2017, doi: 10.3390/fib5030026.

[24] U. Vaidya, 5.3 Examples of Conventional LFT and Tailored LFT Parts, in Composites for Automotive, Truck and Mass Transit - Materials, Design, Manufacturing. DEStech Publications, 2011. Accessed: Jun. 06, 2021. [Online]. Available: https://books.google.com/books?hl=en&lr=&id=1IgDOTSha9MC&oi=fnd&pg=P

R9&dq=Vaidya,+U.,+5.3+Examples+of+Conventional+LFT+and+Tailored+LFT+Parts,+in+Composites+for+Automotive,+Truck+and+Mass+Transit+-+Materials,+Design,+Manufacturing.+2011,+DEStech+Publications.&ots=DvR05yLyX9&sig=977D2g8r64SNYLuRebuVieO09Zg

[25] R. Akkerman, M. Bouwman, and S. Wijskamp, "Analysis of the Thermoplastic Composite Overmolding Process: Interface Strength," Frontiers in Materials, vol. 7, Feb. 2020, doi: 10.3389/fmats.2020.00027.

[26] "https://www.compositesworld.com/articles/overmolding-as-enabler-for composites-aerospace-to-automotive."

2. CHAPTER 2

MELT EXTRUDED VERSUS EXTRUSION COMPRESSION MOLDED GLASS-POLYPROPYLENE LONG FIBER THERMOPLASTIC COMPOSITES*

Shailesh Alwekar, Pritesh Yeole, Vipin Kumar, Ahmed Arabi Hassen, Vlastimil Kunc, Uday K. Vaidya, Melt extruded versus extrusion-compression molded glass-polypropylene long fiber thermoplastic composites.* ***Composites Part A: Applied Science and Manufacturing**, 2021. 144: p.106349. DOI: 10.1016/j.compositesa.2021.106349.*

Abstract

Long fiber thermoplastic (LFT) composites are processed either with extrusion compression or fiber injection processes. The properties of LFT materials are highly influenced by processing techniques, which lead to different porosity contents, fiber length distributions, and fiber orientation distributions. It is important to understand the various LFT processing techniques and their effects on mechanical, thermal, and microscopic properties. This work considered LFT sheets processed via extrusion, which offers highly aligned fibers (referred to as "Tecnogor composites"), and LFT composites produced via extrusion compression molding (ECM), which offers a random distribution of fibers. Tecnogor composites exhibited higher flexural strength (35%~65%), flexural modulus (132%~172%), tensile strength (39%~52%), tensile modulus (67%~75%), and Izod impact resistance (195%~220%) than the random LFT composites. This response was attributed to the aligned fibers in Tecnogor composites. Mathematical models including Halpin-Tsai and Lavengood-Goettler were used to predict and compare the Young's modulus of Tecnogor and ECM composites, respectively.

Keywords: A. Discontinuous reinforcement, C. Statistical properties/methods, D. Microstructural analysis, D. Mechanical testing

2.1 Introduction

Long fiber thermoplastics (LFTs) are one of the forms of discontinuous fiber thermoplastic that bridges the gap between short and continuous fiber reinforced thermoplastic composites. LFTs have widespread applications in the automotive industry because of their light weight, balanced mechanical properties, corrosion resistance, low manufacturing cost, and ability to be recycled [1]. It offers more design flexibility and material choices in terms of resin and fiber reinforcements [2].

LFTs typically comprise fibers of 3 to 25.4 mm in length and reinforced with a variety of crystalline and amorphous thermoplastic polymers [3]. Their fiber aspect ratios (length/diameter) vary from 300 to 2,000 [4]. LFTs possess fiber lengths higher than the critical fiber length necessary for effective strengthening and stiffening of LFT composites [5]. Aspect ratio or fiber length influence the mechanical properties of a composite. Eq. (1.1) shows that as the fiber length increases, the mechanical properties such as strength, impact resistance, and wear resistance also increase [6, 7]. However, composite processing becomes increasingly difficult [8]. Other factors including flow stress during processing, processing conditions, and fiber content affect the fiber length distribution (FLD) [9].

LFT pellets are typically manufactured by hot melt impregnation [10], in which continuous fiber tows are pulled under tension into an extrusion die, where the dry fibers are impregnated with an extruded thermoplastic polymer. The material is then cooled rapidly as it exits the die, is pulled, and is pelletized to the desired pellet length [11]. Several factors affect the mechanical properties of LFTs, such as matrix system, types of fiber, interfacial adhesion, fiber aspect ratio, fiber fraction, and orientation of fibers [12, 13].

Various thermoplastic polymers ranging from commodity polymers to ultrahigh-performance polymers have been used as LFT matrices [4, 8]. Polypropylene (PP) is a common matrix used for LFTs because of its attractive mechanical performance at low costs, commercial availability, and suitability for a range of formulations [14]. PP-based

LFTs hold 65% of the global market share and the remaining 35% comprises engineered polyamides such as PA6, PA66, and high-temperature polymers such as PPS and PEEK [15]. LFT composites are available with glass fiber (GF), aramid fiber, and carbon fiber reinforcements, with GF common for low-cost applications. The principal advantage of using GF is high performance per cost ratio [16]. The use of long GF-reinforced PP is fast growing in automotive applications because of its superior impact resistance, high rigidity, creep resistance, potential to replace metals, and modulus retention at typical automotive temperatures (−30°C to 80°C) [17-21].

Eq. (1.1) shows that the strength of the LFTs is related to the critical fiber length. However, stiffness typically depends on the fiber content and fiber alignment present in the composite. A higher fiber content enhances the load bearing capacity and structural properties [22]. Therefore, long aligned discontinuous fiber composites have shown to be nearly equal to the modulus of continuous fiber [23]. Thomason et al. [24, 25] studied the influence of fiber concentration on the mechanical properties of GF-reinforced PP laminates. The authors reported that for random, in-plane, 0–73 wt % GF-reinforced PP laminates, the composite strength, modulus, and impact resistance exhibited a maximum performance in the fiber of 40 to 50 wt %. Above 50 wt % fiber, the increment in the modulus was less, attributed to the fiber packing problems, which resulted in increased void content and out-of-plane fiber orientation.

Another critical factor is fiber orientation. Fiber alignment in LFT processing is a function of the processing. Typically, LFTs processed using extrusion compression molding (ECM) results in random orientation (based on mold geometry and charge location), and LFTs processed using melt extrusion result in aligned LFTs. Melt extrusion provides high throughput, highly aligned fiber retaining the bulk of fiber length compared with injection molding, and no downstream processing required [26].

For fiber lengths <12 mm, the fiber attrition and fiber entanglement are minimized, thus retaining the bulk fiber length and alignment. Studies performed by Alwekar et al. [27] and Papathanasiou et al. [28] reported an average 20%~139% improvement in flexural, tensile, and impact properties of aligned fiber composites compared with the randomly oriented LFTs. Teixeira et al. [29] investigated the effect of material flow on the injection molded GF-reinforced PA66 LFT composite. The mold flow restriction system controls the material flow, which causes the fiber orientation to be in the direction of flow. This study demonstrated that the tensile strength of molded composites increased by 18% on average despite the reduction of fiber length. The improvement in tensile strength is attributed to the aligned fiber orientation in the flow direction.

This work focuses on aligned fiber LFT sheets processed through extrusion with continuous fiber–like properties [30], and randomly oriented LFT composites manufactured using extrusion compression. Thermal analysis—namely, a differential scanning calorimeter (DSC) and thermo-gravimetric analyzer was performed to determine the thermal properties. Flexural, tensile, and impact properties were evaluated for both types of LFT composites. The Young’s modulus of the aligned and random fiber composites was predicted by Halpin-Tsai and Lavengood-Goettler methods, respectively. Microstructural properties including FLD, porosity, and fiber orientation distribution

(FOD) was measured. Fiber orientation results were analyzed through the analysis of variance (ANOVA) F-test statistical method.

2.2 Experimental

2.2.1 Materials and Processing

Two types of LFT material were used in this work. First, GF-PP aligned discontinuous LFT sheets comprising melt-extruded discontinuous fibers in sheet form were provided by the American Renolit Corporation [31]. These were Tecnogor composite sheets; two formulations were used (Table 2.1). Second, Celstran® GF-PP LFT pellets of 11 mm (0.43 in.) fiber length, 40 wt % GF, and ~1,210 kg/m3 (~1.21 g/cc) density were obtained from Celanese Corporation. Celstran® GF-PP LFT pellets were processed using the ECM technique to fabricate randomly oriented LFT composites. For this purpose, a low-shear single-screw extrusion plasticator (Impco B20 low-shear extrusion plasticator with 50.8 mm [2 in.] barrel diameter and 304.8 mm [12 in.] shot size) and 100-ton compression hydraulic press (Beckwood Corporation, Fenton, Missouri, USA) were used. The extrusion plasticator has four heating zones, which were used to melt LFT pellets. Each heating zone was set and maintained above the melting point of PP (i.e., 210°C, 216°C, 227°C, and 227°C, respectively). LFT pellets were fed into a heated barrel where the GFs were uniformly dispersed into a molten PP polymer, and then produced a molten LFT charge of ~410 g extruded from the heated barrel. The extruded charge was immediately transferred into a pre-heated (44°C) flat mold 279.4 × 279.4 mm (11 × 11 in.)

mounted in a Beckwood hydraulic press. To let the charge flow and fill the mold cavity uniformly, pressure of 4.56 MPa (661 psi) was applied. Prior to demolding, the LFT panel was dwelled for 5 min (longer than usual to avoid warpage). A 279.4 × 279.4 × 4 mm (11 × 11 × 0.16 in.) LFT composite panel was fabricated.

2.2.2 Thermal Analysis

Thermo-gravimetric analysis (TGA) was performed on Tecnogor A, Tecnogor D, and random LFT samples for thermal evaluation. TGA samples were heated within 25°C to 700°C in an oxygen atmosphere at the heating rate of 20°C/min using the TGA Q50 (V6.7 Build 203) instrument (TA Instruments, New Castle, Delaware, USA). The melting behavior of Tecnogor A, Tecnogor D, and random LFT was determined using the DSC Q2000 (V24.11 Build 124) instrument (TA Instruments, New Castle, Delaware, USA). A heat/cool/heat procedure was performed. The samples were heated from 25°C to 250°C at a heating rate of 10°C/min.

An isothermal step of 2 min at 250°C was initiated to remove the previous thermal history. The samples then cooled to room temperature and were again reheated with a heating rate of 10°C/min to obtain the melting peak. Because PP is a semi-crystalline polymer, the degree of crystallinity (X_c) was determined using Eq. (2.1):

$$X_c = \frac{\Delta H_m}{\Delta H^*} \times 100\% \qquad \text{(Eq 2.1)}$$

Table 2.1: Properties of GF-PP aligned discontinuous LFT sheets.

Nomenclature*	**Thickness, mm (in.)**	**Fiber length, mm (in.)**	**Fiber wt %**	**Fiber weight GSM**	**Density, kg/m^3 (g/cc)**	**Melting point, °C**
Tecnogor A	1.52 (0.06)	7 (0.28)	50	1,991	1,310 (1.31)	170
Tecnogor D	1.48 (0.06)	7 (0.28)	35	1,938	1,310 (1.31)	170

where ΔH_m is the specific enthalpy of fusion (J/g) of the sample calculated by integrating the area of the melting peak, and ΔH^* is the standard enthalpy of fusion of a 100% crystalline PP, 209 J/g [9].

2.2.3 Microstructural Characterization

Fiber Length Distribution (FLD)

The FLD was measured to obtain the distribution characterizing the fiber microstructure of Tecnogor A, Tecnogor D, and random LFT samples. During the ECM manufacturing process, the fibers get distributed in all directions because of the flow of molten charge. Therefore, the samples of 19.05 × 19.05 mm (0.75 × 0.75 in.) were chosen from three locations (Figure 2.1, marked M, X, Y) for FLD measurement. The FLD measurements on GF-PP composite samples were performed by removing the PP matrix (samples were burned off at 400°C for 4 h in an oxygen environment using a Thermo Fisher Scientific muffle furnace, Model # F48015-60, North Carolina, USA), selecting the central fibers through the entire thickness of the fiber stack, dispersing the selected central fibers, and measuring the lengths from a set of digitized images stored in TIF image format. The detailed FLD measurement procedure for glass filled LFT materials is reported in the literature [32, 33].

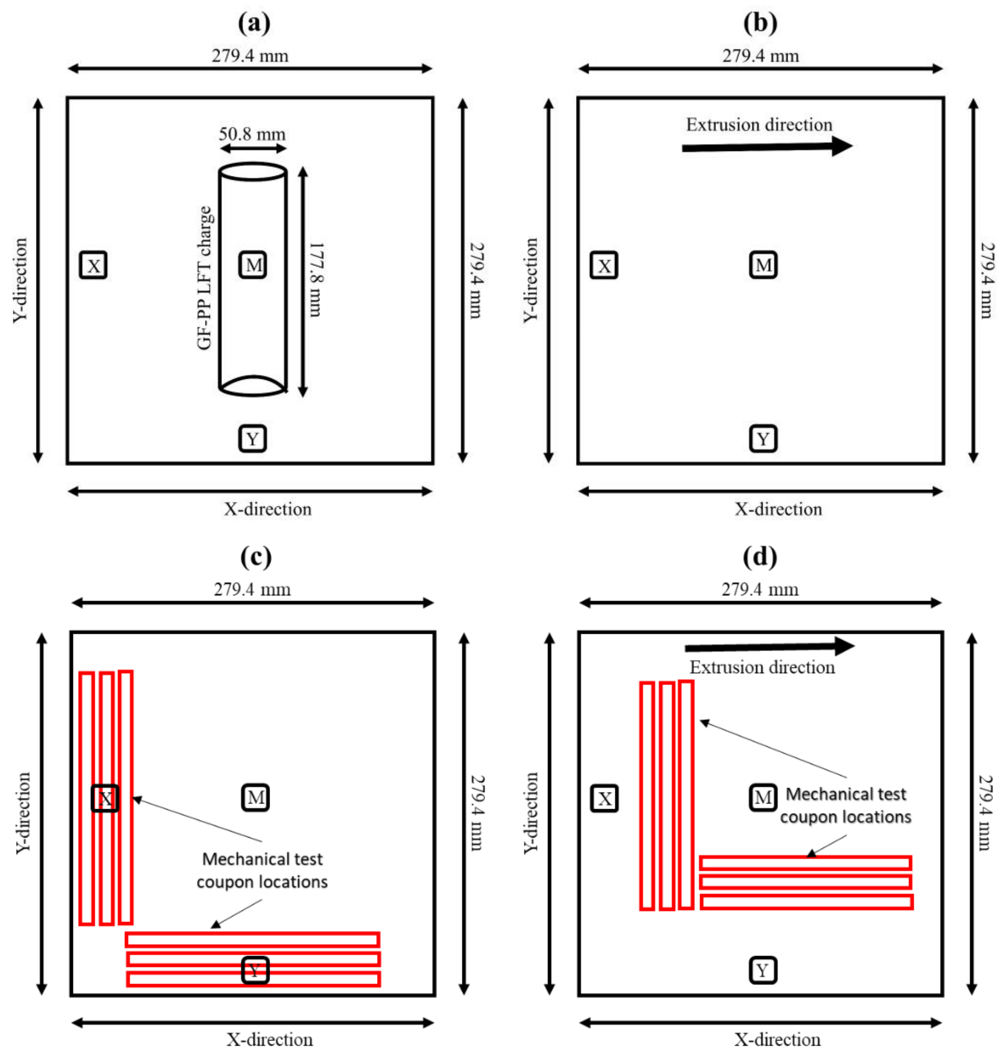

Figure 2.1: Top view representation of (a) a random GF-PP LFT sample showing charge placement in the mold, (b) a Tecnogor sample showing extrusion direction. Respective samples were extracted from locations marked M, X, and Y (middle, X direction, and Y direction locations of the panel) for FLD and FOD calculations, and (c, d) showing test coupon locations for mechanical (flexural, tensile, Izod impact) testing.

Porosity and Fiber Orientation Distribution (FOD)

X-ray computed tomography (XCT) was performed to nondestructively inspect fiber orientation and porosity level within the composites. To perform XCT, 12.70 × 12.70 mm (0.50 × 0.50 in.) samples were extracted from the middle location (Figure 2.1, marked M) of Tecnogor A, Tecnogor D, and random LFT composites. The tomograms were performed using Zeiss Xradia Versa 520 XCT at 3 W power and 40 kV accelerating voltage. For each tomogram, 1,601 radiographs were acquired from horizontally rotating sample with a 1.5 µm resolution. A 4× scintillator objective was used coupled with a highly sensitive charged coupled device camera to collect the radiographs. To extract quantitative and qualitative information of porosity (content, size, shape, and location) within composites, 3D tomograms were analyzed using commercial package DragonflyPRO (version 3.5). A non-local means smoothing filter [34] was used to reduce the noise in the data while preserving the shape and size of the defects. Line segmentation method was used to threshold characteristic phases (fiber, matrix, and voids) based on its grayscale intensity level.

To quantify the FOD, 3D tomograms were reconstructed and visualized using image processing software Avizo (version 9.3.0, XFiber module, Thermo Fisher Scientific) [35]. The software implemented with the algorithms included an adaptive nonlocal means filtering component to exclude noise from each scan and prepare them correctly for the analysis. Thresholding separates the clustered phases of the composites. The Avizo's cylinder correlation module will try to correlate a cylinder template with fibers in data in all orientations to mark each voxel with a score. The cylindrical template defined was by providing fiber length and fiber radius as cylinder length and radius to fit with the fiber structure of the data. The module helps to construct a local orientation tensor. Most of the fibers were correlated throughout the scanned volumes and the orientation of each and then exported into a data format. A spherical coordinate system was used to present fiber segments, which permits quantification of the offset angle from the longitudinal direction. Theta (θ) represents the angle formed with the X-axis and varies from 0° to 90°. The fibers were treated and aligned to the longitudinal direction as θ reaches 0°.

2.2.4 Mechanical Analysis

For mechanical (flexural, tensile, and Izod impact) testing, test coupons were extracted in the X and Y directions (see Figure 2.1) from Tecnogor A, Tecnogor D, and random LFT composite panels with a wet tile saw. The test coupon locations for Tecnogor A, D and random LFT composite panel shown in Figure 2.1 c, d. For mechanical analysis, a minimum of five coupons each were prepared and tested at room temperature according to American Society for Testing and Materials (ASTM) standards as summarized in Table 2.2.

Flexural testing was performed using a 50 KN Test Resources frame (product # 313Q, Test Resources, Minnesota, USA). Tecnogor A, Tecnogor D, and random LFT samples were tested according to ASTM D790 standard with a test rate of 0.73, 0.76, and 1.84 mm/min, respectively. Tensile testing was carried out according to ASTM D3039 standard at 2 mm/min loading rate using a 100 KN MTS frame (model # 647, MTS System Corporation, Eden Prairie, Minnesota, USA).

Table 2.2: Sample dimensions for mechanical testing as per ASTM standards.

Test	Samples	Average dimensions, mm		
		Length	**Width**	**Thickness**
Flexural ASTM D790	Tecnogor A	50.32	13.31	1.54
	Tecnogor D	50.30	13.22	1.46
	Random LFT	80.05	13.40	3.71
Tensile ASTM D3039	Tecnogor A	254.80	25.53	1.58
	Tecnogor D	254.40	26.01	1.44
	Random LFT	255.60	25.54	4.10
Izod impact ASTM D256	Tecnogor A	63.29	12.61	1.57
	Tecnogor D	63.72	12.66	1.46
	Random LFT	64.26	12.96	3.70

A Tinius Olsen-IT 504 impact pendulum (Tinius Olsen Testing Machine Co. Inc., Horsham, Pennsylvania, USA) was used to perform Izod impact testing according to ASTM D256 standard.

2.3 Results and Discussion

2.3.1 Thermal Analysis

Thermal stability/degradation information of Tecnogor A, Tecnogor D, and random LFT composites is essential to determine the end-use application, and it was investigated using TGA. Figure 2.2 exhibits the single-stage decomposition over the entire range of temperature. Less than 1% weight loss was observed in Tecnogor A, Tecnogor D, and random LFT composites when heated to 284°C, 280°C, and 274°C, respectively. This loss indicates the absence of moisture content, thermal stability of the PP phase, and the upper processing temperature limit of each composite. A mass drop was observed from 360°C to 440°C, due to the thermal degradation of the material. At 650°C, the residual amount indicates the actual GF content in Tecnogor A (48.40 wt %), Tecnogor D (45.45 wt %), and random LFT (42.40 wt %) composites. TGA data of Tecnogor A, Tecnogor D, and random LFTs shows 3% lower, 30% higher, and 6% higher GF content, respectively, compared with the company data sheet (Section 2.2.1).

Figure 2.3(a) and 2.3(b) represents the heating and cooling DSC curves, respectively. DSC curves provided information about the melting and crystallization behavior of Tecnogor A, Tecnogor D, and random LFT composites.

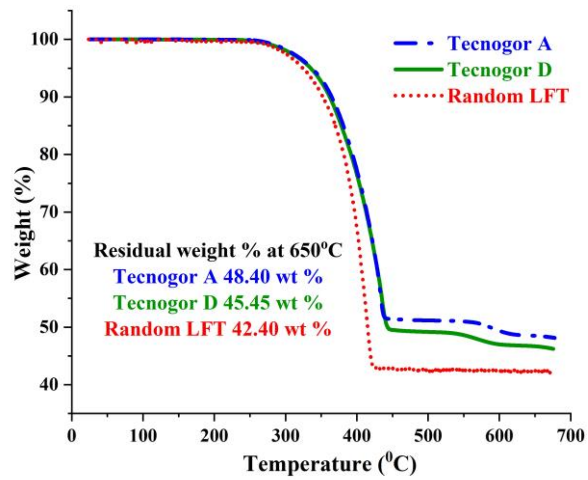

Figure 2.2: TGA thermographs of Tecnogor A, Tecnogor D, and random LFT samples shows single-stage decomposition with residual weight percent at 650°C.

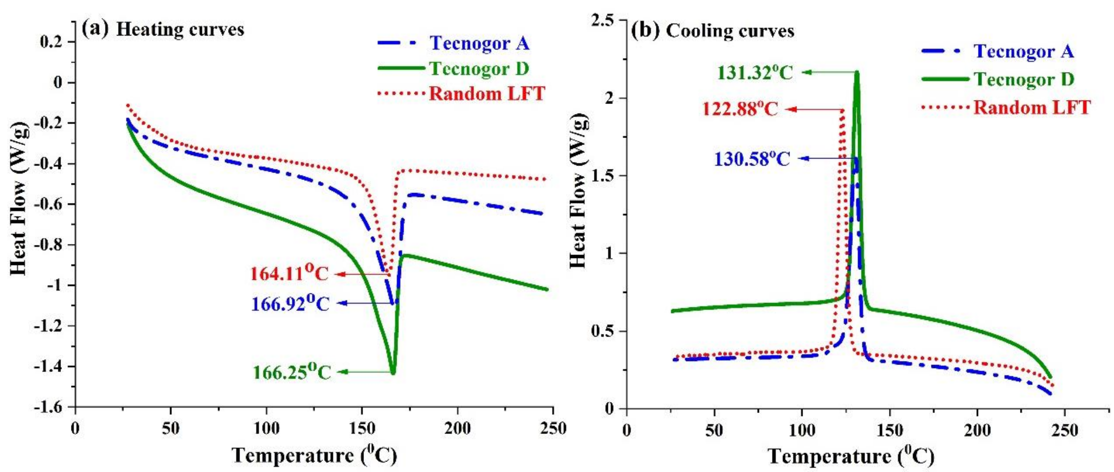

Figure 2.3: DSC thermographs of Tecnogor A, Tecnogor D, and random LFT samples; (a) heating curves with peak melting temperature and (b) cooling curves with peak crystalline temperature.

Thermal properties such as peak melting temperature (T_m), peak crystallization temperature (T_c), enthalpy of fusion (H_m), and degree of crystallinity (X_c) of Tecnogor A, Tecnogor D, and random LFT samples were extracted from the DSC analysis and tabulated in Table 2.3.

The T_m of Tecnogor A (166.92°C) and Tecnogor D (166.25°C) were similar and slightly higher than that of the random LFT (164.11°C). This indicates that the microstructures of the aligned Tecnogor composites were different from the randomly oriented LFT composite. The T_c of the aligned Tecnogor composites increased by 7.70°C to 8.45°C compared with the random LFT composite (122.88°C). This could be attributed to increased GF content and well-distributed GFs [36]. Zhang et al. [37], reported that the degree of crystallinity improves as GF length increases and percentage decreases. The Tecnogor materials had lower GF length (explained in Section 2.3.2) and higher GF percentage than the random LFT. However, Tecnogor A and Tecnogor D illustrated 19.75% and 13.20% higher degrees of crystallinity than that of the random LFT composite, respectively. In melt extrusion process, as hot melt passes through a tapered linear sheet extrusion die with decreasing cross-section, the polymer melt gets strained and aligns the fibers in flow direction. The velocity of melt flow increases when passing through the die resulting the velocity gradient which extends the connected polymer segments and favors the linear crystal growth in the flow direction [38]. Therefore, Tecnogor composites demonstrate improved crystallinity compared to random LFT composite.

Table 2.3: DSC thermal properties of Tecnogor A, Tecnogor D, and random LFT composites.

Material	T_m, °C	T_c, °C	H_m, J/g	X_c, %
Tecnogor A	166.92	130.58	52.34	25.04
Tecnogor D	166.25	131.32	49.46	23.67
Random LFT	164.11	122.88	43.71	20.91

2.3.2 Microstructural Characterization

Fiber Length Distribution (FLD) Analysis

The feedstock used for the Tecnogor A and D sheets possessed a starting fiber length of 7 mm in contrast to the random LFT composite starting fiber length of 11 mm. The FLD influences the mechanical performance of the final composite [12]. Therefore, it is crucial to understand the effect of the manufacturing process and processing parameters on the FLD in aligned and random LFT composites. The FLD was determined by manually measuring the fiber length of ~1,000 fibers each using image processing software (ImageJ, Version 1.52a, bundled with Java 1.8.0_112). The sample locations M, X, and Y shown in Figure 1 represent the middle, X direction, and Y direction locations of the panel, respectively. Table 2.4 and Figure 2.4 represent the FLD statistics of Tecnogor A and D sheets (manufactured through melt extrusion), and random LFT composites (manufactured through ECM). The average mean FLD of all locations (M, X, and Y) of Tecnogor A, Tecnogor D, and random LFT samples were 1.15, 0.69, and 3.07 mm, respectively. A ~83%, ~90%, and ~72% reduction of fiber length occurred in Tecnogor A, Tecnogor D, and random LFT samples, respectively. Yeole et al. [39] demonstrated that in any extrusion process, fiber-fiber interaction, fiber-wall interaction, stresses developed because of matrix rheology, and solid-melt fiber interactions are the main causes of fiber breakage.

Thus, the above factors contribute to reduced FLD within Tecnogor and random LFT composites.

Table 2.4:Descriptive statistics of FLD measurements for Tecnogor A, Tecnogor D, and random LFT composites.

Composite material	Location	Mean (mm)	Avg. mean (mm)	Variance (mm)	Std. deviation (mm)	Range (mm)	Skewness (mm)	Kurtosis (mm)
Tecnogor A	M	1.09	1.15	0.14	0.37	4.24	3.34	18.63
	X	1.13		0.07	0.27	3.18	1.07	7.40
	Y	1.22		0.14	0.37	3.98	2.46	10.26
Tecnogor D	M	0.65	0.69	0.04	0.21	2.08	1.50	5.66
	X	0.72		0.13	0.36	3.12	2.64	10.24
	Y	0.70		0.07	0.26	3.02	2.72	13.52
LFT	M	2.35	3.07	1.71	1.31	7.82	1.28	2.13
	X	3.39		3.81	1.95	9.91	0.92	0.49
	Y	3.48		4.17	2.04	9.76	0.80	0.04

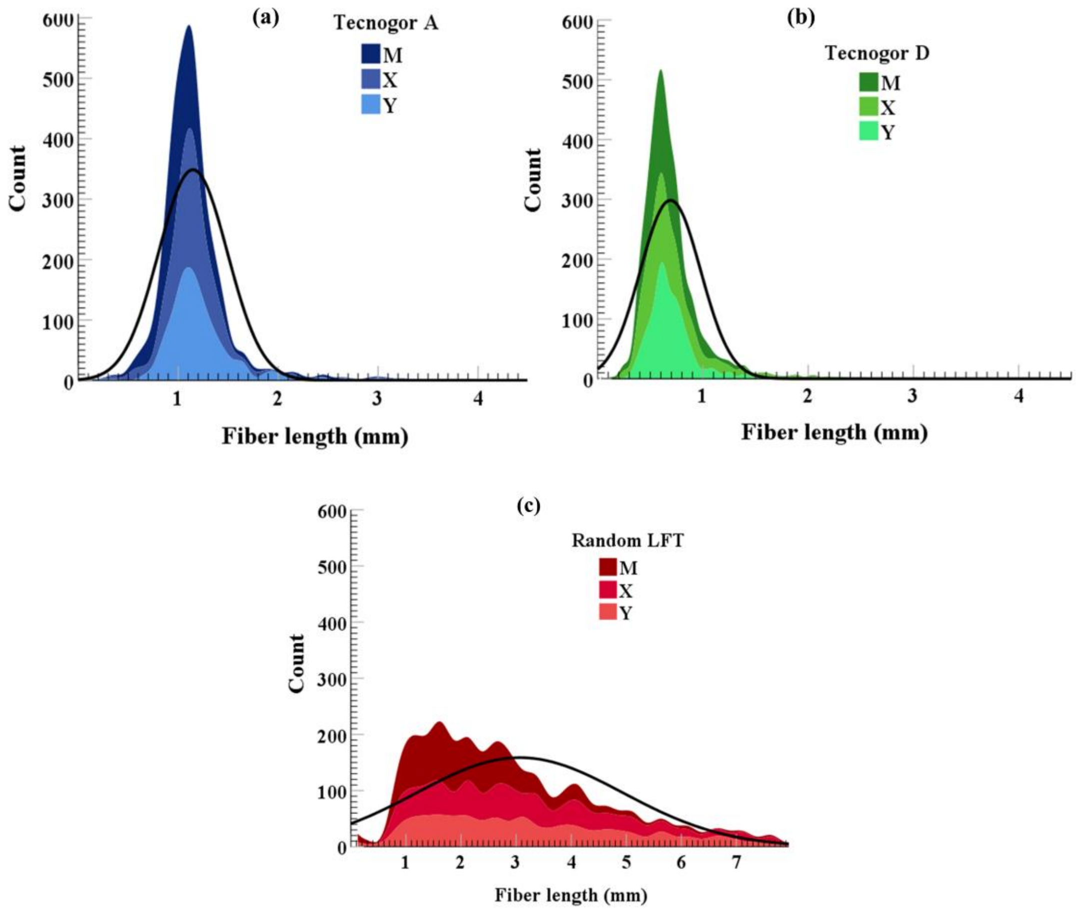

Figure 2.4: Superimposed FLD histograms of middle, X, and Y locations of (a) Tecnogor A, (b) Tecnogor D, and (c) random LFT samples.

Tecnogor A, Tecnogor D, and random LFT composite samples exhibited a distribution with a significant positive skewness (measures the asymmetry of distribution) and a long tail toward the right.

In Tecnogor A and D samples, the measure of kurtosis indicates the FLD measurements clustered more around the mean to form a tall peak. The mean value of FLD does not deviate much with the sample locations (Figure 2.4 a, b). In the random LFT sample, the FLD measurements clustered less around the mean to form a flat hill (less peaked) than the Tecnogor composites (see Figure 2.4 c). The mean FLD at X and Y locations was higher than the M location of the random LFT panel. Yeole et al. [39] and Willems et al. [40] reported that there is always a temperature gradient between the skin and core of the hot molten extruded charge. Thus, fibers get sheared in between the frozen skin and hot molten core because of the flow of the charge. Chopped fibers in the skin area remained in the extruded charge placement location (in this study, the charge was placed at the center of the mold; see Figure 1); however, longer fibers were transported with the melt flow in X and Y directions. Therefore, FLD at the middle location was lower than the other locations. Significant standard deviation in the mechanical properties of random LFT samples was observed compared with the aligned Tecnogor A and D samples (Section 2.3.3).

Porosity Analysis

Figure 2.5 a, c, and e show the 3D raw grayscale volume, and Figure 2.5 b, d, and f show the 3D volume with porosity of Tecnogor A, Tecnogor D, and random LFT samples,

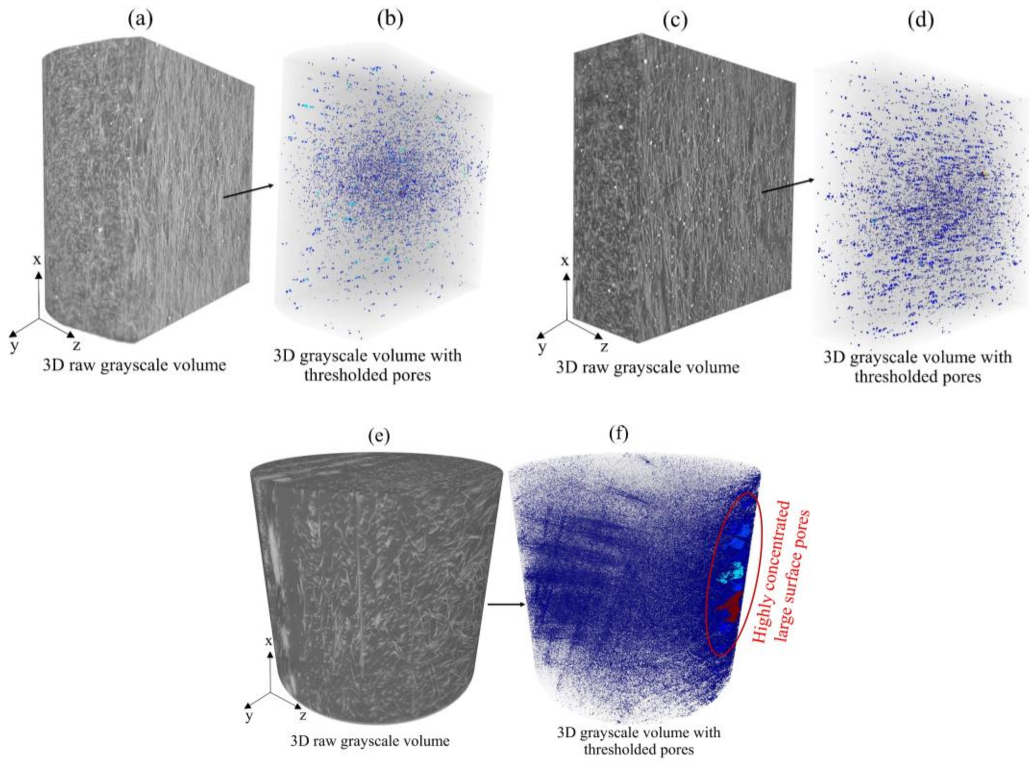

Figure 2.5: 3D raw grayscale volume and volume with an applied threshold range of pores showing size, shape, and location of pores in (a, b) Tecnogor A, (c, d) Tecnogor D, and (e, f) random LFT samples. The random LFT sample shows highly concentrated pores near the surface.

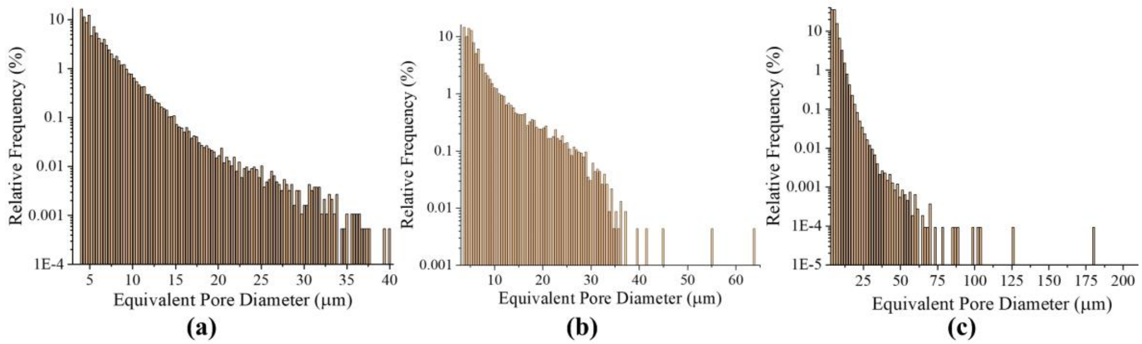

Figure 2.6: Relative frequency distribution as a function of equivalent pore diameter; (a) Tecnogor A (contains 0.132% pores), (b) Tecnogor D (contains 0.073% pores), and (c) random LFT (contains 0.5% pores).

respectively. The 3D images provide the location, size, and volume percentage of voids in the composites. Tecnogor A, Tecnogor D, and random LFT samples displayed scattered porosity throughout their volume. Porosity occurs in the form of entrapped air or other volatile gases during the extrusion process [14]. The random LFT showed heterogeneous distribution of large pores highly concentrated near the surface (Figure 2.5 f). In the random LFT samples, the hot (227°C) GF-PP extrudate placed in the relatively colder (44°C) mold resulted in a rapid reduction temperature of the skin with respect to the core of the extrudate. Thus, the charge near the vicinity of the skin had a higher shear resistance (wall effect) compared with the core of the extrudate, leading to large surface porosity [39].

Figure 2.6 illustrates the relative frequency of pores as a function of equivalent pore diameter. Tecnogor A and D had majority pores in the diameter range of 0 to 38 µm, whereas the random LFTs had most of the pores in the diameter range of 0 to 75 µm. The pore diameters were calculated from the segmented volumes assuming spherical pore morphology. Therefore, as pore diameter increases, pore volume increases. The total volume percentage of pores (ratio of total segmented pore volume to the total sample volume) was evaluated based on the image analysis of the XCT scan volumes. Tecnogor A had 0.132% pores, Tecnogor D had 0.073% pores, and the random LFT had 0.5% pores (Figure 2.6 a, b, c). Tecnogor D had pores with moderate size but less in number compared with Tecnogor A. Hence, Tecnogor D had minimal porosity. In the random LFT, the porosity was significantly increased because of the existence of a few large-diameter pores near the surface (results in a large volume) as shown in Figure 2.5 f. Tecnogor A, Tecnogor D, and random LFT samples represented porosity levels below 1%. This provides enough evidence of the optimal manufacturing process of Tecnogor A, Tecnogor D, and random LFT composites.

Fiber Orientation Distribution (FOD) Analysis

The orientation of the fibers depends on the applied processing parameters during manufacturing and may vary from randomly to nearly perfectly aligned fibers. Mainly there is a FOD in the molded LFT composites. Hence, it is essential to understand fiber orientation within Tecnogor A, Tecnogor D, and random LFT composites.

Figure 2.7 represents the 3D iso-parametric view of fiber orientation within each composite sample. A color-coding scheme (0° as blue, 45° as green, and 90° as red) was implemented to distinguish the characteristic fiber orientation of individual fibers. Tecnogor A and D had preferentially aligned fibers. The skin of the Tecnogor sheet demonstrated highly oriented fibers in the flow direction of the extrudate. The core exhibited partial alignment with a small average angle of the fibers with the flow direction (Figure 2.7a, b). On the other hand, the random LFT sample exhibited randomly oriented fibers through the thickness except in regions closer to the LFT core. During manufacturing of random LFT composites, the LFT charge flowed because of application of pressure and filled the entire mold cavity in the planar flow pattern [41], which resulted in randomly oriented fibers. During charge flow, the strong shear force developed between the frozen skin and hot molten core aligned the fibers close to the core in the preferential flow directions. Thus, we observed fiber alignment in some regions (see Figure 2.7c).

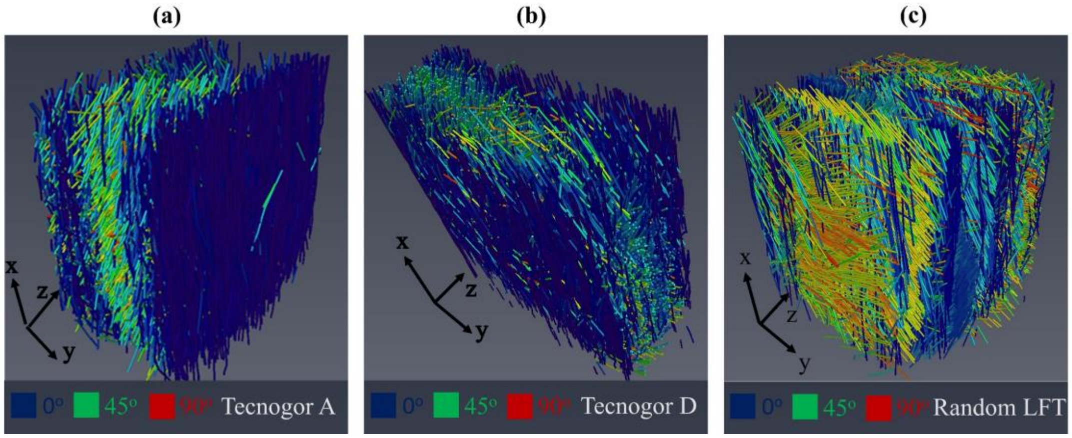

Figure 2.7: 3D visualized fiber orientation; (a) Tecnogor A, (b) Tecnogor D, and (c) random LFT samples. Tecnogor A and D demonstrated most GFs oriented in the X direction, whereas the random LFT exhibited randomly oriented fibers.

The fiber orientation was measured using Avizo's cylinder correlation module that helps to construct local orientation tensor. The spatial position of a fiber can be defined by the two Euler angles θ and ϕ. θ is defined as the angle that the fiber makes with the X-axis in which orientation is measured. ϕ is the angle that the fiber makes with the 2-axis when projected onto the YZ plane [35, 42]. Figure 2.8 displays the FOD in Tecnogor A, Tecnogor D, and random LFT samples. A total of 20,464, 19,133, and 7,742 fibers of Tecnogor A, Tecnogor D, and random LFT samples were counted in various orientations (θ), respectively. The dominant flow directions of the random LFT were between 20° and 30° (16.60%), and between 60° and 70° (17.27%) in the θ direction (see Figure 2.8 c). The flow direction of fibers highly depended on charge placement/location in the mold. It is very difficult to control for every charge placed in the mold, which results in inconsistent fiber orientation. The FOD data exhibited that Tecnogor A and D samples had ~47.76% and ~47.87% of fibers, respectively, oriented in the range of 0° to 20° in the θ direction compared with the random LFT at ~24.4%.

2.3.3 Mechanical performance

Experimental Data

Table 2.5 displays the mechanical properties of Tecnogor A, Tecnogor D, and random LFT composites. Tecnogor A and D exhibited higher flexural, tensile, and impact properties than the random LFT in the X direction (summarized in Table 2.5 and Figure 2.9). Flexural strength and modulus of Tecnogor A in the X direction were 64.99% and 171.57% higher, respectively, than the random LFT.

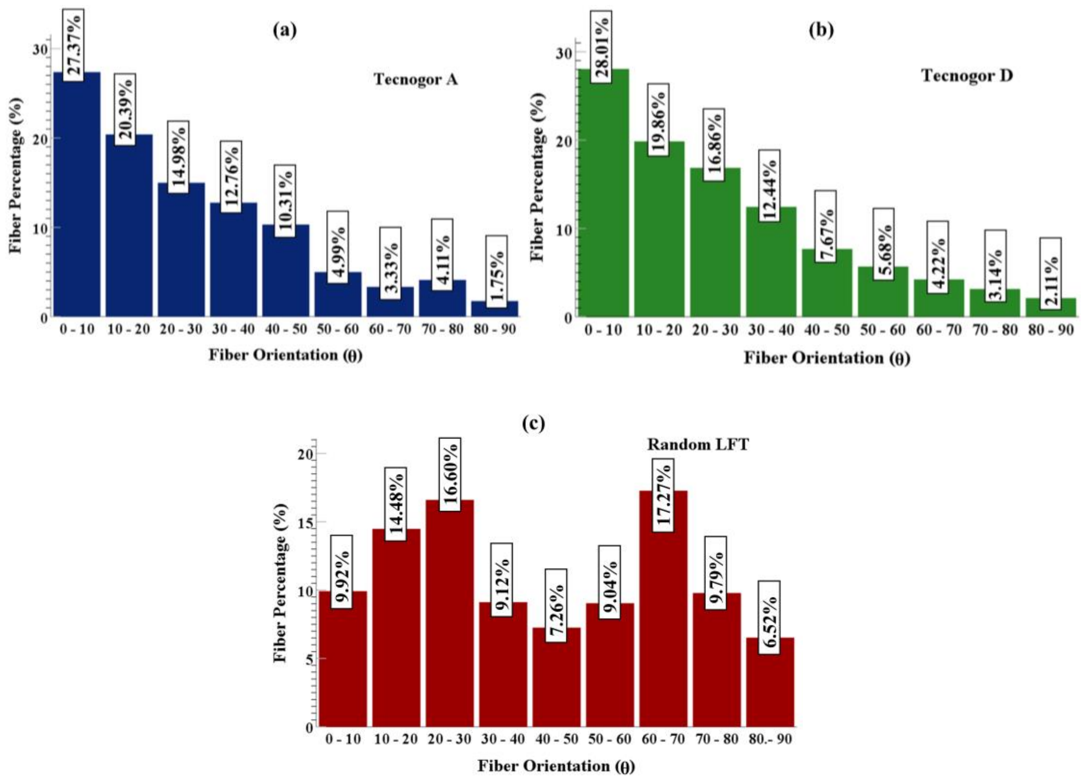

Figure 2.8: θ distributions of the fibers analyzed using Avizo software; (a) Tecnogor A, (b) Tecnogor D, and (c) random LFT samples. Orientation data were binned into equal width class intervals. Tecnogor A, Tecnogor D, and random LFT samples showed ~47.76%, ~47.87%, and ~24.4% fibers in the range of 0° to 20° in the θ direction, respectively.

Table 2.5: Mechanical properties of Tecnogor A, Tecnogor D, and random LFT samples.

Mechanical testing			**Tecnogor A**		**Tecnogor D**		**Random LFT**	
			X dir	**Y dir**	**X dir**	**Y dir**	**X dir**	**Y dir**
Flexural	Strength (MPa)	Mean	205.08	91.36	167.94	89.11	124.30	85.71
		STD	2.97	3.98	7.73	2.80	22.00	4.65
	Modulus (GPa)	Mean	11.27	4.05	9.63	3.67	4.15	2.88
		STD	0.20	0.23	0.45	0.19	0.64	0.27
Tensile	Strength (MPa)	Mean	81.24	32.42	74.45	28.98	53.42	36.02
		STD	3.13	0.39	4.14	0.34	7.66	6.97
	Modulus (GPa)	Mean	8.64	4.48	8.28	4.46	4.95	3.43
		STD	0.88	0.42	0.54	0.40	0.84	0.43
Izod	Impact energy (KJ/m^2)	Mean	10.64	5.58	11.53	4.92	3.60	—
		STD	0.84	0.30	0.70	0.41	0.86	—

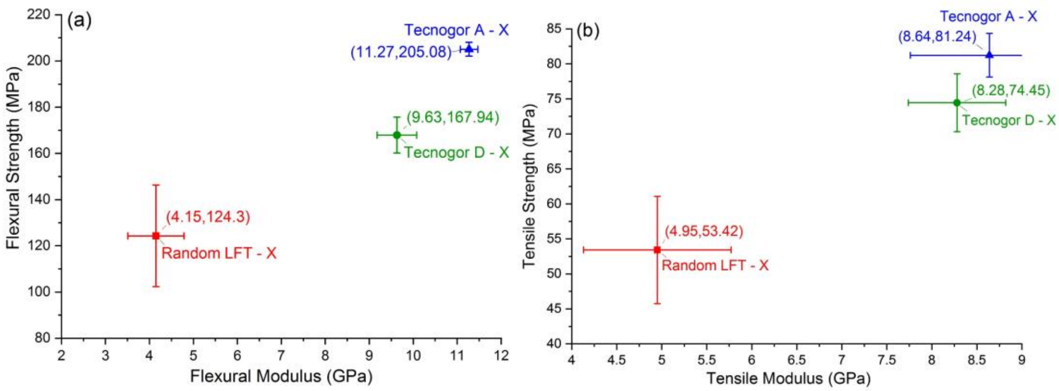

Figure 2.9: Mechanical properties of Tecnogor A, Tecnogor D, and random LFT samples; (a) flexural strength versus flexural modulus, and (b) tensile strength versus tensile modulus.

Similarly, Tecnogor D in the X direction demonstrated 35.11% and 132.05% higher flexural strength and modulus, respectively, than the random LFT. A similar trend can be observed in tensile properties. Tensile strength and modulus of Tecnogor A in the X direction were 52.08% and 74.55% higher, respectively, than the random LFT. Similarly, Tecnogor D showed 39.37% and 67.27% superior tensile strength and modulus, respectively, compared with the random LFT. To evaluate the impact energy dissipation of aligned Tecnogor and random LFT composites, Izod impact pendulum testing was conducted. In the X direction, Tecnogor A and D demonstrated 195.55% and 220.27% higher impact resistance, respectively, than the random LFT. Standard deviations in random LFT samples were significant compared with the aligned Tecnogor A and D samples. The randomly distributed fibers and variation in the FLD (Section 2.3.2) across the LFT composite collectively contributed to the significant standard deviation. Various studies [23, 25, 43] have reported that flexural, tensile, and impact properties of GF-reinforced PP composite materials are highly influenced by fiber length, porosity, fiber weight fraction, and fiber orientation.

Influence of fiber length

The results presented in Section 2.3.2 show that average fiber length in random LFT composites (3.07 mm) was higher than Tecnogor A (1.15 mm) and D (0.69 mm) composites. Therefore, random LFT composites were anticipated to possess high mechanical properties with a higher average fiber length. Despite the lower average fiber length compared with the random LFT samples, Tecnogor A and D showed superior mechanical performance than the random LFT samples. This suggests that fiber alignment had a more dominant influence over fiber length. This observation is based on the higher mechanical performance of Tecnogor composites.

Influence of fiber porosity

Tecnogor A, Tecnogor D, and random LFT samples had total porosity content less than 1% as described in Section 2.3.2. According to Mehdikhani et al. [44], the void content less than 1% is insensitive and has a negligible effect on the mechanical performance of fiber reinforced composites. Hence, minimal porosity was also not the primary reason for the higher mechanical performance of Tecnogor A and D compared with the random LFT samples.

Effect of fiber weight fraction

As per the TGA results presented in Section 2.3.1, Tecnogor A, Tecnogor D, and random LFT samples had an average GF content of 48.40, 45.45, and 42.40 wt %, respectively. Fiber weight fraction could be one of the reasons for the better performance of the aligned Tecnogor composites compared with the random LFT composite. Thus, to have a proper baseline for comparison of mechanical test results, raw mechanical data were normalized using Eq. (2.2) to a specified GF volume content of LFT composite (42.40 wt %). The following formula is taken from the MIL-HDBK-17 handbook, Section 2.4.3 [45].

$$Normalized\ value = Test\ value\ \times \frac{CPT_{specimen}}{CPT_{batchavg.}} \times \frac{FV_{normalizing}}{FV_{batchavg.}} \qquad \text{(Eq 2.2)}$$

where $CPT_{specimen}$ is the composite panel thickness corresponding to individual specimen thickness, $CPT_{batchavg.}$ is the average composite sample thickness calculated from a thickness measurement of respective batch of specimens, $FV_{normalizing}$ is the fiber volume fraction specified or chosen for normalizing, and $FV_{batchavg}$ is the batch average fiber volume fraction measured from a number of panels through thermal measurements.

Equation 2.2 is based on two fundamental assumptions. The first assumption is that fiber-dominated strength and stiffness properties vary linearly with fiber volume fraction, and the second is that the panel thickness and fiber volume fraction are virtually linear up to 65% fiber volume fraction.

Table 2.6 and Figure 2.10 shows the normalized mechanical properties of Tecnogor A, Tecnogor D, and random LFT composites. The normalized flexural, tensile, and impact properties of Tecnogor A and D samples demonstrated excellent performance compared with the random LFT sample. The normalized flexural strength and modulus of Tecnogor A and D in the X direction were approximately 44%~26% and 138%~116% higher, respectively, than the random LFT composite. Similarly, normalized tensile strength and modulus of Tecnogor A and D in the X direction were approximately 33%~30% and 53%~56% higher, respectively, than the random LFT composite. The normalized data show that the fiber weight fraction was less of a factor affecting the flexural, tensile, and impact properties.

Influence of fiber orientation

The composites were much stiffer and stronger in the direction of major fiber orientation than the transverse direction [46]. Flexural properties (strength and modulus) of Tecnogor A, Tecnogor D, and random LFT samples in the fiber flow direction (X direction) were 124%~178%, 88%~162%, and 45%~44% higher, respectively, than in the transverse direction (Y direction). Similarly, tensile properties (strength and modulus) of Tecnogor

Table 2.6: Normalized mechanical properties of Tecnogor A, Tecnogor D, and random LFT for 42.40 wt % fiber.

Mechanical testing			**Tecnogor A**		**Tecnogor D**		**Random LFT**	
			X dir	**Y dir**	**X dir**	**Y dir**	**X dir**	**Y dir**
Flexural	Strength (MPa)	Mean	179.66	79.97	156.73	83.14	124.30	85.71
		STD	2.60	3.16	9.15	3.17	22.00	4.65
	Modulus (GPa)	Mean	9.88	3.55	8.98	3.43	4.15	2.88
		STD	0.18	0.33	0.31	0.17	0.64	0.27
Tensile	Strength (MPa)	Mean	71.15	28.40	69.43	27.03	53.42	36.02
		STD	2.23	0.28	3.46	0.30	7.66	6.97
	Modulus (GPa)	Mean	7.57	3.69	7.73	4.16	4.95	3.43
		STD	0.69	0.62	0.57	0.38	0.84	0.43
Izod	Impact energy (KJ/m^2)	Mean	9.32	4.89	10.76	4.59	3.60	—
		STD	0.74	0.28	0.67	0.36	0.86	—

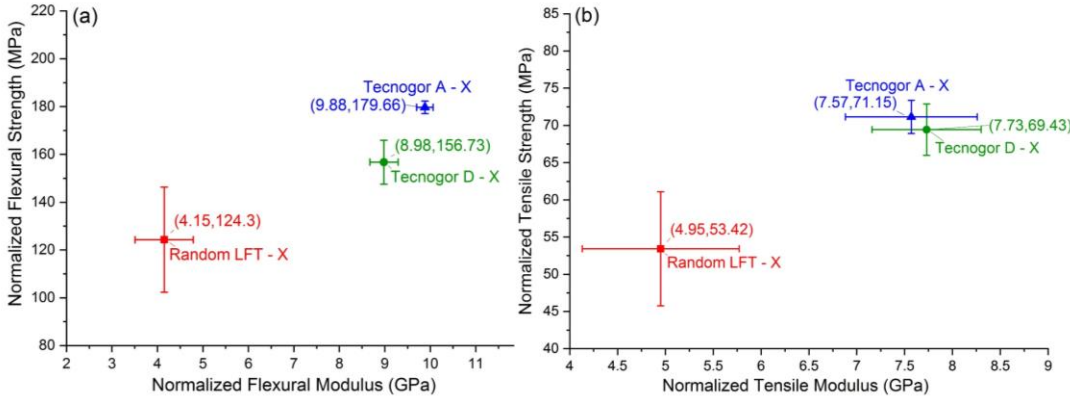

Figure 2.10: Normalized mechanical properties of Tecnogor A, Tecnogor D, and random LFT samples for 42.40 wt % fiber; (a) normalized flexural strength versus normalized flexural modulus, and (b) normalized tensile strength versus normalized tensile modulus.

A, Tecnogor D, and random LFT samples in the X direction were 151%~93%, 157%~86%, and 48%~44% higher than the Y direction, respectively. Thus, the data suggest that Tecnogor A and D composites had an average variation of 151%~125% in flexural, 122%~121% in tensile, and 91%~134% in impact properties between the fiber flow direction (X direction) and transverse direction (Y direction). The Tecnogor D sample exhibited higher impact resistance (~16%), higher tensile modulus (~2%), and lower/comparable tensile strength (~2%) than the Tecnogor A sample (see Table 2.6 and Figure 2.9) despite the low fiber fraction and FLD.

Thus, collectively, we conclude that highly oriented fibers are the most contributing parameter to the overall mechanical performance of LFT composites.

Theoretical Approach

The elastic properties of the discontinuous aligned fiber composites and random fiber composites can be predicted theoretically by adopting semi-empirical approaches [3, 47]. For aligned fiber composites, the tensile modulus was predicted using the following Halpin-Tsai [48] Eqs. (2.3) and (2.4). These equations assume that the fiber cross-section is circular, perfect bonding exists between fibers and the matrix, fibers are uniformly distributed throughout the matrix, and the matrix is free of voids. The longitudinal modulus of a discontinuous fiber composite is given by [3]

$$E_x = \frac{1 + 2(l/d)\eta_L \mathcal{V}}{1 - \eta_L \mathcal{V}} E_m \qquad \text{(Eq 2.3)}$$

and the transverse modulus of a discontinuous fiber composite is given by

$$E_y = \frac{1 + 2\eta_T \mathcal{V}}{1 - \eta_T \mathcal{V}} E_m \quad \text{(Eq 2.4)}$$

where $\eta_L = \frac{E_f/E_m - 1}{E_f/E_m + 2(l/d)}$, $\eta_T = \frac{E_f/E_m - 1}{E_f/E_m + 2(l/d)}$, (l/d) = fiber aspect ratio, $\mathcal{V}$ = fiber volume fraction, E_f = fiber modulus, and E_m = matrix modulus.

Lavengood and Goettler [49] predicted tensile modulus of a 3D randomly oriented discontinuous fiber composite and it is estimated using Eq. (2.5).

$$E_c = \frac{1}{5} E_x + \frac{4}{5} E_y \quad \text{(Eq 2.5)}$$

where E_c is the composite modulus. The longitudinal (E_x) and transverse (E_y) moduli can be calculated using the Halpin-Tsai Eqs. (2.3) and (2.4), respectively. The tensile modulus of the aligned Tecnogor A and D samples was estimated using Eqs. (2.3) and (2.4), whereas the tensile modulus of the random LFT samples was estimated using Eq. (2.5). The following parametric data were used: E_f = 55 GPa [14], E_m = 1.25 GPa [33]. Based on initial fiber length and diameter of feedstock, the aspect ratio (l/d) of Tecnogor A, Tecnogor D, and random LFT samples were 500, 609, and 786. However, when the aspect ratio is greater than 100, the mean fiber length or aspect ratio has nearly no influence on the elastic modulus of composites [47]. Hence, the appropriate critical value of (l/d) = 100 is used.

Table 2.7 represents the theoretically predicted tensile modulus compared with experimental results. The predicted transverse moduli of Tecnogor A, D and random LFT samples were 3%~13% lower than the test data. Also, the predicted longitudinal modulus of the random LFT sample was ~13% lower than the test data. However, the differences are within the range of standard errors of experimental data.

Table 2.7: Comparison of theoretical and experimental results of longitudinal and transverse moduli of Tecnogor A, Tecnogor D, and random LFT composites.

Tensile modulus	**Tecnogor A**		**Tecnogor D**		**Random LFT**	
	X dir	**Y dir**	**X dir**	**Y dir**	**X dir**	**Y dir**
Theoretical (GPa)	24.68	4.35	23.10	4.02	4.32	2.98
Experimental (GPa)	8.64	4.48	8.28	4.46	4.95	3.43
Difference (%)	186	2.90	179	9.87	12.72	13.11

On the other hand, the predicted longitudinal moduli of Tecnogor A and D were much higher than the experimental data (Table 2.7). It is usually laborious to perfectly align fibers in a LFT composite sheet using the aligned extrusion process. Therefore, partial fiber alignment is typical in any molded LFT composite [47]. However, the Halpin-Tsai equations predict the elastic modulus assuming perfectly aligned fibers with a uniform FLD. This could be the reason for the overestimation of the elastic modulus.

Fu et al. [50] investigated the effects of the FLD and FOD on the elastic modulus of short fiber reinforced polymers using a paper physics approach. Their study demonstrated that when fiber volume fraction was around 10%, the composite elastic modulus reduced by ~106% with increasing mean fiber orientation varying from 0° to 48.5°. At a high fiber volume fraction (in the range of 30% to 50%), the composite elastic modulus decreased dramatically by ~205% on an average with increasing mean fiber orientation from 0° to 48.5°. Their study shows that the fiber orientation highly influences the mechanical performance of the composite.

2.3.4 Statistical Analysis

As mentioned in Section 2.3.3, the fiber orientation significantly impacts the mechanical performance of the LFT composites. To investigate if there is enough evidence to suggest the Tecnogor composites have different fiber orientation from the random LFT composites, statistical hypothesis testing using SPSS software (IBM SPSS statistics, version 26) was performed [51]. The testing of assumption of no difference (null hypothesis) performed by observing whether orientation data was plausibly consistent with it. Equations (2.6) and (2.7) represents the null and alternative hypothesis used for hypothesis testing, respectively.

The null hypothesis was that the average fiber orientation is the same in Tecnogor A, Tecnogor D, and random LFT samples.

$$H_0\text{: } \mu_A = \mu_D = \mu_{random} \qquad \text{(Eq 2.6)}$$

The alternative hypothesis was that the average fiber orientation is different in Tecnogor A, Tecnogor D, and random LFT samples.

$$H_0\text{: } \mu_A \neq \mu_D \neq \mu_{random} \qquad \text{(Eq 2.7)}$$

The ANOVA F-test was an appropriate test for the equality of means across the three samples (Tecnogor A, D and random LFT). The fiber orientations of Tecnogor A, Tecnogor D, and random LFT samples were assessed by comparing their means. Table 8 represents the SPSS ANOVA and Scheffe post hoc comparisons test output. The output illustrates that mean fiber orientation of Tecnogor A and D samples were 26.85° and 26.36°, respectively. However, these differences are not statistically significant (F-ratio = 1,716.86, p = 0.066). On the contrary, the mean fiber orientation of random LFT sample was 42.39° and it was statistically significant (F-ratio = 1,716.86, p = 0.000) compared with Tecnogor A and D samples. The outcome of the statistical study suggests that the fiber orientation is different in random LFT composites processed using ECM compared with Tecnogor composites sheet-processed via the aligned extrusion process.

Table 2.8: One-way ANOVA and Scheffe post hoc multiple test output showing F-ratio with appropriate probability and a comparison of mean fiber orientation for each composite sample against one another. Output adapted from SPSS software, version 26.

One-way ANOVA: Fiber orientation of each composite sample

	Sum of squares	df	Mean square	F	Sig.
Between groups	1614578.781	2	807289.391	1716.858	0.000
Within groups	22258013.003	47336	470.213		
Total	23872591.784	47339			

Scheffe post hoc multiple comparisons tests
Dependent variable: Fiber orientation of each composite sample

(I) Composite material	(J) Composite material	Mean difference (I-J)	Std. error	Sig.	95% confidence interval Lower bound	95% confidence interval Upper bound
Tecnogor A	Tecnogor D	0.508644	0.218068	0.066	−0.02515	1.04244
	Random LFT	−15.531687*	0.289332	0.000	−16.23992	−14.82345
Tecnogor D	Tecnogor A	−0.508644	0.218068	0.066	−1.04244	0.02515
	Random LFT	−16.040331*	0.292081	0.000	−16.75529	−15.32537
Random LFT	Tecnogor A	15.531687*	0.289332	0.000	14.82345	16.23992
	Tecnogor D	16.040331*	0.292081	0.000	15.32537	16.75529

Scheffe[a,b] homogeneous subsets: Fiber orientation of each composite sample

Composite material	N	Subset for Alpha = 0.05: 1	2
Tecnogor D	19133	26.35591	
Tecnogor A	20464	26.86455	
Random LFT	7742		42.39624
Sig.		0.167	1.000

2.4 Summary

In this study, DSC data illustrated 19.75%~13.20% improved degree of crystallinity in the case of Tecnogor A and D compared with the random LFT composites, respectively. FLD measurements demonstrated ~83%, ~90%, and ~72% fiber attrition during manufacturing of Tecnogor A, D and random LFT composites. In Tecnogor A and D samples, the mean fiber length did not significantly deviate with sample locations. However, in the random LFT samples, the mean fiber length was highly dependent on sample locations. The processing conditions strongly affected the size, shape, and location of pores in the composites. The porosity level was below 1% in Tecnogor A, Tecnogor D, and random LFT composites, which provides enough evidence of optimal manufacturing. Mechanical testing reveled that the Tecnogor composites had better flexural, tensile, and Izod impact properties than the random LFT composites. Even normalized mechanical results highlighted that the Tecnogor composites had superior mechanical properties over the random LFT composites. The theoretically predicted transverse moduli of Tecnogor A, Tecnogor D, and random LFT samples using Halpin-Tsai and Lavengood-Goettler models were moderately close to the experimental data but lower by 3%~13%. The differences are within the range of standard deviation of experimental data. However, the predicted longitudinal moduli of Tecnogor A and D were much higher than the experimental data because of the partial fiber alignment in the Tecnogor composites. Around 48% of fibers in the Tecnogor composites had preferential orientation in the range of 0° to 20° in the θ direction compared with ~24% in the random LFT samples. Statistical analysis disclosed that the fiber orientation of the Tecnogor composites was different from that of the random LFT composites.

In summary, despite the reduced FLD, LFT composites can achieve superior mechanical performance with highly aligned fibers. Therefore, by understanding the process-microstructure-property relationships and mechanisms, tuned anisotropy, improved quality, and functionality for end-use applications can be accomplished.

References

[1] Bartus SD, Vaidya UK. Performance of long fiber reinforced thermoplastics subjected to transverse intermediate velocity blunt object impact. Composite Structures 2005;67(3):263-277.

[2] Emerson D, et al. Using unidirectional glass tapes to improve impact performance of thermoplastic composites in automotive applications. In: Proceedings of the 12th Annual Automotive Composite Conference and Exhibition ACCE 2012; Troy, Michigan, USA.

[3] Mallick PK. Fiber-reinforced composites: materials, manufacturing, and design. 3rd ed. CRC Press: 2008.

[4] Vaidya U. Composites for automotive, truck and mass transit: Materials, design, manufacturing. DEStech Publications, Inc: 2011.

[5] Chawla KK. Composite materials: science and engineering. Springer Science & Business Media: 2012.

[6] Chithambaram S, and Senthilvelan S. Abrasive behavior of discontinuous fiber reinforced polypropylene material. Industrial Lubrication and Tribology 2010;62:187-196.

[7] Xu Y, et al. A new way of strengthening and toughening for carbon fiber reinforced polyphenylene sulfide (CF/PPS) composites via matrix modification. Journal of Wuhan University of Technology-Mater. Sci. Ed. 2017;32(6):1318-1322.

[8] Ning H, et al. A review of Long fibre thermoplastic (LFT) composites. International Materials Reviews 2019;64(1):1-25.

[9] Wang J, et al. Shear induced fiber orientation, fiber breakage and matrix molecular orientation in long glass fiber reinforced polypropylene composites. Materials Science and Engineering: A 2011;528(7):3169-3176.

[10] Hartness T, et al. The characterization of low cost fiber reinforced thermoplastic composites produced by the DRIFT™ process. Composites Part A: Applied Science and Manufacturing 2001;32(8):1155-1160.

[11] Hudson LA, VUK, Dean DR, Pillay S, Shih AM. Design, analysis and development of optimized thermoplastic pultruded profiles. Thesis 2009.

[12] Balaji Thattaiparthasarathy K, et al. Process simulation, design and manufacturing of a long fiber thermoplastic composite for mass transit application. Composites Part A: Applied Science and Manufacturing 2008;39(9):1512-1521.

[13] Roux C, Denault J, Champagne MF. Parameters regulating interfacial and mechanical properties of short glass fiber reinforced polypropylene. Journal of Applied Polymer Science 2000;78(12):2047-2060.

[14] Alwekar S, et al. Manufacturing and characterization of continuous fiber-reinforced thermoplastic tape overmolded long fiber thermoplastic. Composites Part B: Engineering 2021;207:108597.

[15] Markarian J. Long fibre reinforcement drives automotive market forward. Plastics, Additives and Compounding 2005;7(3):24-29.

[16] Shioya M, Kikutani T. Synthetic Textile Fibres: Non-polymer Fibres. In: Sinclair R, editor. Textiles and Fashion. Woodhead Publishing, 2015. p.139-155.

[17] SABIC. PP glass fiber compounds for structural automotive applications. 2019; Available at: https://www.sabic.com/assets/zh/Images/AUTO-STR-ES-001-EN-061319-WEB_tcm11-18751.pdf.

[18] Wilson M. Finite element analysis of glass fibre reinforced thermoplastic composites for structural automotive components. University of Nottingham: 2003.

[19] Long glass PP concentrate focused on automotive components.(engineering materials). British Plastics & Rubber 2008;28.

[20] Hufenbach W, et al. Polypropylene/glass fibre 3D-textile reinforced composites for automotive applications. Materials and Design 2011;32(3):1468-1476.

[21] Alwekar S, et al. Manufacturing and characterization of continuous fiber-reinforced thermoplastic tape overmolded long fiber thermoplastic. Composites Part B: Engineering 2020;108597.

[22] Naik PS, Orangalu SA, Londhe NV. Effect of fiber weight fraction on mechanical properties of carbon–carbon composites. Polymer Composites 2012;33(8):1329-1334.

[23] Thomason JL, et al. Influence of fibre length and concentration on the properties of glass fibre-reinforced polypropylene: Part 3. Strength and strain at failure. Composites Part A 1996;27(11):1075-1084.

[24] Thomason JL. The influence of fibre length and concentration on the properties of glass fibre reinforced polypropylene: 7. Interface strength and fibre strain in injection moulded long fibre PP at high fibre content. Composites Part A: Applied Science and Manufacturing 2007;38(1):210-216.

[25] Thomason JL, Vlug MA. Influence of fibre length and concentration on the properties of glass fibre-reinforced polypropylene: 1. Tensile and flexural modulus. Composites Part A: Applied Science and Manufacturing 1996;27(6):477-484.

[26] Patil H, Tiwari RV, Repka MA. Hot-Melt Extrusion: from Theory to Application in Pharmaceutical Formulation. AAPS PharmSciTech 2016;17(1):20-42.

[27] Alwekar SP, Kore SS, Uday V. Comparison of long fiber thermoplastics produced via directional extrusion versus extrusion compression molding, TP18-0571. In: CAMX- The Composites and Advanced Materials Expo, CAMX Conference Proceedings. 2018, Society for the Advancement of Material and Process Engineering (SAMPE): Dallas, Texas.

[28] Papathanasiou TD, Ingber MS, Guell DC. Stiffness enhancenment in aligned, short-fiber composites: A computational and experimental investigation. Composite Science and Tecnology 1995:1-9.

[29] Teixeira D, et al. Influence of flow restriction on the microstructure and mechanical properties of long glass fiber-reinforced polyamide 6.6 composites for automotive applications. Materials and Design 2013;47:287-294.

[30] Okine RK, Edison DH, Little NK. Properties and Formability of an Aligned Discontinuous Fiber Thermoplastic Composite Sheet. Journal of Reinforced Plastics and Composites 1990;9(1):70-90.

[31] Renolit. Renolit Tecnogor. Available at: https://www.renolit.com/en/industries/automotive/parcel-shelf/renolit-tecnogor.

[32] Kunc V, et al. Fiber length distribution measurement for long glass and carbon fiber reinforced injection molded thermoplastics. In: SPE Automotive and Composites Divisions - 7th Annual Automotive Composites Conference and Exhibition. 2007.

[33] Yeole P, et al. Characterization of textile-grade carbon fiber polypropylene composites. Polymers and Polymer Composites 2020;0967391120930109.

[34] Buades A, Coll B, Morel JM. A non-local algorithm for image denoising. In: Computer Vision and Pattern Recognition 2005.

[35] Thermo Fisher Scientific Avizo Software 9 user's guide, FEI SAS. Thermo Fisher Scientific.

[36] Lee SY, et al. Thermal, mechanical and morphological properties of polypropylene/clay/wood flour nanocomposites. Express Polymer Letters 2008;2(2):78-87.

[37] Zhang D, et al. Effect of fiber length and dispersion on properties of long glass fiber reinforced thermoplastic composites based on poly(butylene terephthalate). RSC Advances 2017;7(25):15439-15454.

[38] Peterlin, A., Crystallization from a strained melt or solution %J Polymer Engineering and Science. Polymer Engineering and Science, 1976. **16**: p. 126-137.

[39] Yeole P, et al. Mechanical Characterization of High-Temperature Carbon Fiber-Polyphenylene Sulfide Composites for Large Area Extrusion Deposition Additive Manufacturing. Additive Manufacturing 2020;34:101255.

[40] Willems F, Bonten C. Influence of processing on the fiber length degradation in fiber reinforced plastic parts. AIP Conf Proc 2016;1779(1):020003.

[41] Kumar V, et al. Internal arcing and lightning strike damage in short carbon fiber reinforced thermoplastic composites. Composites Science and Technology 2021;201:108525.

[42] Kumar V, et al. High-performance molded composites using additively manufactured preforms with controlled fiber and pore morphology. Additive Manufacturing 2020:101733.

[43] Thomason JL, Vlug MA. Influence of fibre length and concentration on the properties of glass fibre-reinforced polypropylene: 4. Impact properties. Composites Part A: Applied Science and Manufacturing 1997;28(3):277-288.

[44] Mehdikhani M, et al. Voids in fiber-reinforced polymer composites: A review on their formation, characteristics, and effects on mechanical performance. J Comp Mater 2019;53(12):1579-1669.

[45] US Department of Defense. MIL-HDBK-17-1F: Composite materials handbook. 2002. 1:70-74.

[46] Major factors affecting the performance of short fibre reinforced polymers. In: Fu SY, Lauke B, Mai YW, editors. Science and Engineering of Short Fibre Reinforced Polymer Composites. Woodhead Publishing, 2009. p.29-58.

[47] Elastic modulus of short fibre reinforced polymers, In: Fu SY, Lauke B, Mai YW, editors. Science and Engineering of Short Fibre Reinforced Polymer Composites. Woodhead Publishing, 2009. p.119-163.

[48] Halpin JC. Stiffness and Expansion Estimates for Oriented Short Fiber Composites. J Compos Mater 1969;3(4):732-734.

[49] Lavengood R, Goettler L. Stiffness of non-aligned fiber reinforced composites. Monsanto Research Corp: St Louis, Missouri, USA, 1971.

[50] Fu SY, Lauke B. The elastic modulus of misaligned short-fiber-reinforced polymers. Composites Science and Technology 1998;58(3):389-400.

[51] IBM SPSS Statistics for Windows, Version 26.0. Armonk, New York: IBM Corp, 2019.

3. CHAPTER 3

MANUFACTURING AND CHARACTERIZATION OF CONTINUOUS FIBER-REINFORCED THERMOPLASTIC TAPE OVERMOLDED LONG FIBER THERMOPLASTIC*

*Shailesh Alwekar, Ryan Ogle, Seokpum Kim, Uday Vaidya, Manufacturing and characterization of continuous fiber-reinforced thermoplastic tape overmolded long fiber thermoplastic. ***Composites Part B: Engineering***, *2021. 207: p. 108597. DOI: 10.1016/j.compositesb.2020.108597.*

Abstract

Light-weight construction, design freedom, integration of functions, and compelling cost element are desired by Original Equipment Manufacturers (OEMs) and their suppliers. The emergence of overmolding of continuous-discontinuous reinforcement enables design freedom and ability to tailor stiffness, strength, and damage tolerance for structural applications. In this work, long fiber thermoplastics (LFT) are overmolded with continuous fiber-reinforced thermoplastic (CFRTP) tape are combined using extrusion compression molding process to evaluate the structural performance. The CFRTP tape overmolded LFT samples were characterized using nondestructive and destructive techniques to track fiber alignment, fiber distribution, manufacturing defects, interfacial bonding of the tape – LFT and effect of CFRTP tape on LFT. Mode 1 fracture toughness, G_{1c} for tape overmolded LFT was higher by 25~30% compared to literature reported G_{1c}. This response was attributed to excellent fiber distribution, good fiber wetting, and absence of voids at the interface. Three-point bend test indicated that CFRTP tape overmolded LFT composites were better able to resist damage under the bending load compared to constituent LFT composite. Flexural strength of the overmolded composite was higher by 119~142%, and modulus higher by 77~65% compared to constituent LFT composite. Simulated flexural results accurately represents the mechanical behavior of composites. The penetration energy of tape overmolded LFT composites determined by LVI test was in the range of 27.66 to 30.15 J, which is significantly higher than constituent LFT composite, 7.76 J. CFRTP tape overmolded LFT composite exhibits progressive fiber

fracture, matrix cracking, and interfacial debonding failure, whereas constituent LFT composite showed catastrophic fiber fracture.

Keywords: A. Discontinuous reinforcement, A. Tape, C. Computational modeling, D. Non-destructive testing, Extrusion compression molding

3.1 Introduction

Long fiber thermoplastic (LFT) composites are widely used in the automotive and transportation sector. LFT composites provide ease of processability, recyclability, and possess superior specific modulus and strength, excellent impact resistance, excellent corrosion resistance, and infinite shelf life. These advantages enable their increasing use in various applications and make LFT composites one of the most advanced lightweight engineering materials [1].

LFT composites constitute a family of composites, wherein all partially crystalline and amorphous thermoplastics are suitable as thermoplastic matrix materials; reinforced with discontinuous fibers such as natural, glass, carbon, and aramid fibers. Glass fibers used prevailingly as reinforcement due to excellent mechanical properties with low density and at a very reasonable cost [2, 3].

The hot melt impregnation process is used mainly as a manufacturing process for LFT pellets. In this process, collimated continuous fiber tows are pulled into an impregnation chamber, where dry fibers are impregnated with an extruded thermoplastic polymer. The material rapidly cools as it exits the chamber. The rod material is pulled through the puller and pelletized into the desired length. The typical fiber length ranges from 5 to 50 mm [4, 5].

The LFT pellets are molded into the component by typical manufacturing approaches such as injection molding and extrusion-compression molding (ECM). In injection molding, LFT pellets melted into an extruder and further molten charge injected into the closed mold, where it goes under high pressure and hardens to the configuration of the cavity. This process gives highly orientated fiber in the direction of flow, which results in improved mechanical properties of a component in the direction [6, 7]. However, injection molding is associated with fiber attrition due to the high shear witnessed by the fibers as they migrate through the screw and injection nozzle(s). The extent of attrition depends on the type of fiber [8] and the mechanical properties of the resulting parts can be influenced in proportion of attrition [9, 10].

ECM is another method to produce LFT products. Whereas in ECM, the low shear screw design of the plasticator minimizes fiber attrition. Here, LFT pellets fed through the gravimetric feeder and plasticated into the hot barrel. A hot LFT charge extruded, which then placed into the mold cavity and molded into the part. ECM provides various benefits over injection molding, such as- lower fiber attrition, low tooling cost due to simplicity of molds, minimal scrap generation since there are no sprue or runners, low warpage and requires less molding pressure [11-14]. LFTs of approximately 6-25 mm glass fiber (GF) reinforced polypropylene (PP) resin (PP-GF) are used widely in the automotive industry. PP-GF used for components such as front-end carriers, instrument-panel carriers, interior door panels, consoles, pedals, underbody shields, battery box covers etc. [13, 15, 16].

Passenger safety is of utmost priority in vehicles; thus, structural crashworthiness is a vital characteristic in the design of thermoplastic composite components. Therefore, high energy absorbing materials have significant interest in structural and semi-structural applications such as in automotive chassis, B-pillar, side impact beam (SIB), rear floor, bumpers, and liftgate [17, 18].

Sheet molding compound (SMC), glass mat thermoplastic (GMT), and grid stiffened thermoplastic composites are commonly preferred composites for automotive structural components since they provide superior crashworthiness and damage tolerance [19, 20].

SMC is widely used for molding automotive body parts such as grille opening panels, radiator supports, cross car beams, tailgates, and hoods [10]. A typical SMC contains about 50~70% fiberglass reinforcement, 25% thermoset resin (usually unsaturated polyester), and 25~45% filler (usually, calcium carbonate, clay, or kaolin) by weight fraction [20]. SMC offers superior corrosion resistance, better dimension stability, Class A surface finish, lower tooling cost and it can be manufactured in medium to high volumes [21, 22]. Whereas, SMC has limited shelf life, needs special handling since styrene cross-linker is quite volatile and inherent difficulties in recycling makes insuperable obstacles in the development of SMC market [23].

Moghaddam et al. [24] designed an automobile bumper beam by employing GMT material as for energy absorption. Their study revealed that GMT bumper able to convert about 80% kinetic impact energy to potential energy. GMT bumper offers weight reduction of about half when compared to steel bumper.

Beyene et al. [25] analyzed the automotive bumper beam made of GMT as a possible alternative solution to a metal bumper. This study demonstrated that GMT exhibited equivalent structural performance and the energy absorption capability to the metal incumbent. The study demonstrated a reduction in vehicle weight and therefore increases fuel efficiency. Although GMT achieves excellent strength and performance/weight ratio, GMT sheets are relatively 45~78% more expensive than the LFT, even though PP is a low-cost resin [26, 27]. Moreover, the compression processing involves punchouts and other material scrap generation. Post-operation steps like trimming are necessary, which involves costly labor work [28].

Gan et al. [29] investigated the energy absorption characteristics of grid-stiffened thermoplastic composites under transverse loading. They used commingled unidirectional Twintex® E-glass-PP for ribs and commingled woven Twintex® E-glass-PP for the skin. Commingled fibers are laid up into grooves to form the ribs and further skin of commingled woven fabric integrally bonded. This process offers uniform fiber distribution and oriented fibers in the direction of ribs. Despite the several advantages, it is a very time-consuming process and not cost-effective.

Jadhav et al. [30] investigated iso-grid panels with longitudinal rib/skin beams and reported increased energy absorption when loaded on the rib side instead of the skin side. Lee et al. [17] designed the rib stiffened composite side impact beam (SIB), where LFT ribs co-molded with woven glass fabric prepregs. They performed tension and compression tests and found that the specific strength was 130% and 10% higher than steel-made SIB respectively. Their study indicated that rib stiffened composites have the potential to replace the steel incumbent for side impact. However, the use of woven fabric for the skin limits the design freedom.

Thattaiparthasarathy et al. [31] studied rib reinforced LFT composites processed via the ECM technique. It provides design freedom with shorter processing time. On the other hand, the processing complexity increases for features, including ribs, grids, and bosses. The fiber dispersion in ribs and cavities is inadequate due to the high viscosity of charge, which results in fiber agglomeration. Consequently, poor fiber dispersion impedes good interfacial bonding between skin and ribs and increases the voids.

One of the primary goals in designing structures is to provide improvement over the imposed loads without considerable increase in weight, superior crashworthiness, improved efficiency, and compelling cost element. The overmolding approach offers an efficient alternative process to traditional SMC, GMT, and rib reinforced thermoplastic composites.

The overmolding approach it uses pre-consolidated continuous fiber-reinforced thermoplastic (CFRTP) tapes and LFTs. Pre-consolidated tapes were placed in discrete locations in the tool (mold) and followed by extrusion compression molding of LFT. The overmolding process is expected to provide numerous advantages such as: - (a)synergy of constituents, namely LFT and continuous reinforcement; (b) local reinforcement in only needed areas; (c) reduced cost compared to semi-finished products like GMT, GMTex [32, 33] (d) replaces rib and grid structures; (e) enhanced damage tolerance, and (f) superior crashworthiness, in conjunction with reduced weight and recyclability. Minimal literature is available on the manufacturing and characterization of CFRTP tape overmolded LFTs.

In the present work, PP-GF LFT was processed through ECM, and it is overmolded with thin cross-ply laminates fabricated using PP-GF CFRTP tapes. Differential scanning calorimeter (DSC) and Thermo-gravimetric analyzer (TGA) were used to determine the thermal behavior and hence identify the processing limits for the overmolding manufacturing process. CFRTP tape overmolded LFT samples were inspected using nondestructive techniques. Mechanical characterization included- Mode I interlaminar fracture toughness, flexure, interlaminar shear strength (ILSS), and low velocity impact tests. The effect of tape thickness on LFT composite was also studied. A comprehensive microscopic investigation has been carried out on fractured samples to evaluate the constituent and interface. Flexural results were analyzed computationally.

3.2 Experimental

3.2.1 Materials and Methods

Celstran® PP-GF LFT pellets of 11 mm (0.43”) fiber length were obtained from Celanese Corporation with 40 wt % glass fiber and a density of 1.21 g/cc. Polystrand Inc. provided the PP-GF CFRTP in the form of 0.25 mm (0.0098”) thick tape with a fiber content of 62 wt % and areal weight of 0.0349 g/cm2. In the overmolding study, X-ply with [0/90] tape configurations (listed in Table 3.1) were used to fabricate respective CFRTP tape overmolded LFT plates.

Overmolded test coupons processed and prepared in two stages as shown in processing flow chart of overmolding, Figure 3.1. The first stage involved the consolidation of PP-GF CFRTP tape to form a [0/90] cross-ply laminate via compression molding. The 30-metric ton Carver compression press (Model # 3895.4NE1000, Carver, Inc. USA) was used. The tapes were made as follows- CFRTP laminate of 279.4 x 279.4 mm (11"x11") were stacked and placed into the flat tool mounted in the press. The mold was heated to 185°C. As the temperature of the plies reached above the melting temperature, 170°C (measured using thermocouple and thermometer) pressure of 0.11 MPa (16.53 psi) was applied. The dwell cycle was set for 20 minutes and cooled to room temperature to obtain the consolidated laminate. The laminate was cut into strips of 279.4 mm (11") length and 25.4 mm (1") width with a wet tile saw.

The second stage involves pre-consolidated PP-GF CFRTP tape overmolding of PP-GF LFT. From here onward, CFRTP tape overmolded LFTs are referred to as "T-LFT." For overmolding purpose, we used Yamato DP 63C vacuum oven (temperature range of +5°C to 200°C with an accuracy of ±10C), low shear single screw Impco B-20 extrusion plasticator, and 100-ton Beckwood hydraulic press (Beckwood Corporation, Fenton, MO, USA). The PP-GF tape strips were placed parallel and separated by 76.2 mm (3") on the 2.54 mm (0.1") thick steel caul plate (called tape assembly). One-sided Kapton adhesive (product # 1754N13, McMaster-Carr, USA) tape was used to hold PP-GF tape strips in place.

Figure 3.2 (a) shows the consolidated tape strip assembly. The oven was set to 185°C and once it reached that temperature, the CFRTP tape assembly was kept in the oven to heat the tapes to 170°C under 40 kPa vacuum pressure for the fixed time interval. In parallel, a low shear Impco B-20 extrusion plasticator having four heating zones was used

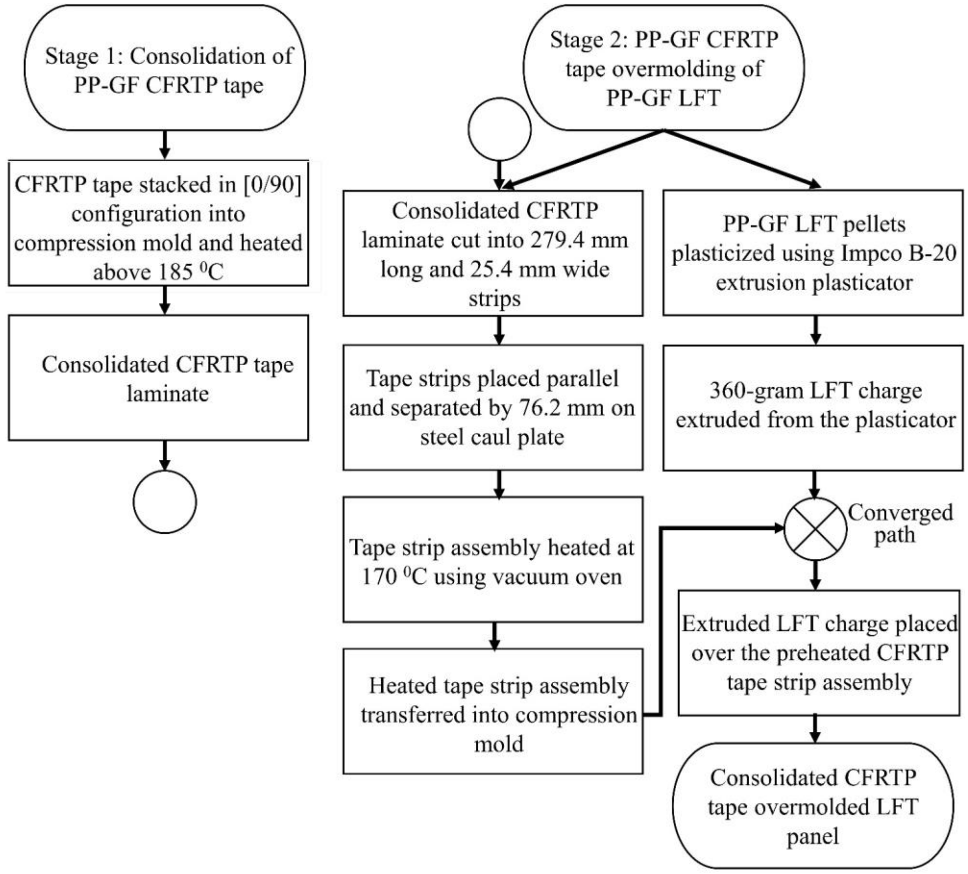

Figure 3.1: Processing flowchart demonstrating the manufacturing layout of CFRTP tape overmolding of LFTs.

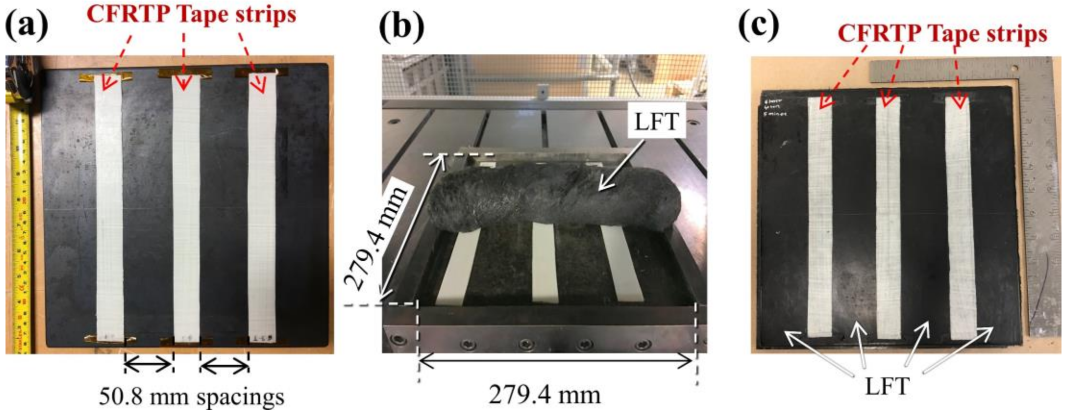

Figure 3.2: (a) PP-GF tape assembly, (b) Extruded LFT charge of diameter 50.8 mm (2”) and length of 170.2 mm (6.70”) placed on preheated tape assembly, and (c) Tape overmolded LFT panel.

Table 3.1: Fabricated configurations with their respective thicknesses

Configuration	Thickness (mm) PP-GF LFT	PP-GF Tape	Overall panel	Extracted coupons for testing
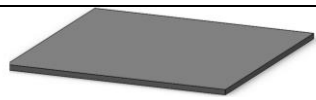 (Baseline) LFT + 0-layer $[0/90]_0$ cross ply tape	3.60	0.00	3.60	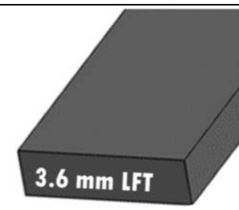 S1 specimen
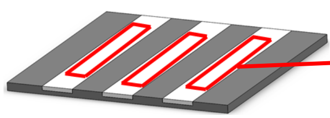 LFT + 6-layer [0/90/0/90/0/90/] cross ply tape	2.40	1.20	3.60	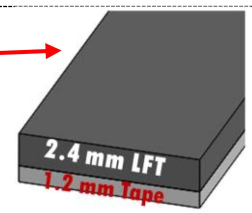 S2 specimen
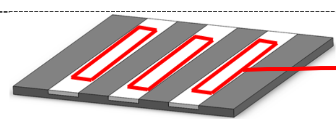 LFT + 9-layer [0/90/0/90/0/90/0/90/0/] cross ply tape	1.80	1.80	3.60	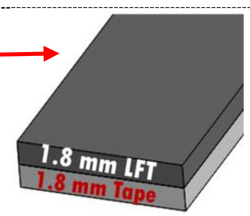 S3 specimen

to plasticize the LFT PP-GF pellets. The heating zones were set to 210, 216, 227, and 227^{o}C respectively (above the melting point of PP). PP-GF LFT pellets were fed into a heated barrel where the glass fibers are uniformly dispersed into a molten polymer (polypropylene) to produce a PP-GF charge. To achieve better compaction without damaging the fibers and fulfill the entire mold cavity, the charge size/mass was optimized and maintained to 50.8 mm (2”) diameter, 170.2 mm (6.70”) length, and a mass of 360 grams on an average.

Once the temperature of consolidated PP-GF tape strips reaches above the melting point of the polymer, the entire assembly was transferred from the vacuum oven into a flat mold mounted in the Beckwood hydraulic press. Immediately after that, the 360-gram PP-GF LFT charge extruded from the plasticator was placed over the preheated CFRTP tape assembly as shown in Figure 3.2 (b). A pressure of 4.56 MPa (661 psi) was applied to enable the PP-GF LFT charge to flow and fill the mold over the tapes. The dwell was set to five (5) minutes prior to demolding, Figure 3.2 (c).

3.2.2 Thermal, Microscopic, Nondestructive, and Mechanical Characterization

The thermal stability and decomposition behavior of PP-GF LFT pellets and PP-GF CFRTP tape was studied using the Q50 TGA (V6.7 Build 203, TA instruments, New Castle, DE, USA). TGA measurements of the samples were carried out in an oxygen environment over a temperature range of 30-700^{o}C at a heating rate of 10^{o}C/min. DSC (Model # 821e, Mettler Toledo, Columbus, OH, USA) was used to evaluate the melting behavior of PP-GF LFT pellets and PP-GF CFRTP tape. The heating cycle of 25^{o}C to 250

^{o}C was set at a heating rate of 10^{o}C/min. To eliminate previous thermal history, an isothermal step of two minutes at 250^{o}C was initiated and cooled down to room temperature subsequently at a rate of 10^{o}C/min. The sample was again reheated with a heating rate of 10 0C/min to obtain the melting peak. The degree of crystallinity (X_c) of the studied samples was determined using Eq (3.1):

$$X_c = \frac{\Delta H_m}{\Delta H^*} \times 100\ \% \qquad \text{(Eq 3.1)}$$

where ΔH_m is melting enthalpy value of a sample measured by DSC, and ΔH^* is the enthalpy value of 100% crystalline PP.

The surface morphology of S2 and S3 T-LFT composites (shown in Table 3.1) was analyzed using Leo 1525 scanning electron microscopy (SEM) (LEO Electron Microscopy Inc., Thornwood, NY, USA) instrument with a low working voltage of 5 KeV. Before scanning, S2 and S3 specimens were polished using sandpapers in consecutive order of 80, 200, 400, 600, 1200, 2000 grits, and then sputtered with the gold of thickness less than 2 nm for 30 sec.

High-resolution X-ray computed tomography (XCT) is used to inspect fiber architecture, manufacturing defects, and interfacial bonding of S2 and S3 T-LFT composites (Table 3.1), nondestructively. The tomograms were performed using Siemens XCT at 80 kV and 200 µA using a tungsten target. A total of 1526 radiographs were acquired for each tomogram with a resolution/voxel size of 8 µm and an exposure time of 8960 ms. The radiographs were collected using a highly sensitive Charged Coupled Device (CCD). 3D tomograms were reconstructed with octopus reconstruction software (version

8.9.4-64 bit) and analyzed using commercial package Simpleware ScanIP (version P-2019.09).

For mechanical testing, (interlaminar fracture toughness, ILSS, and flexural) test coupons S1, S2, & S3 were extracted from T-LFT composite panels using a wet tile saw, see Table 3.1. All the test coupons were prepared and tested at room temperature according to the ASTM standard, as summarized in Table 3.2.

Double beam cantilever (DCB) specimens used to determine Mode 1 interlaminar fracture toughness (G_{1c}) of T-LFT. A total of four specimens of S2 and S3 tested using a 100 KN, MTS frame (Model # 647, MTS Systems Corporation, MN, USA) with a constant crosshead rate of 2 mm/min. Non-adhesive Kapton insert having a thickness of 0.0127 mm (0.0005") was used at the interface as a delamination initiator while preparing the DCB samples. DCB specimens were loaded using one-inch aluminum loading blocks. The bonding surface of the specimens and aluminum blocks were prepared by scrubbing the surface with 60 grit sandpaper. The loading blocks were adhesively bonded to the specimen using a steel-reinforced epoxy adhesive called JB weld. The adhesive was purchased from J-B Weld Company, Sulphur Springs, USA. This is a room temperature cure two-part adhesive with epoxy steel resin and an epoxy steel hardener. The loading blocks were aligned parallel with the specimen and held in position with clamps till the adhesive cured (24 hours).

ILSS and flexural tests were performed using a Test Resources frame (product # 313Q, Test Resources, Minnesota, USA) with 50 KN load cell to determine ILSS and

Table 3.2: Specification of specimens for different mechanical tests

Test	ASTM Standard	Equipment	Avg. thickness (mm)	Avg. width (mm)	Avg. length (mm)
Mode I-interlaminar fracture toughness	D5528	100 KN MTS frame	3.58	25.53	125.90
ILSS	D-2344	50 KN Test Resources frame	3.65	8.23	24.82
Flexural	D-790		3.64	13.51	80.10
Low velocity impact	D7136	Dynatup 8250 drop tower	3.67	100	150

flexural properties of T-LFT. For ILSS and flexural tests, a total of seven samples of S1, S2, and S3 were tested at a crosshead rate of 1 and 1.845 mm min-1 respectively. All the samples were loaded from the LFT side (LFT-side in compression and tape-side in tension). The fractured samples of ILSS and flexural tests were analyzed using the Leo 1525 SEM instrument with a working voltage of 3 KeV.

Low velocity impact (LVI) tests were carried out using Instron® Dynatup 8250 drop tower (Norwood, MA, USA) impact tester. A 16 mm hemispherical impactor with a weight of 3.37 kg was used to test for LVI. The fixture has a circular opening of diameter of 76 mm. The test sample is clamped in the fixture between two aluminum plates. All the samples were prepared and tested based on the ASTM D7136 standard (see Table 3.2). LFT and the T-LFT panels were impacted at the geometric center for different impact energy levels (or height of drop). All panels loaded from the LFT side were impacted from three different heights, 40, 70, and 120 mm, respectively.

3.3 Results and Discussion

3.3.1 Thermal Analysis

Figure 3.3 shows the TGA results for the PP-GF LFT pellets and PP-GF CFRTP tape. TGA curves demonstrate the single-stage decomposition over the entire range of temperature. Less than 0.5% weight loss was observed up to 260^{o}C for both tape and LFT. This indicates the thermal stability of the PP phase. It also seen that the thermal stability is independent of fiber percentage and fiber length. The thermal degradation of PP-GF LFT pellets and

PP-GF tape started around 275°C, with the final degradation temperature of 420°C. At 650°C, the residual amount indicates the glass fiber content in the PP-GF LFT pellets (42.13 wt %) and PP-GF tape (60.01 wt %) respectively.

The melting and crystallization behavior of PP-GF LFT pellet and PP-GF CFRTP tape was investigated using DSC. Figures 3.4 (a, b) shows the DSC results. Table 3.3 summarizes the peak melting temperature (T_m), peak crystallization temperature (T_c), and melting enthalpy (H_m) for the PP phase in the pellet and tape. The melting temperature of PP-GF LFT pellet and PP-GF tape was observed around 163.23°C and 162.22°C respectively. The fiber percentage, continuous (tape), and/or discontinuous (LFT) fiber forms of GF did not significantly influence the melting temperature of the PP matrix. To calculate the degree of crystallinity, ΔH^* is assumed to be 209 J/g for crystalline PP [34]. The degree of crystallinity, X_c for PP-GF LFT pellet, and PP-GF tape was 23.84% and 12.00% respectively. However, in literature [35], it is reported that constituent PP has higher degree of crystallinity (ranges from 41.4% - 47.9%), and it is due to the regular and orderly arrangement of molecular chains of PP in a 3D crystal structure. The addition of glass fiber disturbs this ordered structure and reduces the crystallinity of the pure PP [36]. Besides that, it is also mentioned that the degree of crystallinity of PP reduces as the GF percentage increases in PP-GF composites. DSC and TGA data helped to identify the lower (163°C) and upper (260°C) processing temperature limits for the overmolding studies in this work.

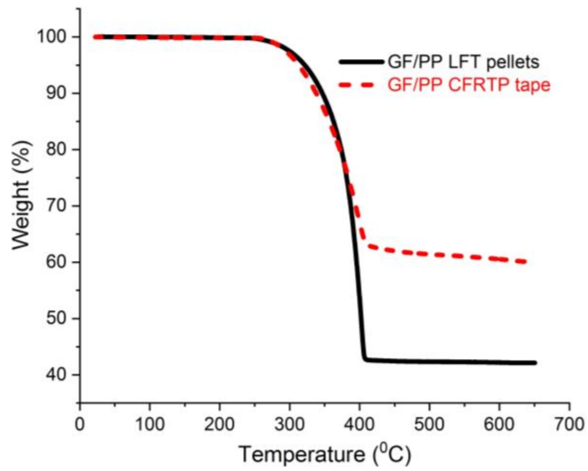

Figure 3.3: TGA thermogram of PP-GF LFT pellets and PP-GF CFRTP tape shows single stage decomposition over the entire range of temperature and PP phase thermally stable up to 260^{o}C.

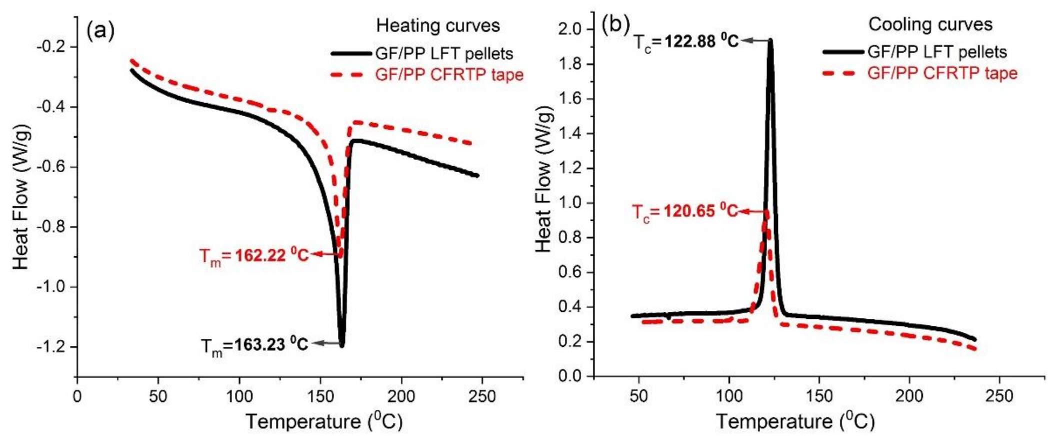

Figure 3.4: DSC thermograms of PP-GF LFT pellets and PP-GF CFRTP tape; (a) Melting behavior with peak melting temperature (T_m), and (b) Crystallization behavior with peak crystallization temperature (T_c).

Table 3.3: Melting and crystallization properties of PP-GF LFT and PP-GF CFRTP tape

Material	T_m (°C)	H_m (J/g)	T_c (°C)	X_c (%)
PP-GF LFT pellet	163.23	49.83	122.88	23.84
PP-GF CFRTP tape	162.22	25.10	120.65	12.00

3.3.2 Inspection of T-LFT Composite

SEM Microscopy

The bonding between CFRTP tape and LFT is critical to transfer load effectively from LFT to CFRTP tape. Initial manufacturing trials revealed that unheated tape tends to debond from the LFT substrate. If heated above the melting temperature, it renders a strong interfacial bond. Figure 3.5 shows SEM micrographs of the polished through-thickness cross-sectional area of the S2 and S3 T-LFT composite. In S2 and S3 T-LFT composite (Figure 3.5 b, d), the LFT side shows well-dispersed glass fibers within the PP matrix. It clearly shows that the fibers are wetted by the PP matrix. The CFRTP tape side shows uniform distribution of aligned fibers with good wetting of the fibers. Both S2 and S3 T-LFT composite (Figure 3.5 a, c) exhibit optimal development of the interface between CFRTP tape and LFT. Both T-LFT composite samples indicate surface voids. We infer these occur during sample preparation or could have developed during the manufacturing process; however, these are limited to the surface as evidenced by microscopic studies. Both S2 and S3 T-LFT composite samples were inspected nondestructively using the XCT technique.

XCT Characterization

Figures 3.6 (a, b) show grayscale XCT images of S2 and S3 T-LFT composites, respectively. Both grayscale images show four characteristic phases identified by A, B, C, and D. In the figure- A-the black background not part of the sample, B- long glass fiber,

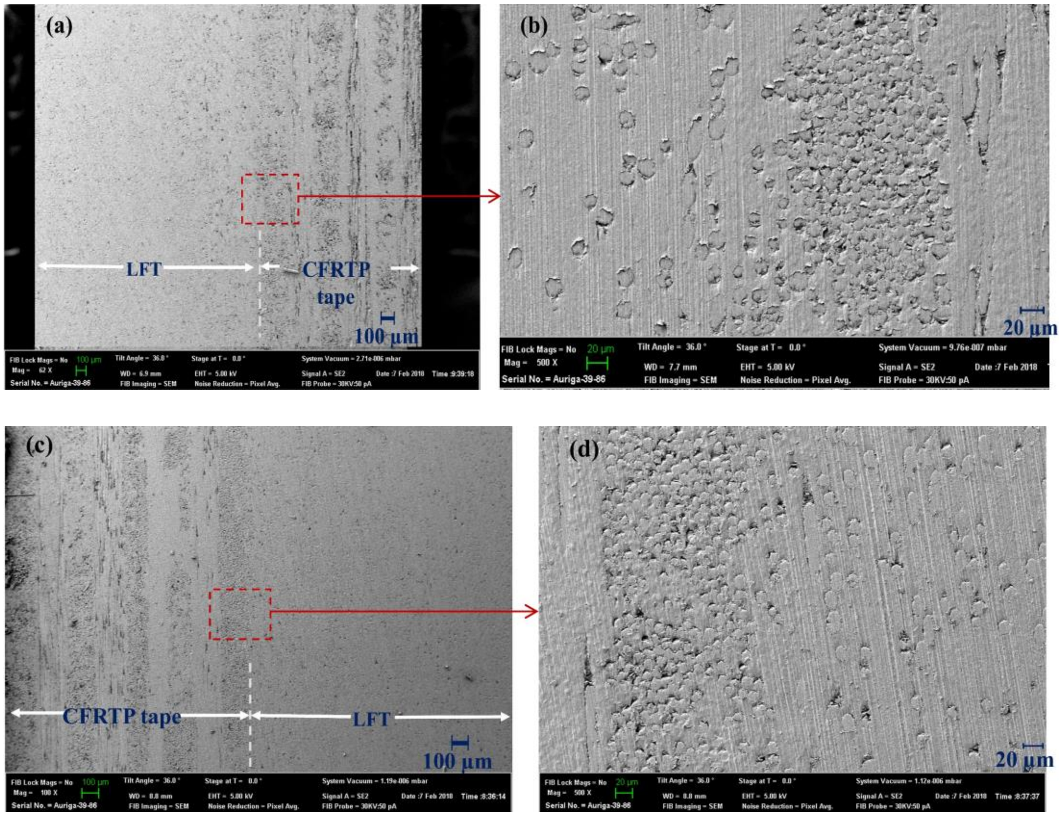

Figure 3.5: SEM micrographs of the polished cross-sectional area of S2 (a, b), and S3 (c, d) T-LFT composite indicating good fiber wetting and fiber distribution.

C- continuous glass fibers, and D- PP matrix. These images reveal the fiber architecture, fiber alignment, and dispersion of fibers within the CFRTP tape and LFT. In S2 and S3 T-LFT composite, the LFT constituent displays well distributed long glass fibers with relatively lesser agglomeration, while CFRTP tape is well aligned fiber in both directions with very limited fiber waviness. The tape stays straight through the process which indicates optimal processing conditions.

The porosity or void level present in composite influences the overall performance of the composite. Hence, it is essential to know actual porosity value. XCT technique can provide the amount, size and shape of the voids exists in the composite. However, when studying GF reinforced polymer composite, artifacts do occur due to the significant density difference between GF (density of GF is 2.55 g/cc) and matrix (density of PP is 0.92 g/cc) [37]. Artifacts are visualized structures which are not present in the investigated object. These artifacts severely affect when information regarding size and shape of voids, manufacturing defects, and interfacial bonding is essential. These artifacts minimized by Octopus image reconstruction software (version 8.9.4.9-64 bit) which is used to reconstruct three-dimensional object [38].

The reconstructed images processed via image processing software Simpleware ScanIP (version P-2019.09) to identify and separate different phases within the scan as well as to extract quantitative and qualitative information such as interfacial bonding, manufacturing defects, and accurate determination of size and shape of voids present in the composite [39]. Here, we performed the line segmentation process on characteristic phases by using visual aid tools such as brightness and contrast to represent the greyscale values

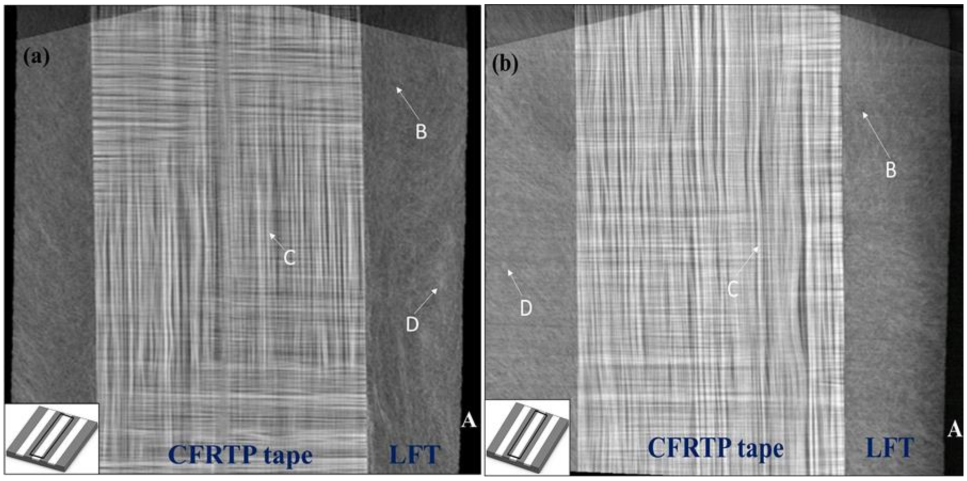

Figure 3.6: Greyscale 2D tomographic slices along the thickness direction for; a) S2 T-LFT composite, and b) S3 T-LFT composite disclosing the fiber architecture, fiber alignment, and dispersion of fibers within the CFRTP tape and LFT.

visually. The concept behind this is to find a threshold value which maximizes the variance between the clustered phases. Figure 3.7 (a) shows the grayscale intensity histogram with thresholding values, and it is used to distinguish the characteristic phases of the raw grayscale volume of T-LFT composite samples (Figure 3.7 b). The applied threshold range of 0 to 0.23 represents the pores, 0.23 to 0.64 as a matrix, 0.64 to 1.95 as fibers, 1.95 and above represents surface impurities and artifacts. A binary volume with applied thresholding (Red = Pores, Green = PP matrix, Dark brown = Glass fibers) shown in Figure 3.7 (c).

Figure 3.8 (a, b) shows the 2D cross-section slices of S2 and S3 T-LFT samples. Figure 3.8 (a, b) provides evidence of optimal manufacturing. There are no manufacturing defects and/or porosity at the interface, which confirms high interfacial bonding. The XCT results corroborate well with SEM microscopic results presented in previous SEM section. However, there are pores present in the LFT constituent, which is attributed to entrapped air during compression molding of LFTs. Once the PP-GF LFT extrudate placed over the tape assembly, the mold closes, and fiber-filled polymer flows except the area where it is placed. Hence air, water vapor, or other volatile gases get trapped within the extrudate. This creates internal voids within composite and referred as flow associated porosity. The CFRTP tape constituent shows very few pores present throughout all the layers.

The total volume percentage of the voids was calculated based on the image analysis of 2048 slices of the XCT scan volumes. S2 T-LFT sample has 0.30 % pores, and the S3 T-LFT sample has 0.69% pores, shown in Figure 3.9 (a, b) S2 and S3 T-LFT composite indicate scattered flow associated porosity.

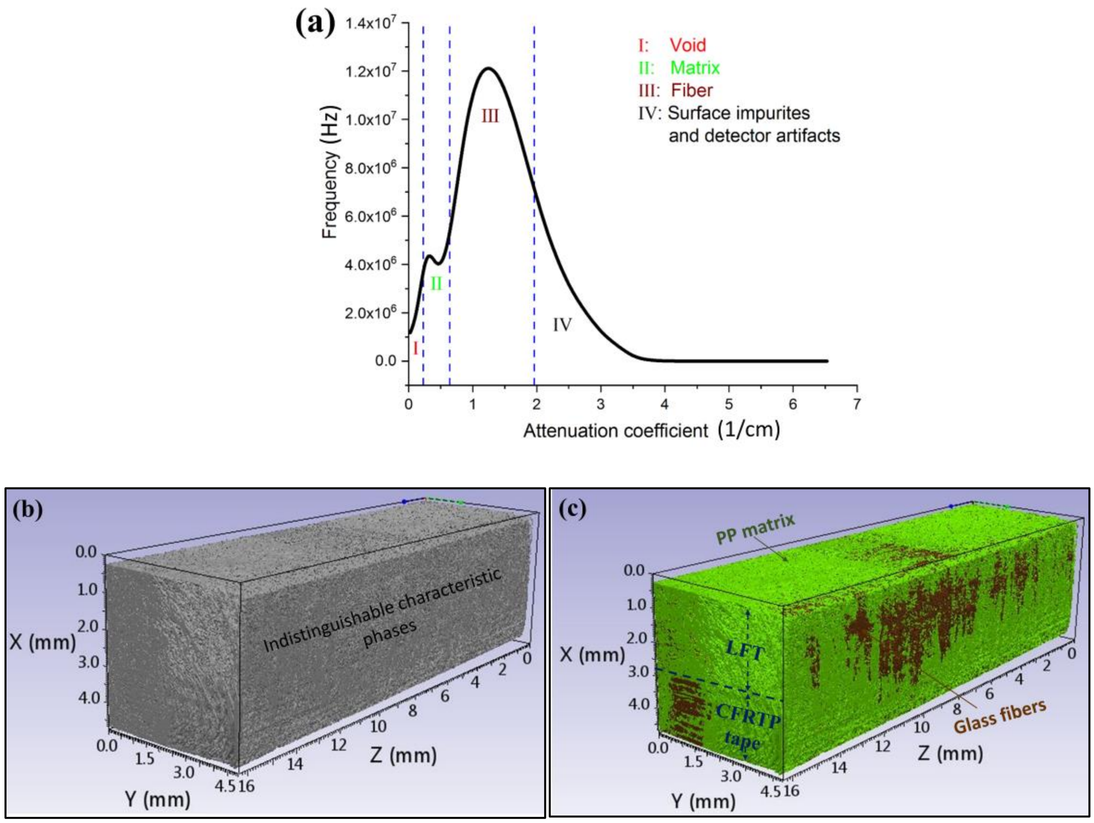

Figure 3.7: Histogram based image segmentation of 3D T-LFT composite; (a) grayscale intensity histogram with a threshold value, (b) raw grayscale volume, and (c) binary volume with applied thresholding range indicating characteristic phases of T-LFT composite.

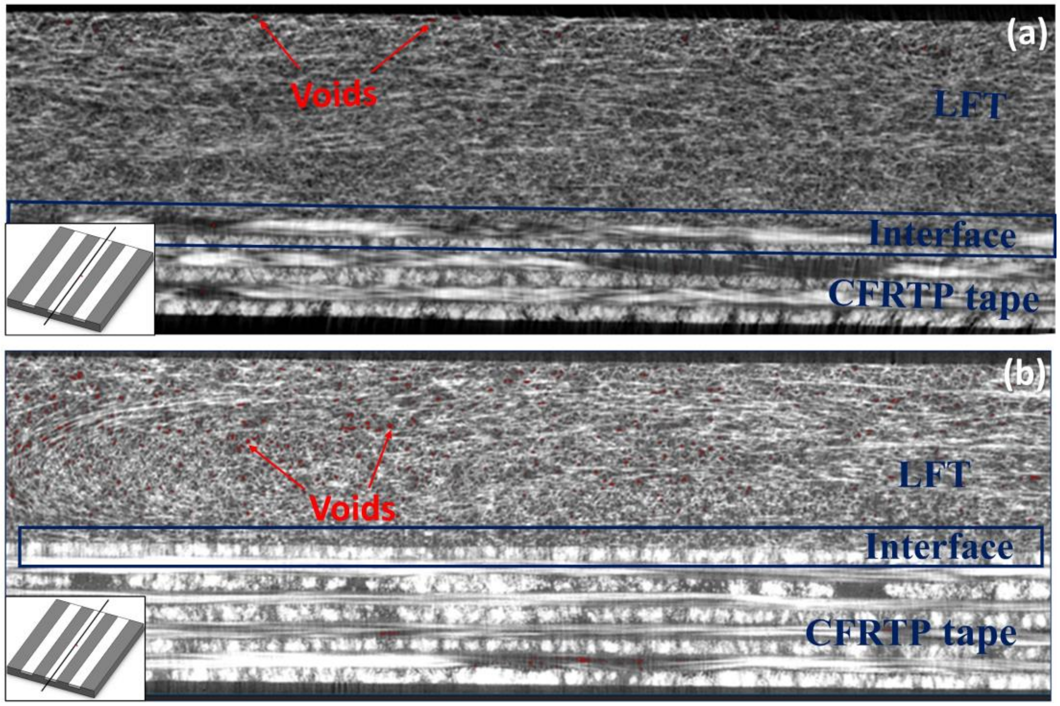

Figure 3.8: 2D crossectional slices of typical T-LFT composite indicating presence of pores primarily in LFT side and defect-free interface; a) S2, and b) S3 sample.

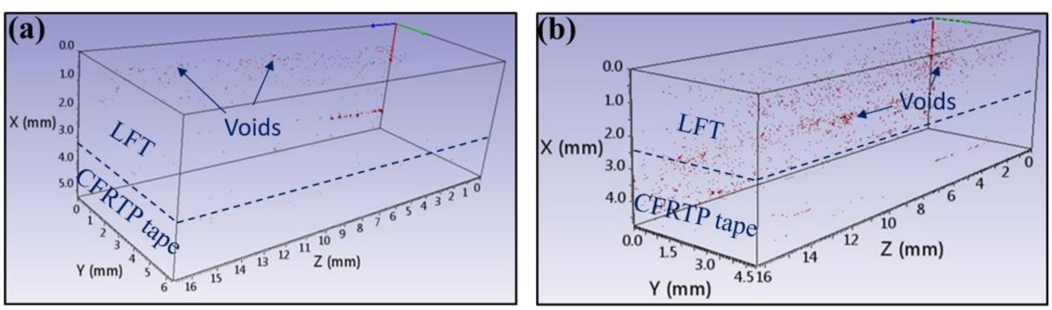

Figure 3.9: 3D binary volume showing size, shape, and location of pores in T-LFT composite; a) S2, and b) S3 sample.

3D images illustrate the size, shape, and location of pores in T-LFT composite. S2 and S3 T-LFT specimens show the heterogeneous distribution of pores. Most of the pores are present in the LFT side and are spherical in shape. There are average 32.50 E-06 mm^3 dimension pores present in T-LFT composite. In the S3 T-LFT sample, pores are mainly above the interface and present all over in LFT, whereas in S2 T-LFT samples, pores exist primarily nearby the surface of the LFT. It could be due to the time delay during manual transfer of each LFT charge from the plasticator to the mold while processing the T-LFT panels. The molten LFT charge tends to cool rapidly as it exits the chamber; thus, the slight time difference during each charge transfer will significantly affect the porosity location, size, and shape. The automated charge placing systems can address these manual errors. The automated controls will ensure the consistent reproduction of the T-LFT composite panel.

3.3.3 Mechanical and Microscopic Characterization

Mode 1 Interlaminar Fracture Toughness Testing

S2, and S3 T-LFT composite tested using the ASTM D5528-15 standard to evaluate respective G_{1c} values. An average G_{1c} value of 2.49 ± 0.02 N/mm for S2 T-LFT composite and an average G_{1c} value of 2.59 ± 0.13 N/mm for S3 T-LFT were noted. The G_{1c} values differ by 4% for both S2 and S3 T-LFT composite. In literature, the reported interlaminar fracture toughness value ranges from 220 J/m^2 (0.22 N/mm) to 2000 J/m^2 (2 N/mm) for PP-GF composite [40, 41]. On average, T-LFT composite shows a 27% higher G_{1c} value compared to literature, and it could be due to the various factors such as fiber orientation, fiber distribution, fiber wetting, molding conditions, adhesion, etc. The prior studies have shown that the molding conditions, adhesion, interdiffusion, and fiber bridging at the interface drives the fracture energy [32, 42]. However, the fracture energy is independent of the orientation of the fibers above and below the delaminating interface [43].

SEM micrographs (Figure 3.5 b, d) and XCT tomograms (Figure 3.6 a, b) of S2 and S3 T-LFT sample shows excellent adhesion between PP-GF LFT and PP-GF tape, very good fiber wet-out, and fiber distribution, respectively. XCT tomogram shown in Figure 3.8 (a, b) also reveals that they are not manufacturing defects and voids at the interface. The above factors could be the reason for the enhancement of G_{1c} in T-LFT composite. The study performed by Perrin et al. [40] complies well with the conclusion. They studied the effect of molding conditions and test temperature on Mode I interlaminar crack propagation in continuous PP-GF composites. Their study demonstrates excellent fiber distribution and good fiber wetting contribute to the high interlaminar fracture toughness. Thus, these all-collective pieces of evidence corroborate a strong bond between PP-GF LFT and PP-GF tape surfaces.

ILSS Testing

The average ILSS value of S3 T-LFT, S2 T-LFT and S1 LFT composites was 21.78 ± 0.35 MPa, 20.47 ± 0.42 MPa and 12.64 ± 0.80 MPa, respectively. The S1 LFT composite failed in tension before shear failure at the mid-plane takes place. Hence, in the S1 LFT composite, ILSS testing becomes invalid since fiber failed in tension before shear-induced failure occurs [3]. We believe tension failure occurred since S1 sample was composed of bulk LFT charge instead of laminas. The bulk LFT composite S1 does not contain any layer throughout the thickness. Therefore, for ILSS comparison purpose, LFT composite sample manufactured and tested with two layers of LFT. Each LFT layer thickness maintained to 1.80 mm and total thickness of LFT composite retained to 3.60 mm.

The average ILSS value increased by 41% for S3 T-LFT composite (21.78 ± 0.35 MPa) compared to LFT composite (15.42 ± 3.02 MPa). Similarly, for S2 T-LFT composite ILSS value (20.47 ± 0.42 MPa), enhanced by 33% compared to LFT composite.

According to the literature [4, 44, 45], ILSS value mainly depends on fiber-matrix interfacial shear strength and matrix characteristics rather than the fiber attribute. The ILSS value decreases linearly with an increase in void content, fabrication defects, dry strands, and internal microcracks. XCT tomogram shown in Figure 3.8 (a, b) revealed that there are no manufacturing defects or voids at the interface of S2 and S3 T-LFT composite. XCT tomograms also revealed that pores are present in LFT and attributed to entrapped air during the manufacturing process. Thus, in S2 and S3 T-LFT composites, excellent interfacial bonding between LFT and tape could be the primary reason for 33 and 41% higher ILSS value compared to LFT composite, respectively. Likewise, high void content in LFT composite could be the reason for lower ILSS value (27% on an average lower compared to T-LFT composite). The fractured surfaces of the tested S2 and S3 samples were inspected using SEM, Figure 3.10. The S2 and S3 T-LFT composite samples failed by interlaminar shear cracking and fiber rupture. The crack initiated at the LFT- tape interface and then transferred into the LFT part due to the fiber breakage. Interlaminar shear failure is the governing mode of failure in both S2 and S3 T-LFT composite.

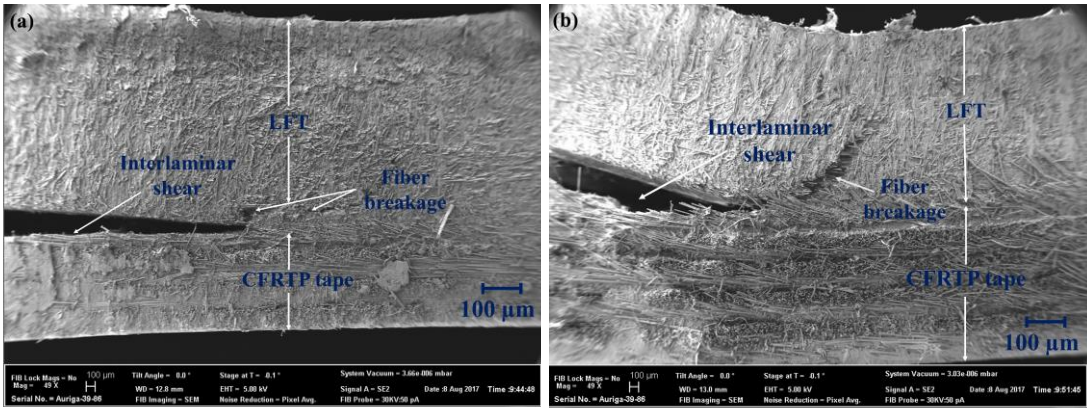

Figure 3.10: SEM micrographs of fractured ILSS sample shows interlaminar shear cracking and fiber rupture at LFT-tape interface; a) S2 T-LFT, and (b) S3 T-LFT.

Flexural Testing

To estimate the effect of PP-GF continuous fiber tape on PP-GF LFT, we performed the three-point flexural test. Figure 3.11 (a) shows the load-displacement curves of S1 LFT composite (baseline), S2, and S3 T- LFT composites. S2 and S3 T-LFT composites showed non-linear behavior due to the plastic deformation of CFRTP tape cross-plies. S1 LFT composite failed in brittle fashion at the lower end on load-displacement diagram; however, S2 and S3 T-LFT composites fractured in a progressive way at the higher end on load-displacement diagram. In S2 T-LFT composite, the first load drop appears around the equal displacement value at which S1 LFT composite failed, and it corresponds to the failure of the LFT constituent. After the first drop, the load increases back again, which corresponds to the load-bearing capacity of the tape component in T-LFT composite before the final failure. Whereas, S3 T-LFT composite does not display any load drop preceding the final failure. Hence, it indicates that the failure could be due to the debonding. Debonding failure usually takes place via areas of high stress concentrations. The path of debonding propagation depends on properties of a material (here it will be LFT substrate and tape) as well as interface and follows the path of least resistance [46]. In S3 T-LFT composite, the interface is highly stress concentrated and inadequate interfacial bonding between LFT and tape compared to strength of LFT and tape material. Therefore, we observed the failure occurred at the LFT-tape interface rather than in LFT and/or tape.

The energy absorption (area under the curve) of S2 and S3 T-LFT composites are higher compared to the S1 LFT composite. The T-LFT composites were better able to resist the damage under the bending load compared to LFT composite. The flexural properties of

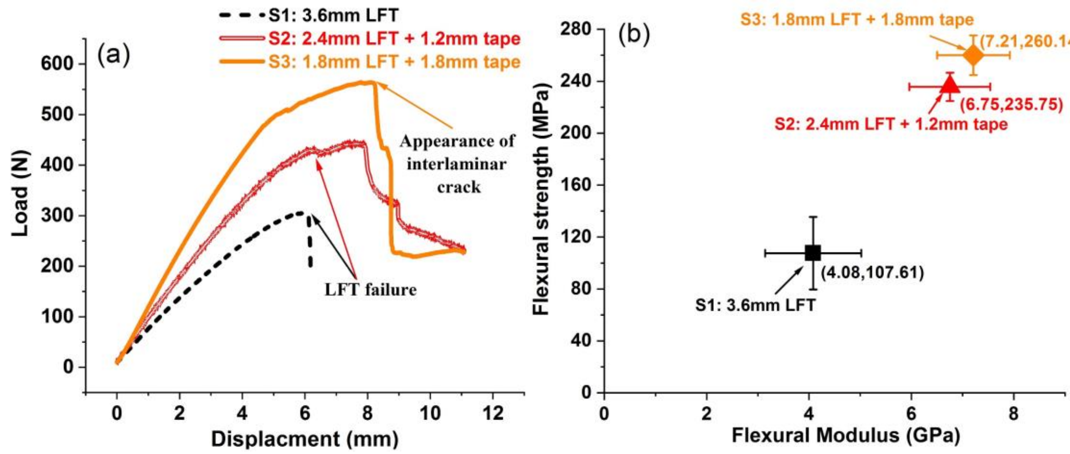

Figure 3.11: (a) Load versus displacement curves, and (b) flexural strength versus flexural modulus of baseline S1 and T-LFT composites S2 and S3

S2 and S3 T- LFT composites compared with S1 LFT composite, Figure 3.11 (b). Flexural strength and modulus increased by 142 and 77% respectively, for S3 T-LFT composite (260.14 ± 15.27 MPa, 7.21 ± 0.71 GPa) compared to LFT composite, S1 (107.61 ± 27.91 MPa, 4.08 ± 0.94 GPa). Similarly, for S2 T-LFT composite strength and modulus (235.75 ± 10.89 MPa, 6.75 ± 0.79 GPa), enhanced by 119 and 65% respectively, as compared with LFT composite S1. The bending results illustrate that the overmolding improves the failure resistance of LFT by 130% on an average.

A cross-ply tape laminate alone was tested for flexural properties. The average flexural strength and modulus were 360.45 ± 34.61 MPa and 17.25 ± 1.09 GPa respectively. Flexural results demonstrate the continuous fiber tape dominates the flexural properties of T-LFT composite.

The fractured specimens of S1, S2, and S3 composite were examined using SEM, as shown in Figure 3.12. Fiber fracture is the dominant failure mechanism in LFT composite S1, and it fails in a catastrophic manner leading to lower flexural stress (Figure 3.12 a, d); however, in S2 T-LFT composite (Figure 3.12 b, e) the crack initiates in the LFT (compression side) due to fiber breakage, and crack migrates into the continuous fiber tape laminate (tension side). In the tape, the crack can be seen only in the 90^0 plies, which indicates that the matrix fails before the continuous glass fibers. The intact LFT- tape interface enables the specimens to withstand higher loading. It leads to an increase in the flexural strength of T-LFT composite S2 compared to LFT composite S1 by 119%, see Figure 3.11 (b). The matrix failure within the tape on the tension side without delamination confirms, the complete utilization of tape strength.

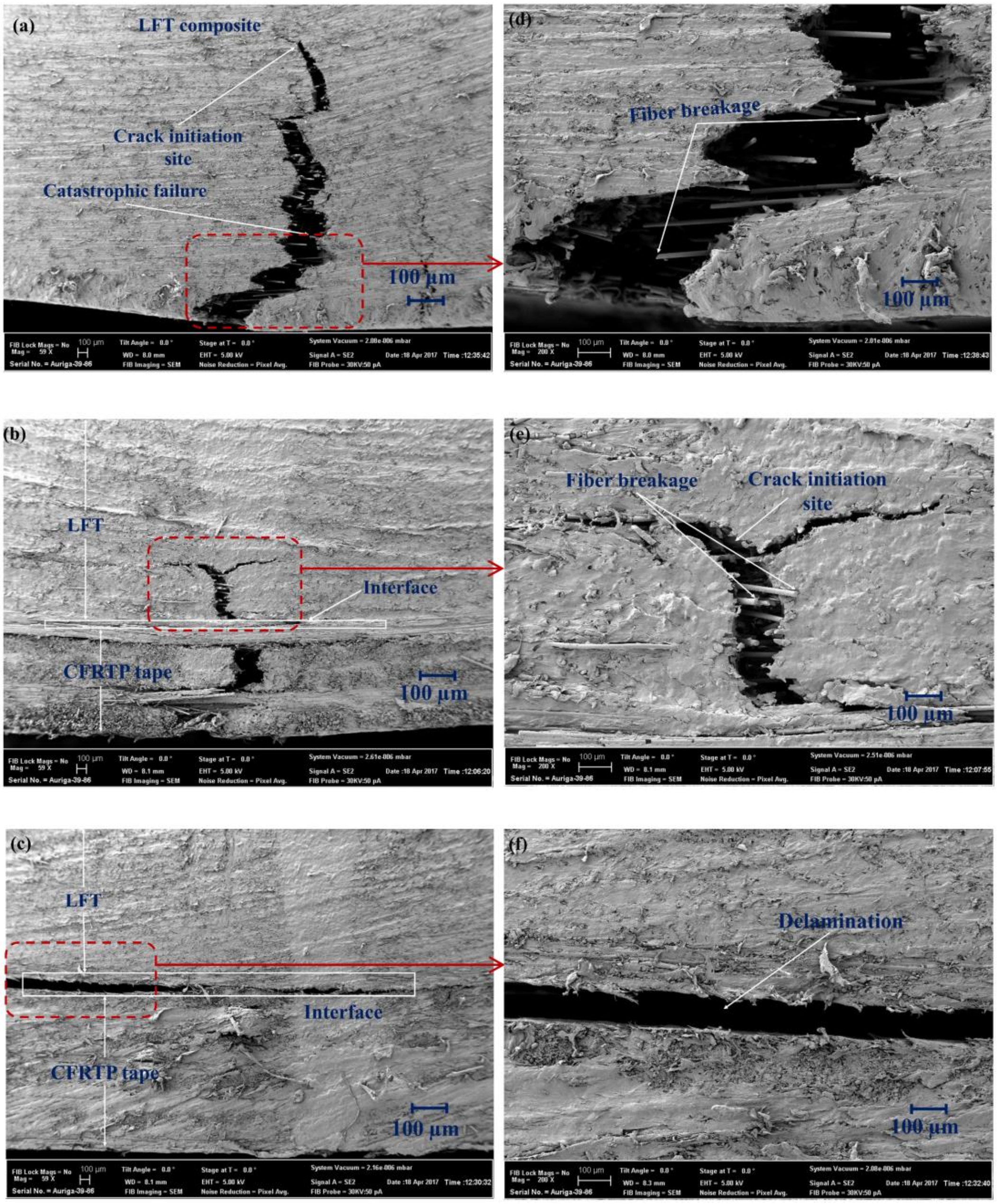

Figure 3.12: SEM micrographs of failed flexural coupons revealing failure mechanism of S1 (a, d) LFT composite, S2 (b, e), and S3 (c, f) T-LFT composites.

S3 T-LFT composite (Figure 3.12 c, f) exhibits interface delamination. The tape debonds from the LFT substrate. The tape and LFT both are 1.8 mm thick; thus, the neutral axis of the composite matches with the interface. Thereby, the interface is exposed to a high shear zone which leads to premature failure at the interface. There can be inferred that the tape strength is only partially utilized. Due to the moderate use of tape strength, insignificant improvement of flexural strength is observed in S3 compared with S2 T-LFT composite, see Figure 3.11 (b). Moreover, no cracks were observed in the LFT (compression side) as well as in the tape (tension side).

The above flexural results of the S2 and S3 T-LFT composite emphasizes that to employ the full strength of the tape component, the tape thickness must be less than 50% of the overall composite thickness.

LVI Testing

To evaluate the impact behavior of the LFT and T-LFT composites, LVI test was performed. The first impact tests were carried out for impact energy of 12 J (40 cm drop height). No penetration was observed for the LFT panel S1, as well as S2 and S3 T-LFT panels. Partial damage was noticed on the impact side of LFT panel S1.

The second impact test carried with an impact energy of 22 J (70 cm drop height) and full penetration was observed for of the LFT panel S1, whereas S2 and S3 T-LFT composite panels displayed moderate damage on the impact side. No penetration was observed for both T-LFT composite panels.

When the impact energy increased to 37 J (drop height of 120 cm), LFT and T-LFT composite panels perforated. The amount of energy absorbed by LFT composite S1 and T-LFT composite S2 and S3 found to be 7.76, 30.15, and 27.66 J, respectively. The results illustrate that the overmolding technique enhances the energy absorption capacity of LFT by 272% on an average.

Figure 3.13 compares the load versus time data obtained for a 120 cm drop height. At maximum load, S2 and S3 T-LFT composite panels deflected 41 and 28% more when compared to S1 LFT composite. The deformation of the T-LFT composite panels leads to energy absorption. It can be observed that the S2 T-LFT configuration exhibited the maximum load with the highest energy absorption. The ability to store energy elastically in the fiber is dictated by the fiber failure strain. Thus, higher the strain to failure of the fiber, greater the energy absorption capabilities of the fiber reinforced composite [47]. The fiber failure strain of S1 LFT, S2 T-LFT and S3 T-LFT composite was 1.10, 1.95 and 1.68, respectively. S2 T-LFT composite displayed 16 and 77% higher fiber failure strain compared to S3 T-LFT and S1 LFT, respectively. The failure strain data corroborates well with energy absorption results. Table 3.4 summarizes the LVI results.

3.3.4 Computational Analysis

Flexural test was analyzed computationally using a micromechanics approach and finite element simulations. The micromechanics approach was used to construct the anisotropic stiffness tensor based on experimental tests, and the stiffness tensors for the two composite materials (i.e., LFT composite and CFRTP tape) were used for the finite

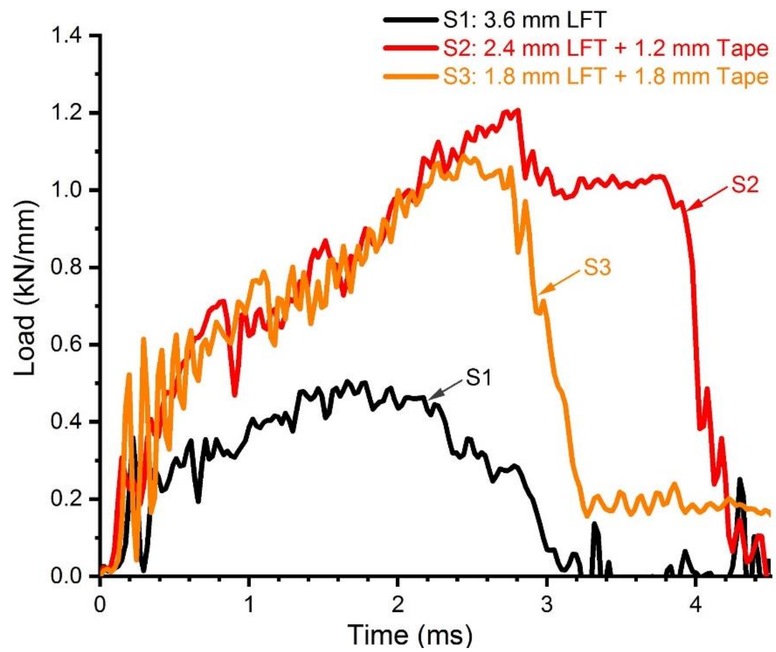

Figure 3.13: Comparison of load vs. time for impact energy of 37 J indicating high energy absorption in T-LFT composite compared to LFT composite.

Table 3.4: LVI properties at a drop height of 120 cm and impact energy of 37J.

Sample	Height (cm)	Impact Energy (J)	Velocity (m/s)	Max Load (kN/mm)	Energy Max Load (J)	Deflection at max load (mm)
S1	120	36.77	4.79	0.51	7.76	7.55
S2	120	37.73	4.73	1.21	30.15	10.61
S3	120	38.38	4.77	1.09	27.66	9.63

element simulations with the three configurations as described in Table 3.1: (1) 3.6 mm LFT / 0 mm Tape, (2) 2.4 mm LFT / 1.2 mm Tape, (3) 1.8 mm LFT / 1.8 mm Tape.

To construct the stiffness tensor, Young's moduli of composites in x and y directions were experimentally obtained. For LFT, the extruded charge is an elliptical shape, and the major axis of the charge was defined as the transverse direction (y direction). The minor axis of the charge (flow direction) was defined as the longitudinal direction (x direction). For unidirectional continuous fiber composites, the x direction was defined as the fiber direction and the y direction was defined as perpendicular to the fiber direction. Since our CFRTP tape consisted of [0°/90°] cross plies with the equal amount of 0° layers and 90° layers, any one of 0° and 90° is x direction, and the other is y direction.

For computational purpose additional 1.2 mm thick unidirectional CFRTP tape laminate manufactured using same processing conditions as described in section in 3.2.1, materials and methods. Tensile test coupons were extracted in x and y direction from LFT composite and unidirectional CFRTP tape laminate. Samples were tested at 2 mm min^{-1} loading rate at room temperature according to the ASTM D3039 standard. Strain was measured using extensometer. Table 3.5 and 3.6 shows the experimental young's modulus for the LFT composite and the unidirectional CFRTP tape laminate, respectively. The first half of each table shows the longitudinal properties, and the second half of the table shows the transverse properties. Stiffnesses of individual materials (i.e., glass fiber and polypropylene) were calculated based on the tensile tests of unidirectional CFRTP in the fiber direction and the transverse direction using Voigt and Reuss average schemes (i.e., isostrain and isostress).

Table 3.5: Experimental Young's modulus of LFT sample in longitudinal and transverse direction.

	longitudinal Young's modulus (charge flow direction)			Transverse Young's modulus (Cross to charge flow direction)		
Samples	Modulus (GPa)	Avg. Modulus (GPa)	Std. Deviation	Modulus (GPa)	Avg. Modulus (GPa)	Std. Deviation
LFT1	5.63	4.96	0.95	3.73	3.64	0.14
LFT2	5.84			3.45		
LFT3	3.80			3.63		
LFT4	4.59			3.76		

Table 3.6: Experimental Young's modulus of unidirectional CFRTP tape sample.

	longitudinal Young's modulus			Transverse Young's modulus		
Samples	Modulus (GPa)	Avg. Modulus (GPa)	Std. Deviation	Modulus (GPa)	Avg. Modulus (GPa)	Std. Deviation
Tape1	21.14	20.75	0.26	2.15	2.20	0.11
Tape2	20.70			2.26		
Tape3	20.40			2.04		
Tape4	20.74			2.33		

Table 3.7 shows the individual properties of GF and PP. Micromechanics-based material modeling was used to calculate the stiffness tensor of fiber reinforced polymer composites. Since composite materials have non-uniform fiber orientations, a paper physics-based approach [48, 49] was implemented to reverse engineer orientation of fiber as shown in Figure 3.14. This procedure utilized a de-homogenization technique [50] involving finding the distribution of fiber orientation that satisfies the longitudinal and transverse stiffness from experiments. The details of the approach are shown in reference [51].

Commercial software, MCQ-Chopped by AlphaSTAR Corp., was used for this approach. First, the anisotropic stiffness tensor of a composite material with aligned fibers was obtained using the micromechanics approach. The composite material consists of the same composition as the LFT sample (PP with 40%wt. GF), but the fibers are assumed to be aligned in one direction. Table 3.8 shows the anisotropic moduli of the LFT composite with aligned fibers. Second, using the paper physics approach with reverse engineering, the fiber orientations (or layer orientations) were estimated to match the experimentally obtained moduli in the flow direction (4.96 GPa) and the crossflow direction (3.64 GPa). This process is equivalent to finding an optimal laminate configuration consisting of multiple unidirectional plies with various thicknesses. Figure 3.15 shows the orientation angle distribution. Third, the anisotropic stiffness tensor was constructed using the fiber orientation data as in Figure 3.15. The moduli of the LFT composite material from the de-homogenization technique are listed in Table 3.9. It should be noted that the experimentally obtained E_{11} and E_{22} moduli (4.96 GPa and 3.64 GPa) are close to the reverse engineered

Table 3.7: Properties of individual materials (Glass fiber and neat polypropylene).

		GF	PP
Density	[g/cm^3]	2.55	0.92
Young's modulus, E	[GPa]	55	1.01
Poisson ratio, *v*		0.22	0.41

Table 3.8: Anisotropic moduli of composites (40% PP-GF) with an aligned fiber orientation.

Property	Value [GPa]	Property	Value [GPa]	Property	Value
E_{11}	11.207	G_{12}	0.521	NU_{12}	0.369
E_{22}	1.634	G_{13}	0.521	NU_{23}	0.634
E_{33}	1.634	G_{23}	0.500	NU_{13}	0.369

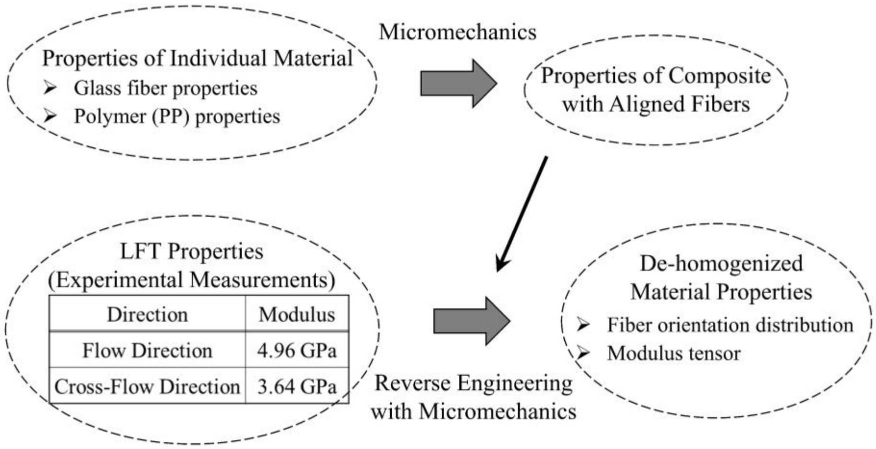

Figure 3.14: Flowchart of a reverse engineering with a de-homogenization technique for anisotropic material properties.

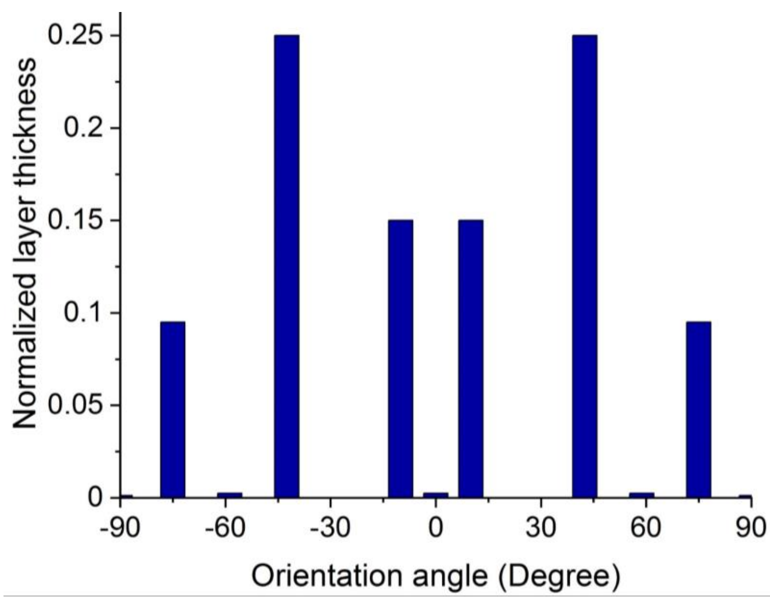

Figure 3.15: Fiber orientation angle distribution of the LFT composite. The normalized amount of fibers in any given orientation is equivalent to the normalized thickness of the unidirectional ply in the same direction.

E_{11} and E_{22} (4.94 GPa and 3.65 GPa).

With a similar approach, anisotropic moduli of a cross ply [0/90] CFRTP tape with 62% weight fraction of GF were calculated based on experimental longitudinal and transverse directional modulus of unidirectional CFFTP tape laminate as shown in Table 3.6. The values of the anisotropic moduli of the cross-ply tape are listed in Table 3.10. Flexural deformation of same three sample configurations (S1-LFT, S2, and S3 T-LFT composites) as shown in Table 3.1 analyzed computationally. The same flexural specimen dimensions as shown in Table 3.2 were used. The thicknesses of LFT and CFRTP vary depending on the samples. The first sample (S1) consists of 3.6 mm thick LFT and no tape. The second sample (S2) consists of 2.4 mm thick LFT and 1.2 mm thick CFRTP tape. The third sample (S3) consists of 1.8 mm thick LFT and 1.8 mm thick tape.

The simulation was configured based on the experiments described in section. 3.3.3 and it followed standardized test configurations as in ASTM D790. The overall configuration is shown in Figure 3.16. The simulation was performed with a commercial finite element package, Abaqus 2018.HF5. The sample in the simulation was discretized into 4600 brick elements with a quadratic interpolation function. The material properties were assigned to the elements with the 11-direction aligned along the longitudinal direction of the sample. The deformation was simulated using a linear elastic constitutive relation and it does not consider fracture or material failure. The properties used for LFT are listed in Table 3.9 and the properties used for CFRTP tape are listed in Table 3.10. The XCT characterization (section 3.3.2) demonstrated that there were no manufacturing defects and/or porosity at the interface.

Table 3.9: Anisotropic moduli of the compression molded (40% PP-GF) LFT composite.

Property	Value [GPa]	Property	Value [GPa]	Property	Value
E_{11}	4.944	G_{12}	1.948	NU_{12}	0.469
E_{22}	3.645	G_{13}	0.512	NU_{23}	0.425
E_{33}	2.216	G_{23}	0.509	NU_{13}	0.335

Table 3.10: Anisotropic moduli of the (62% PP-GF) CFRTP tape with a cross ply [0/90] layup

Property	Value [GPa]	Property	Value [GPa]	Property	Value
E_{11}	11.641	G_{12}	0.752	NU_{12}	0.065
E_{22}	11.641	G_{13}	0.727	NU_{23}	0.556
E_{33}	3.212	G_{23}	0.727	NU_{13}	0.556

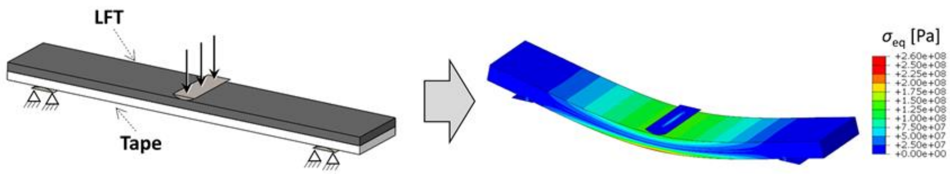

Figure 3.16: (Left) Simulation configuration for a flexural (3-point bend) test. (Right) Stress profile from the flexural test.

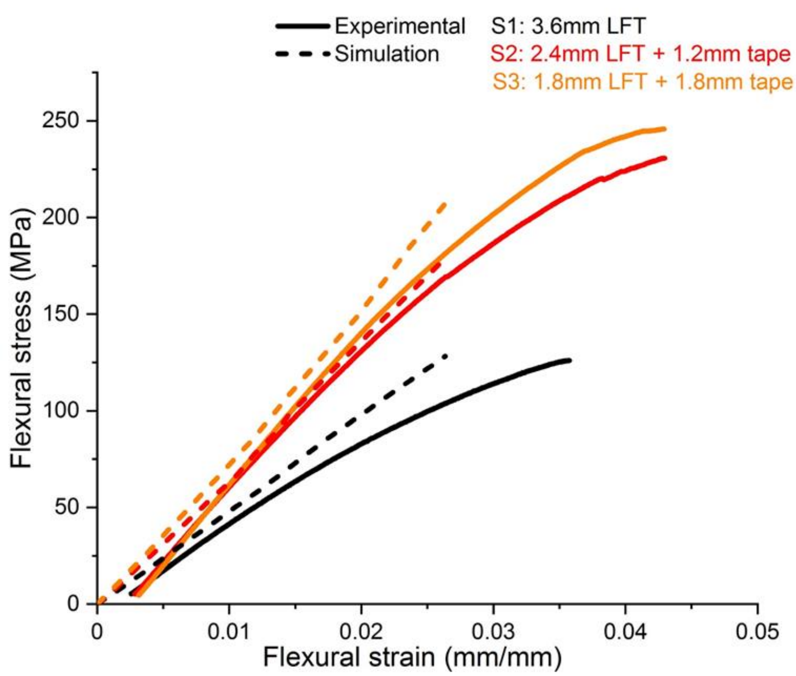

Figure 3.17: Comparison of stress-strain curves of the three samples (S1, S2, and S3) obtained from simulation and experimental testing.

Therefore, perfect bonding condition was applied at the interface of LFT and CFRTP tape. A contact condition between the sample and the load cell was applied. The contact condition includes a frictionless sliding for tangential movement and a pressure-overclosure relation for normal penetration, referred to as hard contact. The displacement of the load cell varied from 0 mm to 5 mm in vertical direction.

Figure 3.17 shows the simulated and experimental stress-strain relation for the three cases (S1, S2, and S3). Computationally, S3 T-LFT composite sample shows the highest modulus (7.63 GPa), which is 57% improvement as compared to the modulus of S1 LFT sample (4.87 GPa). S2 T-LFT composite sample shows the modulus of 6.74 GPa which is 38% improvement as compared to the modulus of S1 LFT sample. The simulated flexural modulus corroborates well with experimental flexural modulus (see section 3.3.3, Figure 3.11, b). Simulation results of flexural deformation showed that the simulation accurately represents the mechanical behavior of S1 LFT, S2 and S3 T-LFT composite. Therefore, the simulation models and the parameters in this study can be used for industry applications with complex geometries to analyze high stress areas and predict the performance improvement (stiffening effect) by adding CFRTP tapes.

3.4 Summary

In this study, processing and molding conditions governed by DSC and TGA used during the manufacturing of PP-GF T-LFT composite. SEM micrographs illustrated very good fiber wet-out and excellent interfacial bonding in T-LFT samples. The XCT revealed the fiber architecture, fiber alignment, and dispersion of fibers within T-LFT composite.

S2 and S3 T-LFT composite panels displayed perfectly aligned fibers in tape constituent and the excellent distribution of long glass fibers within the LFT constituent. The molding conditions strongly affected the shape, size, orientation, and location of voids in composite. The porosity level is below 1% in both T-LFT composites, which provide evidences of optimal manufacturing process for PP-GF T-LFT composite.

Mode I interlaminar fracture toughness G_{1c}, value for T-LFT composites are 25~30% higher compared to literature reported G1c value for PP-GF composite. We can conclude that the excellent fiber distribution, good fiber wetting, and absence of voids at the interface contributed to the high interlaminar fracture toughness value. ILSS testing revealed that T-LFT composites performed 33~41% higher compared to LFT composite and ILSS value primarily dependent on fiber-matrix interfacial shear strength and matrix characteristics rather than the fiber attribute. In T-LFT composites, interlaminar shear failure was a dominant failure mode. The three-point bend test disclosed that continuous fiber tape dominated the flexural properties of T-LFT composite. Fractured samples revealed that failure mechanism changes as tape thickness changes. Fiber breakage, matrix cracking, and interfacial debonding are the mainly observed failure modes in T-LFT composite. Flexural results highlighted that to utilize the strength of tape constituent completely; the tape thickness must be less than 50% of the overall composite thickness. Simulated flexural results accurately represents the mechanical behavior of LFT and T-LFT composite. Simulated results of flexural deformation correlates well with experimental results of S1 LFT, S2 and S3 T-LFT composites. LVI testing under dynamic loading conditions confirmed that T-LFT composite illustrated 28~41% higher deflection with increased load-bearing capabilities and leads to 288~256% high energy absorption compared to LFT composite. S2 T-LFT configuration exhibited the maximum load with the highest energy absorption.

Based on all summarized results, the innovative overmolding approach could be an effective alternative to the traditional manufacturing processes. The overmolded structures have the potential to provide more resistance against the imposed loads without a considerable increase in weight, superior crashworthiness, improved efficiency, and compelling cost element.

References

1. Ning Haibin, L.N., Hassen Ahmed Arabi, Chawla Krishan, Selim Mohamed & Pillay Selvum, A review of Long fibre-reinforced thermoplastic or long fibre thermoplastic (LFT) composites. International Materials Reviews, 2019.
2. Chawla Krishan, Composite materials. Springer, 2011: p. 151,152,153.
3. Chawla K.K., Materials science and materials engineering. 2016.
4. Mallick P.K., Materials, design and manufacturing for lightweight vechicles. Third ed. 2010, London, New York: Woodhead Publishing Limitied.
5. Hudson Leigh A., V.U.K., Dean Derrick R., Pillay Selvum, Shih Alan M., Design, analysis and development of optimized thermoplastic pultruded profiles. Thesis, 2009.
6. Bijsterbosch H., G.R.J., Polyamide 6—long glass fiber injection moldings. Polymer composites, 1995. 16 (5): p. 363-369.
7. Stokes V., I.L., Liang E., et al., A phenomenological study of the mechanical properties of long fiber filled injection-molded thermoplastic composites. polymer composites, 2000. 21 (5): p. 696-710.
8. Huang CT. et al., Investigation of Fiber Breakage Phenomena for Different Fiber Types in Injection Molding, in ANTEC® 2016 - Proceedings of the Technical Conference & Exhibition, Indianapolis, Indiana, USA May 23-25, 2016. 2016, Society of Plastics Engineers.
9. Andrea Sara, Analysis of fiber attrition and fiber-matrix separation during injeciton molding of long fiber reinforced thermoplastic parts. Master thesis, 2016.

10. Advani Suresh G, H.K.-T., Manufacturing techniques for polymer matrix composites (PMCs). Woodhead Publishing, 2012: p. 32,33.

11. Rosato Dominick V., R.D.V., V. Rasato Matthew, Plastic product material and process selection handbook. Elsevier science, 2004: p. 439-454.

12. Schemme Michael, LFT – development status and perspectives. Reinforced plastics, 2008. 52(1): p. 32-34, 36-39.

13. Gleich Klaus, L.K.C.A., Extrusion/Compression of long fiber thermoplastic composites Society of plastics engineers, 2001. 2: p. 145.

14. Yeole, P., et al., Characterization of textile-grade carbon fiber polypropylene composites. 0(0): p. 0967391120930109.

15. Mathijsen, D., Long fiber thermoplastics are a key technology in expanding existing markets for composites. Reinforced plastics, 2018.

16. Hufenbach W., B.R., et al., Polypropylene/glass fibre 3D-textile reinforced composites for automotive applications. Materials and Design, 2011. 32(3): p. 1468-1476.

17. Lee, H., et al., Compressive behavior of automotive side impact beam with continuous glass fiber reinforced thermoplastics incorporating long fiber thermoplastics ribs. 2017. 18(8): p. 1609-1613.

18. Vaidya, U., 6.2 Preforming, in Composites for Automotive, Truck and Mass Transit - Materials, Design, Manufacturing. 2011, DEStech Publications.

19. Adesina, O.T., et al., Mechanical evaluation of hybrid natural fibre–reinforced polymeric composites for automotive bumper beam: a review. 2019. 103(5): p. 1781-1797.

20. Vaidya, U., References, in Composites for Automotive, Truck and Mass Transit - Materials, Design, Manufacturing. 2011, DEStech Publications.

21. McConnell, V.P., SMC has plenty of road to run in automotive applications. Reinforced Plastics, 2007. 51(1): p. 20-25.

22. Brooks, R., 6.16 - Composites in Automotive Applications: Design, in Comprehensive Composite Materials, A. Kelly and C. Zweben, Editors. 2000, Pergamon: Oxford. p. 341-363.

23. Poor prospects for automotive SMC. Reinforced Plastics, 1992. 36(4): p. 10-10.

24. Moghaddam Mortazavi A.R., A.M.T., Design and analysis of an automobile bumper with the capacity of energy release using GMT materials. International Journal of Mechanical and Mechatronics Engineering, 2011. 5.

25. Beyene A.T., K.E.G., Belingardi .G., Martorana .B,, Design and manufacturing isssues in the development of lightweight solution for a vehicle frontal bumper. Procedia engineering, 2014. 88: p. 77-84.

26. N/A, New Developments in Long Fiber Reinforced Thermoplastic Composites (618), in ANTEC 2002 Plastics: Annual Technical Conference, Volume 2: Materials. Society of Plastics Engineers.

27. Miracle, D.B. and S.L. Donaldson, Advances in LFT, in ASM Handbook, Volume 21 - Composites. ASM International.

28. N/A, In - Line Compounding and Molding of Long - Fiber reinforced Thermoplastics (D - LFT) - Insight into a Rapid Growing Technology, in ANTEC 2004 Plastics: Annual Technical Conference, Volume 3: Special Areas. Society of Plastics Engineers.

29. Gan C., G., R. F., Newaz, G. M.,, Analytical/experimental investigation of energy absorption in grid-stiffened composite structures under transverse loading. 2004. 44(2): p. 185-194.

30. Jadhava P., M.P.R., Gibson R.F. , Energy absorption and damage evaluation of grid stiffened composite panels under transverse loading. Composites Part B, 2006. 37(2-3): p. 191-199.

31. Thattaiparthasarathy KB, P.S., Ning H, Vaidya UK, Process simulation, design and manufacturing of a long fiber thermoplastic composite for mass transit application. Composites: part A, 2008. 39: p. 1512-1521.

32. Vaidya, U., 5.3 Examples of Conventional LFT and Tailored LFT Parts, in Composites for Automotive, Truck and Mass Transit - Materials, Design, Manufacturing. 2011, DEStech Publications.

33. N/A, Added Value for Long - Fiber Reinforced Thermoplastic Components by In - Line - Compounding in the LFT - D - ILC Process, in ANTEC 2004 Plastics: Annual Technical Conference, Volume 3: Special Areas. Society of Plastics Engineers.

34. Brandrup, J., et al., Polymer handbook. Vol. 89. 1999: Wiley New York.

35. Krajenta, A.R.A., Physical state of the amorphous phase of polypropylene-influence on thermo-mechanical properties. Polymer, 2015. 70: p. 127-138.

36. Wang, Y., et al., Crystallization Behavior and Properties of Glass Fiber Reinforced Polypropylene Composites. Polymers (20734360), 2019. 11(7): p. 1198-1198.

37. Wilbers Arnold, B.A., Schillings Jennifer, Loosa Joachim, Application of iterative reconstruction algorithms to mitigate CT-artefacts when measuring fiber reinforced polymer materials. Polymer, 2019. 177: p. 120-130.

38. Garcea S.C., W.Y., Withers P.J. , X-ray computed tomography of polymer composites. Composite Science and Technology, 2018. 156: p. 305-319.

39. Ali M.A., U.R., Khan K.A., Cantwell W.J. , In-plane virtual permeability characterization of 3D woven fabrics using a hybrid experimental and numerical approach. Composite Science and Technology, 2019. 184.

40. Perrin F, B.M.N., Dickson J.I, Mode I interlaminar crack propagation in continuous glass fiber/polypropylene composites: temperature and molding condition dependence. Composites Science and Technology, 2003. 63(5): p. 597-607.

41. Jung, K.-H., et al., Finite element analysis of a low-velocity impact test for glass fiber-reinforced polypropylene composites considering mixed-mode interlaminar fracture toughness. Composite Structures, 2017. 160: p. 446-456.

42. Yeole, P., Fiber Metal Laminate with Thickness Reinforcement. 2015, The University of Alabama at Birmingham.

43. Chai, H., Bond Thickness Effect in AdJiesive Joints and Its Significance for Mode I Interlaminar Fracture of Composites. Composite Materials: Testing and Design

(Seventh Conference), ASTM STP 893, J. M. Whitney, Ed., American Society for Testing and Materials, 1986: p. 209-231.

44. Sridharan Srinivasan, Delamination behaviour of composites. Woodhead Publishing Limitied, 2008.

45. Yeole, P., H. Ning, and A.A. Hassen, Development and characterization of a polypropylene matrix composite and aluminum hybrid material. Journal of Thermoplastic Composite Materials, 2019: p. 0892705719843974.

46. Kang, T.H.K., et al., A State-of-the-Art Review on Debonding Failures of FRP Laminates Externally Adhered to Concrete. International Journal of Concrete Structures and Materials, 2012. 6(2): p. 123-134.

47. Richardson, M.O.W. and M.J. Wisheart, Review of low-velocity impact properties of composite materials. Composites Part A: Applied Science and Manufacturing, 1996. 27(12): p. 1123-1131.

48. Fukuda, H., K.J.F.s. Kawata, and technology, On Young's modulus of short fibre composites. 1974. 7(3): p. 207-222.

49. Jayaraman, K. and M.T. Kortschot, Correction to the Fukuda-Kawata Young's modulus theory and the Fukuda-Chou strength theory for short fibre-reinforced composite materials. Journal of Materials Science, 1996. 31(8): p. 2059-2064.

50. Godines, C., et al., Damage tolerant composite design principles for aircraft components under static service loading using multi-scale progressive failure analysis. 2017. 51(10): p. 1393-1419.

51. Analysis on Part Distortion and Residual Stress in Big Area Additive Manufacturing with Carbon Fiber-Reinforced Thermoplastic using Dehomogenization Technique, in Proceedings of Composites and Advanced Materials Expo (CAMX). 2019: Anaheim, California, United States of America.

4. CHAPTER 4

HIGH PERFORMANCE CARBON -NYLON SANDWICH COMPOSITE MOLDED USING LONG FIBER THERMOPLASTIC AS CORE AND CONTINUOUS COMMINLGED FIBERS AS SKIN VIA OVERMOLDING PROCESS

Abstract

Sandwich structures are extensively used in aerospace, marine, transportation other applications. Most of the sandwich constructions comprise fiber reinforced skins and core made from aluminum / Nomex (aramid) honeycomb, or foams. Overmolding of continuous with discontinuous fiber reinforcement provide avenues for innovation, design freedom and ability to tailor stiffness, strength, and damage tolerance for a broad range of structural applications. This work considered discontinuous long fiber thermoplastic (LFT) core overmolded with continuous carbon fiber reinforcement to produce sandwich composites. The skins comprised unidirectional and triaxial (0°/±60°) braided commingled fibers. The overmolded sandwich composite samples were characterized using spectroscopic and microscopic techniques to evaluate interfacial bonding of the skin - LFT core. Vibration analysis of overmolded sandwich composites was conducted to determine the damping and frequency. The coefficient of linear thermal expansion of commingled fiber overmolded LFT sandwich composites determined by thermomechanical analysis was in the range of 2.18~7.06 μm/m°C. Unidirectional and braided fiber overmolded LFT sandwich composites exhibited higher flexural strength (130%~81%), flexural modulus (192%~94%), tensile strength (169%~125%), and tensile modulus (118%~49%) compared to constituent LFT composite, respectively. Finite element analysis (FEA) using ABAQUS was used to validate the sandwich concept in a remote control (RC) airplane wing application. The unidirectional-LFT wing demonstrated 8% higher specific stiffness than braided-LFT wing structure.

Keywords: Sandwich composites, Commingled fiber, Filament winding, Finite element analysis, Vibrational testing.

4.1 Introduction

The use of polymer matrix composites (PMCs) reinforced with carbon fiber (CF) continues to increase rapidly in aerospace, ships, automotive and infrastructure applications. PMCs provide high specific strength and stiffness, high impact resistance, superior fatigue resistance, and damage tolerance [1]. Sandwich composites [2] and grid stiffened PMCs [3] are preferred in stiffness-critical structures due to their light weight and improved structural efficiency. The widespread use of foam core [2, 4], honeycomb core [5], and grid stiffened composites are extensively used [6, 7].

4.1.1 Literature Review

Foam and honeycomb-based sandwich composites and grid-stiffened composites have been studied extensively. Mohamed et al. [8] studied the influence of moisture absorption on the mechanical properties of glass polyurethane sandwich composites. They performed flexural and low velocity impact tests on distilled water immersed samples 15-day intervals and compared with dry samples. The flexural strength reduced by 35% compared to dry sample after 15 days, and after 30 days it further decreased by 17%. Zhou et al. [9] investigated the bending behavior of sandwich composite with Nomex honeycomb core. They identified that damage occurred through simultaneous core crush and top-skin delamination. Horrigan et al. [10] conducted theoretical and experimental investigations on glass epoxy Nomex honeycomb core sandwich composites. They showed that a soft, compliant projectile causes shallow crushing of the core whereas hard projectile developed concentrated damage that follows the shape of projectile. Hence it can be deemed that enhancing the damage tolerance of sandwich structures is desirable.

Shroff et al. [11] investigated grid stiffened panels to evaluate effect of typical 100-150 passenger aircraft fuselage loads. Their study demonstrated that at high compression load levels, grid-stiffened composite exhibits skin delamination resulting sudden loss of stiffness. Rahimi et al. [12] studied the effect of stiffener profile on the buckling strength of isogrid stiffened composite cylindrical shell under axial loading. Their study demonstrates that stiffening the shells increased the buckling load in range of 10%~36%. However, the specific buckling load decreased to 42%~52% of an unstiffened shell. Kamareh et al. [7] presented a comparative study on the debonding of skin and the lattice stiffener. Their findings clearly illustrate that debonding between the skin and ribs adversely influences the bending behavior of the composite. Ahmadi et al. [13] investigated the behavior of grid stiffened composite panel subjected to transverse loading. They found that debonding between skin and ribs is the dominant failure mechanism during transverse loading.

Lamanna et al. [14] studied the aluminum filled syntactic foam core sandwich composites for vibration response. They reported that damping ratio was between 0.46%~0.52% which is more than twice the damping ratio of metal matrix composite and glass filled epoxy composite [15].

From the various studies it can be seen there are several critical needs such as high bond strength between the skin and core/stiffener to eliminate delamination, enhanced damage tolerance without considerable increase in weight, and compelling cost basis.

This study presents an approach to produce sandwich composites utilizing discontinuous-continuous fibers via innovative overmolding approach. Discontinuous long fiber thermoplastics (LFTs) comprise the core and continuous commingled fibers comprise the skin(s). LFT offers light weight, balanced mechanical properties, excellent impact resistance, vibration damping and infinite shelf life [16]. The commingled fibers provide higher potential for advanced mechanical performance, homogenous distribution of reinforcement and matrix over the yarn cross section, and ease of molding and processing [17], [18]. The innovative overmolding approach features LFT and continuous commingled constituents and provides numerous advantages such as enhanced damage tolerance, superior crashworthiness in conjunction with reduced weight and recyclability [17-19].

Discontinuous LFTs were processed via extrusion compression molding (ECM) as core. Continuous fiber reinforcement-i.e., unidirectional and triaxial (0°/±60°) braided commingled fibers skins were used to overmold the LFT. Differential scanning calorimeter (DSC), thermo-gravimetric analysis (TGA) was performed to determine the thermal properties. Thermomechanical analysis (TMA) was performed to evaluate dimension stability of the sandwich composites and hence its suitability for high temperature application. Spectroscopic and microscopic investigations have been carried out on both unidirectional and braided skin LFT core sandwich composites. Vibration analysis was performed to determine the damping characteristics of these sandwich composites. Mechanical characterization included - flexural (4-point bend) and tensile tests. As an application of sandwich composites, a remote control (RC) plane wing of approximate dimensions 1350 mm x 207.6 mm x 1.213 mm was designed and analyzed computationally.

4.2 Experimental

4.2.1 Materials and Processing

Carbon fiber (CF) reinforced polyamide (PA)-6 resin (Celstran® PA6-CF) LFT pellets of 11 mm (0.43 in.) fiber length, and 40 wt % CF were obtained from Celanese Corporation, Florence, KY, USA. The continuous unidirectional and triaxial (0°/±60°) braided PA6-CF commingled fibers with 59 wt % CF were acquired from Concordia Fibers, Rhode Island, USA. LFT pellets in conjunction with unidirectional and triaxial braided commingled fibers were dried at 80^{o}C for 16 hours prior the processing to avoid moisture absorption.

For characterization purpose, two sample configurations were fabricated− (I) Unidirectional commingled fiber overmolded LFT sandwich composite, and (II) Triaxial (0°/±60°) commingled fiber overbraided LFT sandwich composite.

Overmolded sandwich test coupons were processed and prepared in two stages. The first stage involved the fabrication of LFT core via ECM. ECM utilizes a single screw, low shear extruder (Impco B20 extrusion plasticator), and 100-ton hydraulic compression press

(Beckwood Corporation, Fenton, Missouri, USA). To prepare hot, molten charge, the plasticator has four heating zones which were set and maintained above the melting point of PA6, i.e., 249°C, 260°C, 270°C, and 270°C, respectively. PA6-CF LFT pellets were fed into a heated barrel where the CF are uniformly dispersed into a molten PA6 polymer, and then extruded molten ~655 grams LFT charge of size 279.4 mm (11 in.) length 50.8 mm (2 in.) diameter from the heated barrel. The extruded charge was immediately transferred into pre-heated (135°C) flat mold 279.4 x 279.4 mm (11 × 11 in.) mounted in Beckwood hydraulic press. To let the charge flow and fill the mold cavity uniformly, pressure of 6.27 MPa (909 psi) was applied. Prior to demolding, the LFT material was dwelled for 5 mins (longer than usual to avoid warpage). On an average, 279.4 × 279.4 × 6.4 mm (11 × 11 × 0.25 in.) LFT composite core was fabricated.

The second stage involves the over wrapping of LFT core with commingled fibers and further consolidate hence resulting in an overmolded sandwich panel. The overmolded sandwich composite was produced utilizing 30-ton compression press (Model # 3895.4NE1000, Carver, Inc. USA). Overall skin to core ratio was expected to be 1:12 across all the manufactured samples.

Unidirectional commingled fiber overmolded LFT sandwich composite

The unidirectional commingled fiber tow winded unidirectionally over extrusion-compression molded LFT core utilizing filament winder equipment (Entec Model 5K30-180-4-1, Engineering Technology Corporation, UT, USA). The tensioning unit provided 13.56 N-m (10 ft-lbf) on the spool to allow adequate tension on the commingled fiber tows while being wound on the LFT core (acting as a mandrel) (see Figure 4.1, a). The filament winding setup had one layer of commingled fiber wound for a width of 228.6 mm (9 in.) along the LFT mandrel as shown in Figure 4.1 (b). After winding was complete, the overall assembly (commingled fiber skin – LFT core) was consolidated to form the overmolded sandwich panel (see Figure 4.1, c) by dwelling for 45 mins under heat (240oC) and pressure (0.63 MPa) using a Carver (Model # 3895.4NE1000, Carver, Inc. USA) compression press.

Triaxial (0°/±60°) braided commingled fiber overmolded LFT sandwich composite

The 279.4 mm (11 in.) wide and 279.4 mm (11 in.) long triaxial (0°/±60°) braided commingled fabric wrapped over extrusion-compression molded LFT core (Figure 4.2, a) by maintaining 10 N-m (7.376 ft-lbf) tension. To avoid wrinkling of the commingled braided fabric, it was spot fused with LFT core at multiple locations using a soldering iron prior to consolidation into an overbraided LFT sandwich panel (same processing conditions as for unidirectional overmolded LFT composite were employed) (Figure 4.2, b). The Table 4.1 shows the nomenclature used to identify material systems in this research.

4.2.1 Thermal Analysis

DSC Q2000 (V24.11 Build 124) instrument (TA Instruments, New Castle, DE, USA) was used to evaluate the melting behavior of pellets, unidirectional fiber, and braided fiber. A heat/cool/heat procedure was performed.

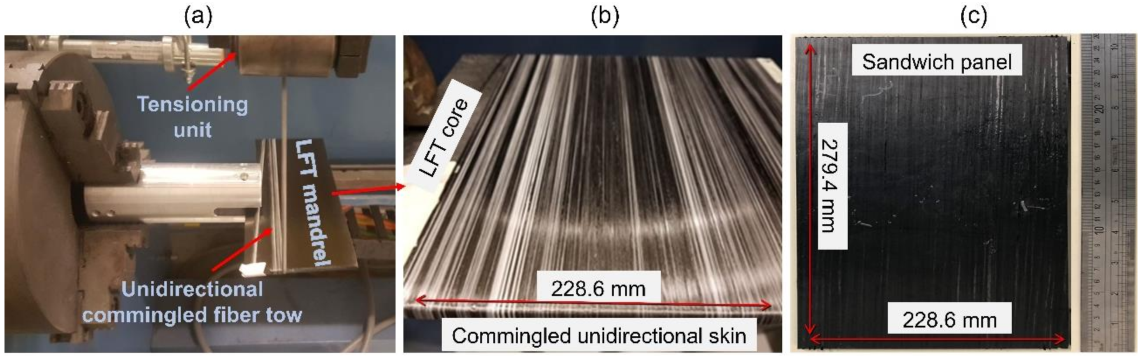

Figure 4.1: Processing steps of unidirectional commingled fiber overmolded LFT sandwich composite; (a) filament winding setup with a tensioning unit which provides 13.56 N-m tension on tows while being winded on LFT mandrel, (b) one layer of commingled fiber wound with a 2 mm step along 228.6 mm wide LFT mandrel, and (c) consolidated sandwich panel.

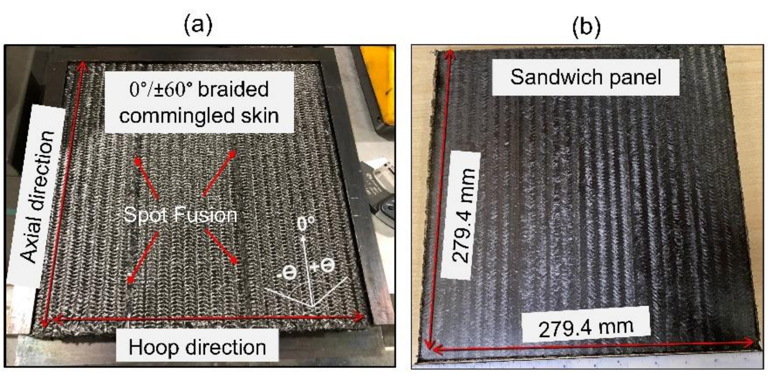

Figure 4.2: Processing steps of triaxial (0°/±60°) braided commingled fiber overmolded LFT sandwich composite; (a) Triaxial braided commingled fabric wrapped by maintaining 10 N-m tension and spot fused at multiple location to avoid wrinkling, and (b) consolidated sandwich panel.

Table 4.1: Nomenclature used to identify various material systems in this research.

Nomenclature	Material systems
Pellet	LFT pellet
LFT	LFT core
Unidirectional fiber	Unidirectional commingled fiber
Braided fiber	Triaxial (0°/±60°) braided commingled fabric
Unidirectional constituent	Unidirectional commingled laminate
Braided constituent	Triaxial (0°/±60°) braided commingled laminate
Unidirectional-LFT (U-LFT)	Unidirectional commingled fiber overmolded LFT sandwich composite
Braided-LFT (B-LFT)	Triaxial (0°/±60°) braided commingled fiber overmolded LFT sandwich composite

** From here onwards U-LFT and B-LFT will be used throughout the chapter instead of unidirectional-LFT and braided-LFT, respectively.*

The samples were heated from 25°C to 300°C at a rate of 10°C/min and isothermal step of 2 min at 300°C was performed to eliminate any thermal history that polymer may acquire during synthesis or post processing steps. The samples were then cooled to room temperature and reheated up to 300°C at a rate of 10°C/min to obtain the melting peak. The thermal stability and degradation behavior of pellets, unidirectional fiber, and braided fiber were studied using the Q50 TGA (V6.7 Build 203, TA instruments, New Castle, DE, USA). TGA measurements of the samples were carried out over a temperature range of 25-700^{o}C in an oxygen environment at a heating rate of 20 0C/min.

Dimension stability of LFT, U-LFT, and B-LFT under temperature variations were determined using TMA Q400 (V22.5 Build 31, TA instruments, New Castle, DE, USA). For this purpose, each sample (~8 mm in length) was placed in the furnace and compressive force of 0.02 N was applied using a rigid expansion probe. The temperature was ramped from room temperature (25^{o}C) to 180^{o}C in oxygen environment at a heating rate of 5^{o}C/min. All samples were tested in the axial direction.

4.2.2 X-Ray Photoelectron Spectroscopy (XPS)

Thermo scientific model K-Alpha XPS instrument (ORNL, Oak Ridge, TN, USA) having monochromatic AI Kα X-ray (1486.6 eV) source with a 128 multichannel electron energy detector operated at 2×10^{-9} mbar used to characterize surfaces of LFT, unidirectional constituent, braided constituent, U-LFT, and B-LFT. 4 mm × 4 mm sample was used with a depth penetration of 5-10nm. Dual-spot analysis was performed using a 400 µm-diameter X-ray spot size. Broad range of spectra (0-1350 eV) have been used for qualitative and quantitative analysis. Data was collected and analyzed using Thermo Scientific Advantage XPS software package (v 4.61) to understand interfacial bonding between commingled skin and LFT.

4.2.3 Optical Microscopy

Optical microscopy of the cross section of a U-LFT and B-LFT samples were performed to determine the skin to core ratio and interfacial morphology using high-resolution Keyence VHX 7000 (Keyence Corporation, IL, USA) optical digital microscope. Before imaging, samples were polished using MetaServ 250 (Buehler Inc., IL, USA) grinder-polisher in consecutive order of 180, 320, 600, and 1000 grits.

4.2.4 Vibration Testing

Bruel & Kjaer forced vibration setup (shown in Figure 4.3) with a 3160 LAN-XI module, 2735 power amplifier, 4810 mini-shaker, 8001 impedance head, and two 2647 CCLD converters was used to investigate resonant frequency and damping behavior of LFT, U-LFT, and B-LFT. A minimum of three 25.4 × 254 mm (1 × 10 in.) specimen each were tested for statistical relevance.

Each specimen was attached to the impedance head in double-cantilever position with a thin layer of bee’s wax to couple the sample to the impedance head [15, 20].

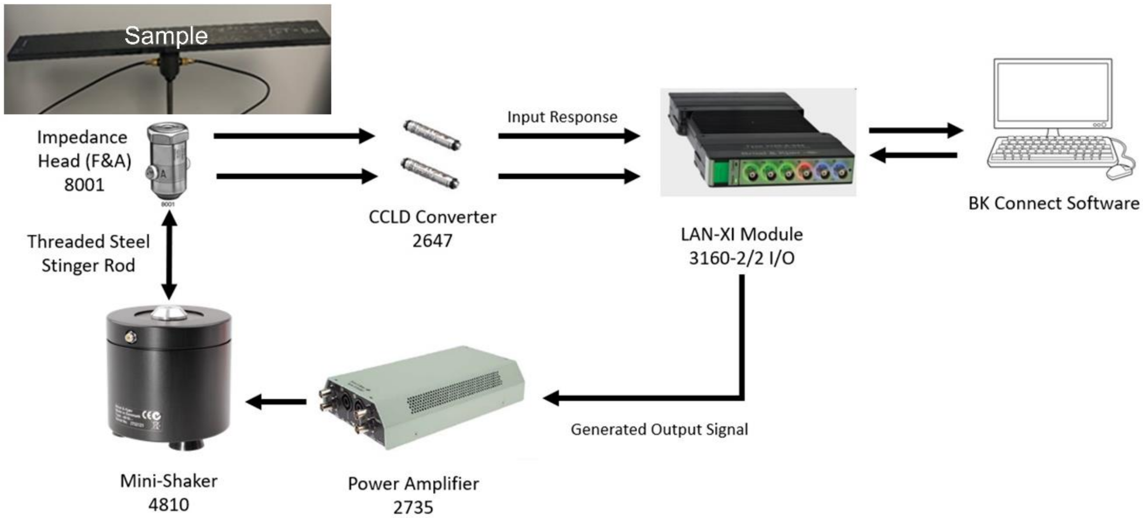

Figure 4.3: Bruel & Kjaer vibration setup with mini shaker and loaded sample

The signal generation and data capture were performed on the BK Connect 2018.1 software (Version 22.2.0.98, Bruel & Kjaer, GA, USA). A pseudo-random waveform was generated with a 6400 Hz low bandwidth at a 1 Hz resolution. The mini-shaker was excited to 100-mRMS amplification for sufficient excitation. Each sample went through 200 excitations with a total test time of 200 seconds and then averaged linearly to mitigate noise and outliers. The outcome is a frequency response form (FRF) which displays resonance frequency of the material. Only the first fundamental mode was used for analyzing the damping ratio. The half-power bandwidth method was used to calculate the damping ratio from the measured FRF in accelerance ($(m/s^2)/N$) [21-24].

4.2.5 Mechanical characterization

For mechanical (4-point bend, and tensile) testing, specimens were extracted using waterjet cutting. The specimens were taken from LFT (along charge flow induced fiber direction), U-LFT (longitudinal to fiber), and B-LFT (axial direction) panel. 4-point bend and tensile samples were prepared and tested according to the American Society for Testing and Materials (ASTM) standards [D6272-17, D3039-17], as summarized in Table 4.2.

Room temperature 4-point bend testing was performed in accordance with ASTM D6272-17 using a 50 KN Test Resources frame (product # 313Q, Test Resources, Minnesota, USA). LFT, U-LFT and B-LFT samples tested with a test rate of 2.95, 2.94, and 2.93 mm/min, respectively. Tensile testing was carried out according to ASTM D3039 standard at 2 mm/min loading rate using a 100 KN MTS frame (model # 647, MTS System Corporation, Eden Prairie, Minnesota, USA).

Table 4.2: Sample dimensions for mechanical testing as per ASTM standards.

No. of samples	Test	Samples	Average dimensions, mm		
			Length	Width	Thickness
4	4-point bend ASTM D6272-17	LFT	125.40	23.16	6.27
		U-LFT	125.02	23.89	6.29
		B-LFT	124.62	24.21	7.09
4	Tensile ASTM D3039-17	LFT	254.60	25.70	6.17
		U-LFT	254.40	25.23	6.19
		B-LFT	251.62	25.20	6.56

4.3 Results and Discussion

4.3.1 Thermal Analysis

Figure 4.4 (a) and 4.4 (b) represents the DSC and TGA results, respectively. DSC and TGA curves provide the melting, thermal stability, and degradation behavior of LFT pellets, unidirectional commingled, and triaxial (0°/±60°) braided commingled fiber. The melting temperature of the pellet, unidirectional fiber, and braided fiber were observed around 219.61^{o}C, 218.44^{o}C, and 219.90^{o}C respectively.

TGA curves exhibit the single-stage decomposition over the entire range of temperature. Less than 1% weight loss was observed when heated up to 341.39^{o}C, 364.82^{o}C, and 370.57^{o}C for pellet, unidirectional fiber, and braided fiber, respectively. This loss indicates the absence of moisture content, and thermal stability of the PA6 phase. A sudden mass drop was observed from ~408^{o}C to ~500^{o}C, due to the thermal degradation of the material. At 600^{o}C, the residual mass indicates the CF content in pellets (39.41 wt %), unidirectional fibers (71.25 wt %), and braided fibers (66.67 wt %) respectively. TGA data of pellets, unidirectional fiber, and braided fiber shows 1% lower, 21% higher, and 13% higher CF content compared to the company data sheet (section 4.2.1). DSC and TGA data helped to identify the lower (~220^{o}C) and upper (~341^{o}C) processing temperature limits for the overmolded sandwich composite.

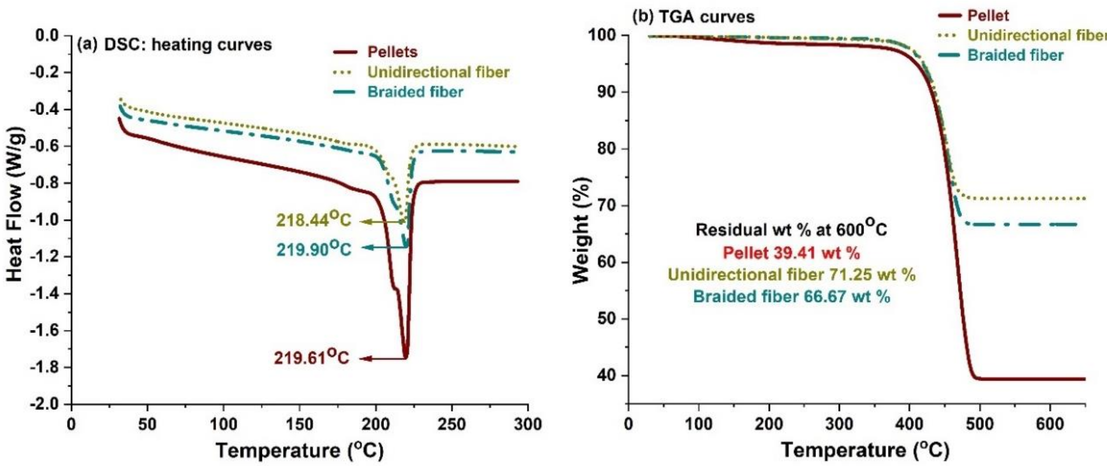

Figure 4.4: Thermal analysis results of pellet, unidirectional fiber, and braided fiber samples; (a) DSC heating curves with peak melting temperature, and (b) TGA curves showing single stage decomposition with residual wt % at 600^{o}C.

4.3.1 XPS Analysis

XPS analysis was conducted to evaluate the chemical composition of LFT, unidirectional constituent and braided constituent; as well as chemical reaction at the interface of U-LFT and B-LFT panel. XPS surface composition and overall spectra of LFT, unidirectional constituent and braided constituent are shown in Figure 4.5, respectively. All three specimens demonstrate high intensity peak at approximately 284 eV, 400 eV, and 532 eV binding energy representing high content of carbon, presence of nitrogen and oxygen, respectively. In overall spectra, other elements were also observed however their total composition was less than 2%.

High-resolution spectrums of carbon (C1s) and oxygen (O1s) were examined for each sample (LFT, unidirectional constituent, and braided constituent) to identify surface composition. It can be observed from Figure 4.6 (a) C1s spectrum consisted of several peaks such as C-C (284.6 eV), C-O (286.2 eV), and O=C-O (287.6 eV); however, O1s spectrum (Figure 4.6 b) indicated O=C (531.1 eV), O-C (532.72 eV) features. Overlapping curves of high-resolution spectra (Figure 6) for carbon and oxygen demonstrated slight variation between LFT and unidirectional/braided constituent. It could be due to difference in manufacturing (LFT manufactured via ECM, unidirectional constituent and braided constituent manufactured via compression molding).

Figure 4.7 and 4.8 shows high-resolution spectrums of C1s and O1s for unidirectional constituent with U-LFT interface, and braided constituent with B-LFT interface, respectively.

Surface Composition (at.%)

	C	O	N	Si	Ca	Na	S	Fe	Zn	Al
LFT	79.4	12.8	6.0	0.8	0.8	-	0.1	0.1	tr	-
Unidirectional Constituent	79.6	12.2	7.6	0.4	0.1	0.1	0.1	-	tr	-
Braided Constituent	74.3	15.7	8.1	0.7	0.2	0.1	0.1	0.5	0.1	0.2

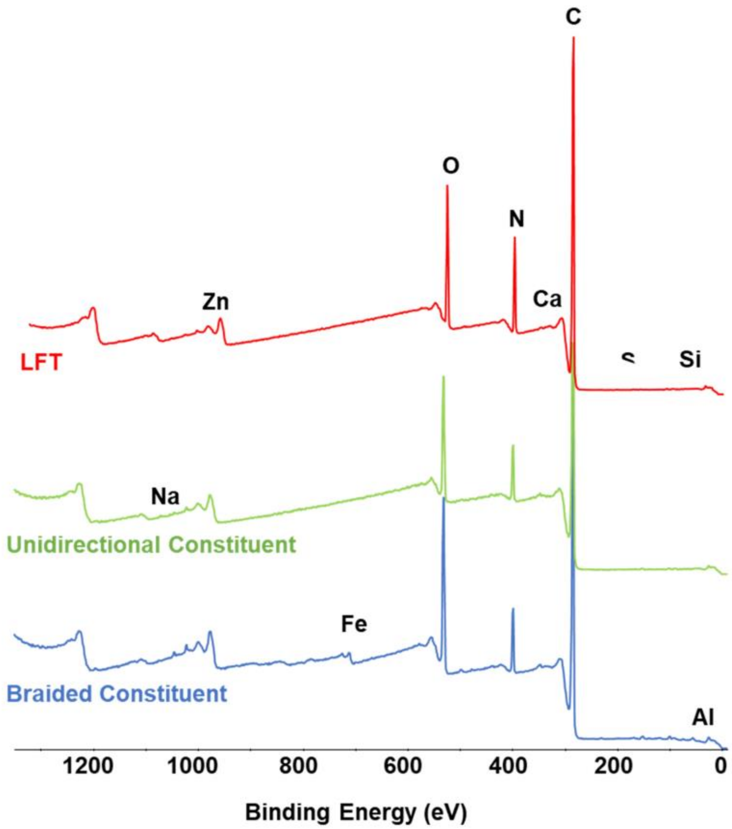

Figure 4.5: Surface atomic composition with XPS overall spectra of LFT, unidirectional constituent, and braided constituent

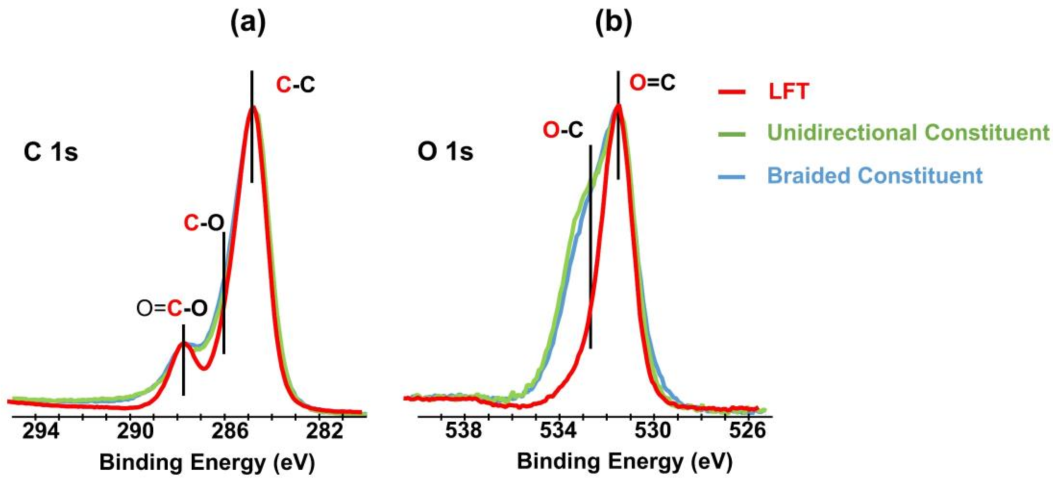

Figure 4.6: XPS high-resolution spectra of (a) C1s and (b) O1s peaks for LFT, unidirectional constituent and braided constituent

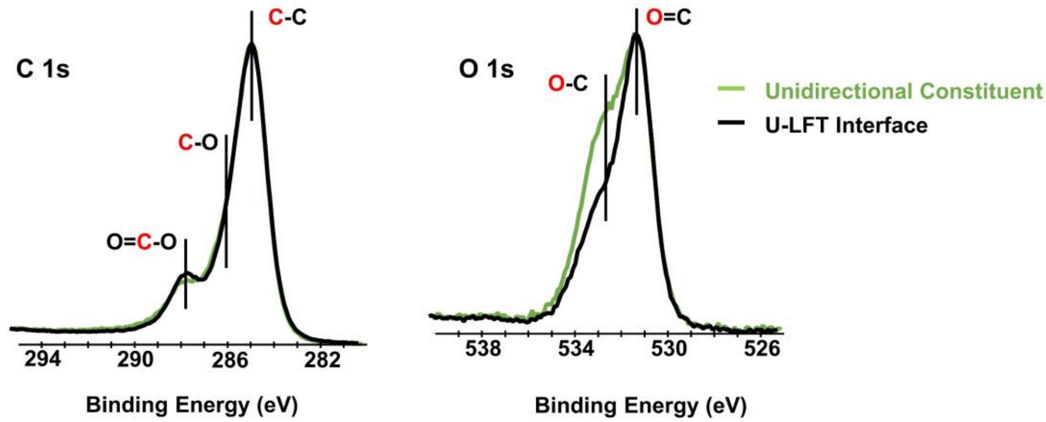

Figure 4.7: XPS high resolution C1s and O1s spectra comparing unidirectional constituent and U-LFT interface.

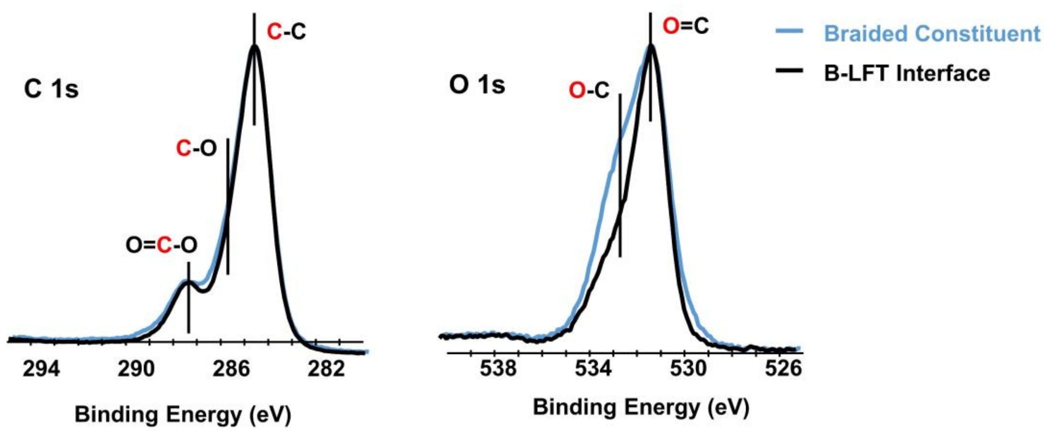

Figure 4.8: XPS high resolution C1s and O1s spectra comparing braided constituent and B-LFT interface.

Note that, the high-resolution spectra of C1s and O1s for individual constituents were different than the respective interfaces, indicating interfacial adhesion. There are no additional peak(s) observed at the interface of U-LFT and B-LFT (Figure 4.7 and 4.8) which confirms no chemical reaction appeared contributing to the interfacial adhesion.

4.3.1 Optical Microscopic Analysis

The interface between LFT and continuous commingled fiber reinforcement (skin) is enabled by thermal fusion bonding. The degree of bonding between LFT and commingled skin is guided by the cohesion and adhesion forces. Similar matrix system i.e., PA6 polymer in LFT and continuous commingled reinforcement improves the interdiffusion of polymer chains across the interface. Discontinuous-continuous fiber bridging across the interface and mechanical adhesion due to uneven surface at the interphase also contributes to interfacial bonding (see Figure 4.9 b, d). Thus, these all-collective pieces of evidence corroborate a strong mechanical bond between LFT and commingled skin.

Both U-LFT and B-LFT samples indicate surface voids, and it is inferred that they may occur during sample preparation or could be artifacts [19, 25] of the the density difference between CF and PA6 matrix. The density of CF is 1.78 g/cc and PA6 is 1.13 g/cc). The skin-to-core ratio was ~1:12.35 in case of U-LFT (Figure 4.9 a). However, in case of B-LFT (Figure 4.9 c) the skin to core ratio fluctuates in the range of 1:8.08 ~ 1:11.91. The skin to core fluctuation is attributed to the triaxial braided commingled fiber which causes variations in interface contact to the LFT core.

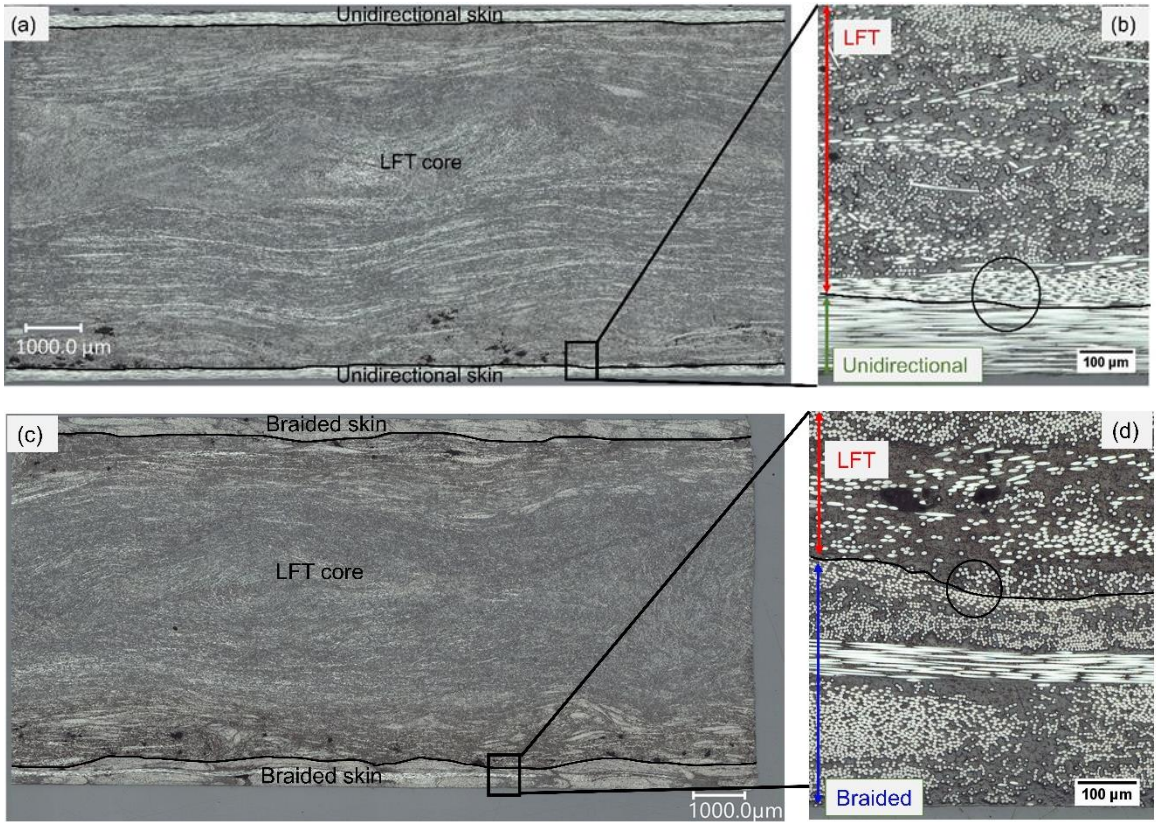

Figure 4.9: Optical image illustrating interface between; LFT and unidirectional commingled fiber reinforcement (a, b), and LFT and braided commingled fiber reinforcement (c, d). Skin to core thickness ratio was maintained to ~1:10 across the samples. The bond strength is influenced by interdiffusion, fiber bridging and mechanical adhesion due to uneven surface at interphase.

According to Hartoni et al. [26], the bending strength increased by 61% as skin to core ratio increased from 1:5.55 to 1:11.67. It is expected that higher skin to core ratio provides higher bending and shear properties without encumbering significant weight penalty [27]. Hence, skin to core ratio was maintained at 1:11.17 on an average in the case of U-LFT and B-LFT.

4.3.2 Vibration Testing

Vibration testing of the three types of composites (LFT, U-LFT, and B-LFT) provided insight into the dynamic properties of the sandwich composites. Figure 4.10 displays the resonant frequency and damping ratio for each, and Table 4.3 summarizes the vibration results. The resonant frequency ranked as follows: LFT< B-LFT < U-LFT. The damping ratio ranked as U-LFT < B-LFT < LFT.

The LFT has an average resonant frequency of 265 Hz and standard deviation of 29 Hz. The U-LFT exhibited an average resonance frequency of 462 Hz due to its high stiffness, and standard deviation of 6 Hz. The B-LFT structure exhibited an average resonant frequency of 395 Hz and deviation of 16 Hz. The standard deviation in resonant frequency was the highest for the constituent LFT and least (narrow) for the unidirectional overmolded composites.

The U-LFT has highly aligned fibers in the direction of dynamic flexure. The highly aligned fibers results into higher stiffness and higher storage modulus [28, 29]. However damping ratio is inversely proportional to fiber orientation.

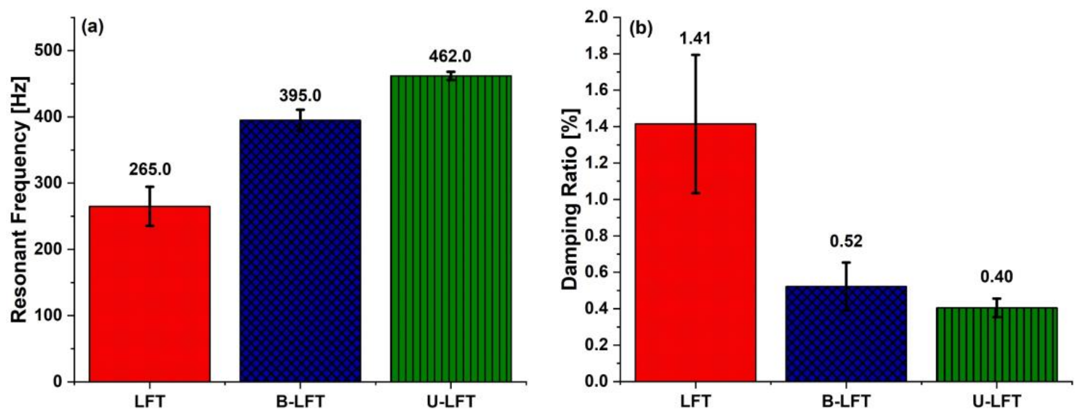

Figure 4.10: Vibration results for the (a) resonant frequency and (b) damping ratio of LFT, U-LFT, and B-LFT.

Table 4.3: Vibration analysis results showing frequency and damping ratio of each material.

Material	Mode 1			
	Frequency Avg. (Hz)	Frequency STD (Hz)	Damping Ratio Avg. (%)	Damping Ratio STD (%)
LFT	265	29	1.41	0.38
U-LFT	462	6	0.40	0.05
B-LFT	395	16	0.52	0.13

Hence in case of U-LFT, the resonant frequency increased by 74.3 % and the damping ratio reduced by 74% compared to constituent LFT. The B-LFT has continuous angled fiber plies in $0^{o} \pm 60^{o}$. Hence its stiffness is in between that of LFT and U-LFT as evidenced by intermediate resonant frequency (395 Hz) and damping ratio (0.52%). The LFT has random discontinuous microstructure resulting in the lowest stiffness and storage modulus. This yields a lower resonant frequency (265 Hz) and highest damping ratio (1.41%) due to a viscoelastic response caused by the polymer matrix [30, 31].

For comparison purpose, the damping ratio for the unidirectional constituent and braided constituent were evaluated. It is found to be 0.42% and 1.19%, respectively. This displays that cost effective LFT material does not alter the dynamic damping response of U-LFT. Whereas the damping ratio of the braided constituent is more than double the B-LFT. This is due to the multiple layers of braided fibers, each off-axis to the dynamic flexure, contributing to a large viscoelastic response whereas the B-LFT only has one layer contributing. Further investigation is necessary. This data will help to conclude that overmolded sandwich composite provides balance strength, stiffness, and comparable damping characteristics and it can be tailored as per the application.

4.3.3 Thermomechanical Analysis (TMA)

Figure 4.11 show typical curves of thermal expansion of LFT, U-LFT, and B-LFT in longitudinal direction. Coefficient of linear thermal expansion (CLTE often referred to as "α") were calculated from these curves using equation 4.1. All samples exhibited linear expansion for the 60-120^{o}C temperature region. Therefore, CLTE was determined from these curves using linear regression between 60^{o}C and 120^{o}C temperature. The mean CLTE of U-LFT and B-LFT decreased by 88.17% and 61.67% compared to LFT composite, respectively.

$$\alpha_l = \frac{\Delta L_{sp} \times k}{L \times \Delta T} \qquad \text{(Eq 4.1)}$$

Where α_l is longitudinal CLTE (μm/m.^{o}C), ΔL_{sp} is change in specimen length (μm), k is calibration coefficient (1.0201), L is specimen length at room temperature (m), and ΔT is temperature difference over which the change in specimen length is measured (^{o}C).

Kulkarni et al. [32] used transmission election microscopy (TEM) to measure the CLTE of PAN based IM7 CFs. They reported the axial and transverse CLTE of IM7 CFs as -0.4 and 5.6 μm/m.^{o}C, respectively. Besides that, it is also mentioned that the polymeric composite made from IM7 CF possess higher CLTE value buts closer to CLTE value of fiber. The U-LFT and B-LFT CLTE values complies well with the literature. Thus, collectively all pieces of information clearly indicate that continuous fiber reinforcement (skin) dominates the dimension stability of U-LFT and B-LFT composite.

The manufacturer datasheets [33, 34] of PA6-CF (3mm) pellet reported that CLTE of pellets were 14 μm/m.oC, which is 23.99% lower than PA6-CF LFT (18.42 μm/m.^{o}C) composite. In our study higher CLTE values were recorded in longitudinal direction. This could be the result of the surface roughness of the sample surface and the possibility of non-uniform distribution of fibers [35].

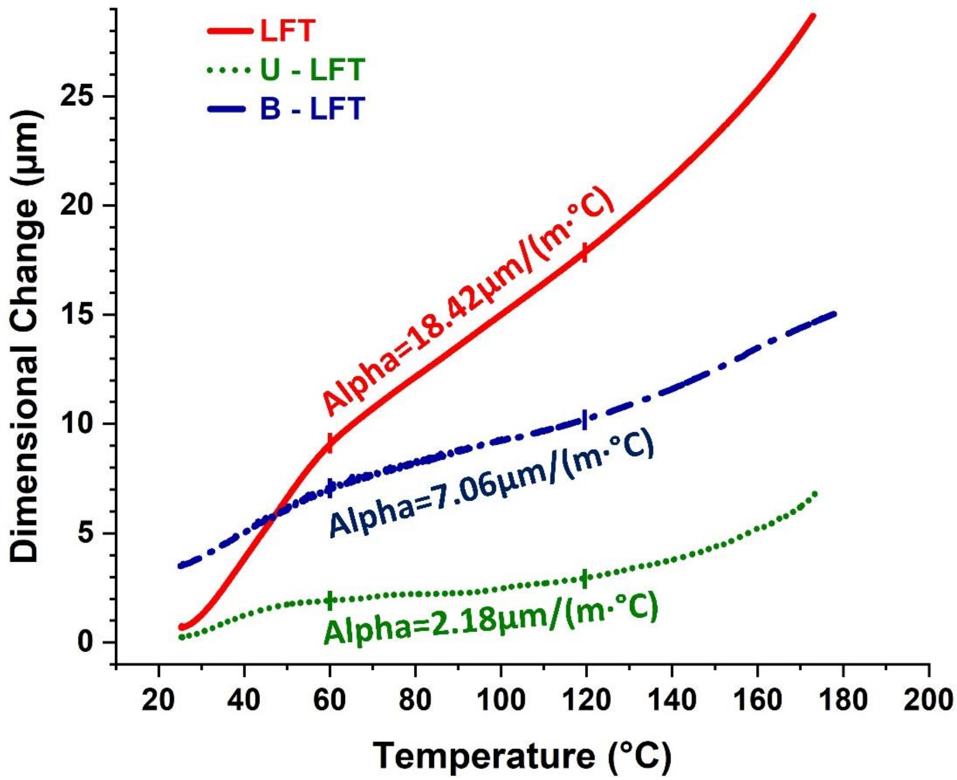

Figure 4.11: Comparison of thermal expansion of LFT, U-LFT, and B-LFT in longitudinal direction when subjected to constant heating rate of 5°C/min. CLTE is evaluated for the desired temperature range of 60°C - 120°C.

In foam and honeycomb sandwich structures, CLTE of the core material ranges between 23 to 37 µm/m°C [36, 37] whereas CLTE of unidirectional carbon skin ranges between -0.1 to 0.85 µm/m°C. The significant difference in the thermal expansion rate in the skin and core can lead to cracks and delamination. However, in U-LFT, and B-LFT the thermal expansion difference between skin and core is in the range of 16.24~11.36 µm/m°C, respectively. The thermal expansion difference is 55.08%~50.82% lower than reported in literature [36, 37]. This validates that U-LFT and B-LFT are suitable candidates for high performance applications.

4.3.4 Mechanical Testing

The mechanical testing considered the constituent LFT core as well as the sandwich composites comprising the LFT core with the unidirectional and braided skins. The purpose of this comparison was to evaluate the relative contributions of the constituents in the mechanical response. Table 4.4 and Figure 4.12 displays the mechanical properties of LFT, U-LFT, and B-LFT samples.

The flexural and tensile properties of U-LFT and B-LFT samples are compared with LFT composite. Flexural strength and modulus of U-LFT were 129.54% and 191.51% higher, respectively, than the LFT. Similarly, B-LFT showed 81.33% and 94.20% higher flexural strength and modulus, respectively, than the constituent LFT.

Table 4.4: Mechanical properties of constituent LFT core, U-LFT, and B-LFT sandwich composite

Material system	Flexural properties		Tensile properties	
	Strength (MPa)	Modulus (GPa)	Strength (MPa)	Modulus (GPa)
LFT	268.77 ± 10.25	14.13 ± 0.10	192.94 ± 13.24	15.28 ± 0.31
U-LFT	616.94 ± 62.43	41.19 ± 4.35	519.26 ± 20.69	33.25 ± 2.71
B-LFT	487.35 ± 10.34	27.44 ± 1.24	434.40 ± 58.71	23.80 ± 2.13

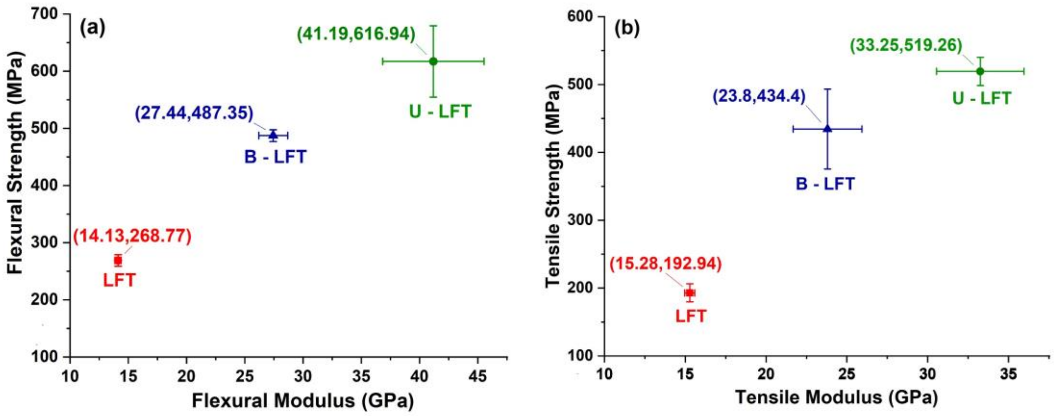

Figure 4.12: Mechanical properties of LFT, U-LFT, and B-LFT composite; (a) flexural strength versus flexural modulus, and (b) tensile strength versus tensile modulus.

A similar trend can be observed in tensile properties. Tensile strength and modulus of U-LFT were 169.13% and 117.61% higher, respectively, than the constituent LFT. Similarly, B-LFT showed 125.15% and 49.22% superior tensile strength and modulus, respectively, compared with the LFT. The bending and tensile results illustrate that the sandwich produced via continuous commingled fiber overmolding process enhances the mechanical performance of LFT core by 105.43~147.14% on an average.

The unidirectional constituent and braided constituent skins were tested in longitudinal and transverse direction for tensile properties. These results are summarized in Table 4.5, section 4.3.7. The average tensile strength and modulus of unidirectional constituent in longitudinal direction were 1707.29 ± 42.88 MPa and 137.31 ± 10.16 GPa, respectively. Similarly, braided constituent demonstrated 514.12 ± 15.24 MPa and 41.66 ± 4.36 GPa, tensile strength and modulus, respectively. Tensile results of individual constituent demonstrate that the continuous commingled fiber skin dominates the performance of U-LFT and B-LFT sandwich composite.

4.3.5 Computational Analysis

Various mechanical tests performed in experiments provided material properties from the corresponding samples. Each mechanical test (e.g., tensile test) can provide the corresponding property (e.g., Young's modulus in 0^{o}) of the sample prepared with a certain configuration (e.g., U-LFT). In this section, the stiffness values of the materials were obtained via analytical methods and compared with experiments. The analytically obtained properties include 9 orthotropic stiffness values for each material system. The properties were then utilized to an aerospace application via a computational simulation, specifically a finite element analysis (FEA). For the analytical calculations, MCQ-Chopped (Ver. 2017) from AlphaSTAR Corp. was used. For the FEA simulations, ABAQUS (Ver. 2018) from SIMULIA were used. Detailed methods used in MCQ-Chopped and information about the simulation are shown in *Micromechanics Approach* and *FEA simulation* section.

Micromechanics Approach

Experiments were performed to obtain tensile moduli in two directions for LFT (along and cross charge flow induced fiber direction), unidirectional constituent (longitudinal and transverse to the fiber), and braided constituent (axial and hoop direction) as shown in Table 4.5. A minimum of four 25.4 × 254 mm (1 × 10 in.) specimens each were tested for statistical relevance.

The experimentally obtained tensile moduli (E_{11} and E_{22}) are insufficient for a computational simulation. Simulation requires a complete modulus tensor consisting of 9 independent constants (E_{11}, E_{22}, E_{33}, G_{12}, G_{23}, G_{13}, v_{12}, v_{23}, v_{13}) for an orthotropic material, and it is challenging to obtain all 9 constants via experiments. Therefore, modulus tensors have been constructed for LFT, unidirectional, and braided constituent by matching the experimentally obtained tensile moduli (E_{11} and E_{22}) shown in Table 4.5. Orthotropic modulus tensor was obtained using individual material properties (CF and PA6 polymer) and by using MCQ-Chopped (Ver. 2017) software from AlphaSTAR Corp.

Table 4.6 shows the material properties of CF and PA6 polymer used in the micromechanics approach to calculate effective moduli.

Table 4.5: Experimentally measured moduli in 0° and 90° directions for LFT, unidirectional constituent and braided fiber constituent

Composite Type	Stiffness test direction	Modulus (GPa)	Standard (Dev.)
LFT	0° (along charge flow induced fiber direction)	15.28	0.31
	90° (cross charge flow induced fiber direction)	10.07	3.1
Unidirectional constituent	0° (longitudinal to the fiber)	137.31	10.16
	90° (transverse to the fiber)	5.11	0.48
Braided constituent	0° (Axial direction for 0/±60 axes)	41.66	4.36
	90° (Hoop direction for 0/±60 axes)	37.89	1.76

Table 4.6: Referenced orthotropic properties of CF [38] and isotropic properties of PA6 polymer [39]

CF properties							
Property	Value [GPa]	Property	Value [GPa]	Property	Value	Property	Value [kg/m^3]
E_{11}	277	G_{12}	58.81	ν_{12}	0.2218	ρ	1780
E_{22}	18.86	G_{23}	6.96	ν_{23}	0.3548		
E_{33}	18.86	G_{13}	6.96	ν_{13}	0.3548		
PA6 properties							
E	2.68			ν	0.31	ρ	1130

The Young's modulus of a CF in a longitudinal direction was provided by Concordia Fibers. The remaining elastic properties of a CF were taken from reference [38]. The properties of PA6 polymer were taken from reference [39].

Computation of Orthotropic Modulus Tensor of LFT

In LFT, the fibers have random orientation. According to Halpin and Pagano [40], heterogeneous material with randomly oriented fibers is equivalent to a laminate consisting of multiple plies with a different fiber direction within each ply. The equation 4.2 to 4.5 shows that the elastic coefficients for orthotropic random fiber composite [40].

$$\bar{E} \equiv \frac{4U_5(U_1 - U_5)}{U_1} \qquad \text{(Eq 4.2)}$$

$$\bar{\nu} \equiv \frac{(U_1 - 2U_5)}{U_1} \qquad \text{(Eq 4.3)}$$

$$\bar{G} \equiv U_5 \qquad \text{(Eq 4.4)}$$

Where $U_1 = \frac{(3Q_{11}+3Q_{22}+ 2Q_{12}+ 4Q_{66})}{8}$ $and\ U_5 = \frac{(Q_{11}+Q_{22}- 2Q_{12}+ 4Q_{66})}{8}$ with

$$Q_{11} = \frac{E_{11}}{(1-\nu_{12}\nu_{21})},\ Q_{22} = \frac{E_{22}}{(1-\nu_{12}\nu_{21})},\ Q_{12} = \nu_{12}Q_{22} = \nu_{21}Q_{11},\ Q_{66} = G_{12}$$

The same analogy can be used to find the fiber orientation distribution within LFT. Hence, a physics-based approach [41, 42] was implemented to reverse engineer orientation of fiber as shown in Figure 4.13. This procedure utilized a de-homogenization technique [43] involving finding the distribution of fiber orientation that satisfies the along and cross direction stiffness values from experiments. The details of the approach are shown in reference [38]. Commercial software, MCQ-Chopped (Ver. 2017) by AlphaSTAR Corp., was used for this approach.

First, the orthotropic stiffness tensor of a composite material with aligned fibers was obtained using the micromechanics approach. The composite material consist of the same composition as the LFT sample (PA6 with 40 wt. % CF) but the fibers are assumed to be aligned in one direction.

Second, using the physics-based approach with reverse engineering, the fiber orientations (or layer orientations) were estimated to match the experimentally obtained moduli in the flow direction (15.28 GPa) and the cross-flow direction (10.07 GPa). This process is equivalent to finding an optimal laminate configuration consisting of multiple unidirectional plies with various thicknesses. Figure 4.14 shows the fiber orientation and corresponding volume ratio (i.e., the amount of fibers normalized in each orientation). It should be noted that in Figure 4.14, length of the line does not correspond to the fiber length. However, the length of line represents the percent amount of fibers and the angle with respect to the x-axis. The sum of the lengths of all lines is 1.0.

Third, the effective orthotropic elastic modulus tensor was constructed [40, 44] using the fiber orientation distribution data as in Figure 4.14. The moduli of the LFT composite material from the de-homogenization technique is shown in Table 4.7. It should be noted that the reverse engineered E_{11} and E_{22} moduli (15.35 GPa and 10.14 GPa) are close to the experimentally obtained E_{11} and E_{22} (15.28 GPa and 10.07 GPa).

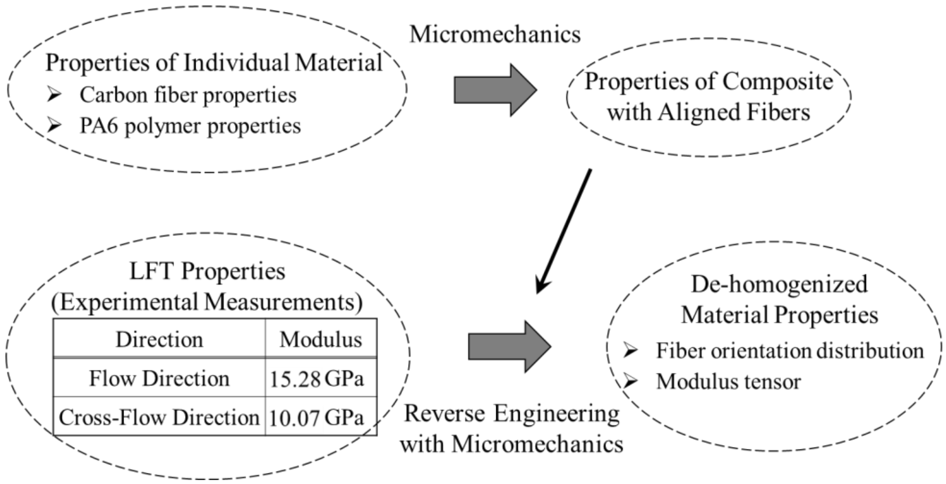

Figure 4.13: Flowchart of a reverse engineering with a de-homogenization technique for orthotropic material properties

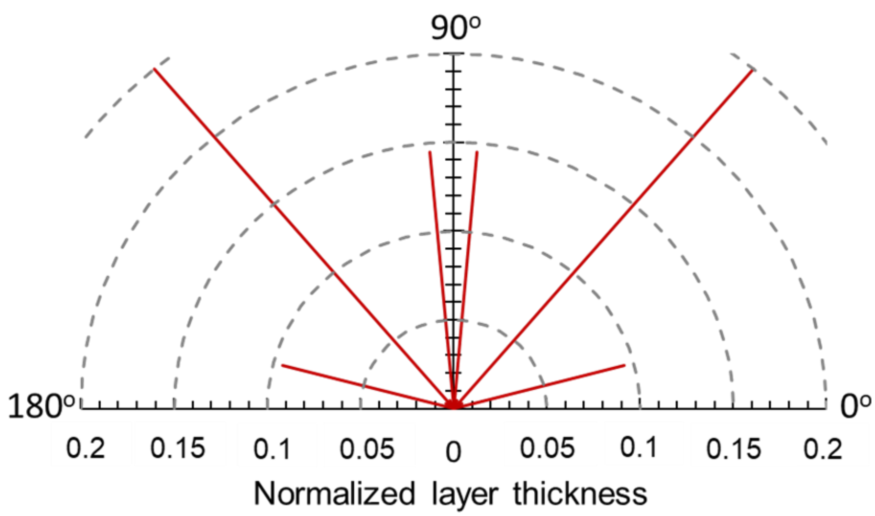

Figure 4.14: The fiber orientation distribution of LFT. The angle between the line and x-axis indicates the orientation of the fibers and the length indicates the amount of the fibers in the corresponding orientation.

Table 4.7: Effective orthotropic elastic modulus tensor of LFT obtained using reverse engineering and micromechanics [40-43]

Property	Value [GPa]	Property	Value [GPa]	Property	Value	Property	Value [kg/m^3]
E_{11}	15.35	G_{12}	5.497	ν_{12}	0.4457	ρ	1325
E_{22}	10.14	G_{23}	1.634	ν_{23}	0.3075		
E_{33}	4.782	G_{13}	1.649	ν_{13}	0.2475		

Computation of Orthotropic Modulus Tensor of Braided Constituent

The braided material has an intrinsic waviness in the fibers (see Figure 4.9, section 4.3.3) which results in lower modulus values than the stiffnesses obtained via the classical laminate plate theory [45]. Therefore, E_{11} and E_{22} needed to estimate such way that it should match the experimentally obtained moduli in axial (41.66 GPa) and hoop (37.89 GPa) direction. Hence for computational purpose braided constituent was treated as an equivalent discontinuous fiber-reinforced polymer with a reduced fiber length. By using similar approach as shown for LFT composite, an effective orthotropic elastic modulus tensor for braided constituent was obtained (shown in Table 4.8). It should be noted that the values in E_{11} and E_{22} are the same. It is also noted that a truss with an isogrid (0°/±60° triangulated grid) configuration provides uniform stiffness in all directions as shown in Figure 3.9 [46]. In experiments performed in our study, E_{11} (41.66 GPa) was slightly higher than E_{22} (37.89 GPa) (Table 4.5).

Computation of Orthotropic Modulus Tensor of Unidirectional Constituent

The weight fraction of 59 wt % was considered for the unidirectional CF. The micromechanics approach for unidirectional CF assumed uniformly distributed aligned fibers in a matrix within an idealized representative volume [44]. Using commercial software, MCQ-Chopped (Ver. 2017) by AlphaSTAR Corp. and micromechanics approach, an orthotropic effective modulus tensor of unidirectional constituent has been obtained and listed in Table 4.9. The experimentally obtained moduli (137 GPa and 5.1 GPa) shown in Table 4.5 are in good agreement with the effective modulus values (133 GPa and 5.7 GPa) obtained from MCQ-Chopped.

Table 4.8: Effective orthotropic elastic modulus tensor of braided constituent obtained using a micromechanics [40, 44]

Property	Value [GPa]	Property	Value [GPa]	Property	Value	Property	Value [kg/m^3]
E_{11}	40.20	G_{12}	15.18	ν_{12}	0.3242	ρ	1444
E_{22}	40.20	G_{23}	2.277	ν_{23}	0.2922		
E_{33}	6.535	G_{13}	2.277	ν_{13}	0.2922		

Table 4.9: Orthotropic effective modulus of unidirectional constituent obtained using micromechanics [44]

Property	Value [GPa]	Property	Value [GPa]	Property	Value	Property	Value [kg/m^3]
E_{11}	133	G_{12}	2.19	ν_{12}	0.2606	ρ	1444
E_{22}	5.74	G_{23}	2.19	ν_{23}	0.4119		
E_{33}	5.73	G_{13}	2.47	ν_{13}	0.3360		

FEA Simulation of U-LFT and B-LFT for Airplane Wing Application

In *Micromechanics Approach* section, orthotropic material properties were obtained for LFT, unidirectional and braided constituent. The approaches involved micromechanics with reverse engineering from experimentally obtained stiffness values in the flow direction and crossflow direction. The micromechanics study resulted in 9 independent constants for orthotropic stiffness tensor. As an application of the U-LFT and B-LFT, a remote control (RC) airplane wing was chosen for computational analysis. The properties were calculated from the micromechanics approach were used for finite element analysis. Further, the deflection of an RC plane wing was obtained.

Airfoil Design and Loading Conditions

The dimensions and the design of the RC wing are shown in Figure 4.15 [47]. Two-material layup designs were considered: U-LFT and B-LFT. For the U-LFT layup, the wing consists of unidirectional constituent (0.213 mm thick) as an outer layer and LFT (1.0 mm thick) as an inner layer. For the B-LFT layup, the wing consists of braided constituent (0.672 mm thick) as an outer layer and LFT (1.0 mm thick) as an inner layer.

NACA 2410 is one of the airfoil shapes developed by National Advisory Committee for Aeronautics (NACA). In this study, the airfoil NACA 2410 shape with the chord length of 207.6 mm were considered [47]. NACA airfoils are commonly used in aircraft and their aerodynamic behavior is well studied including the lift coefficient and the angle of attack [48]. The coefficient of lift is a measure of how much lift the wing can produce and can only be changed by changing the shape of wing or the angle of attack at which it cuts through the relative wind. As the angle of attack increases, lift increases.

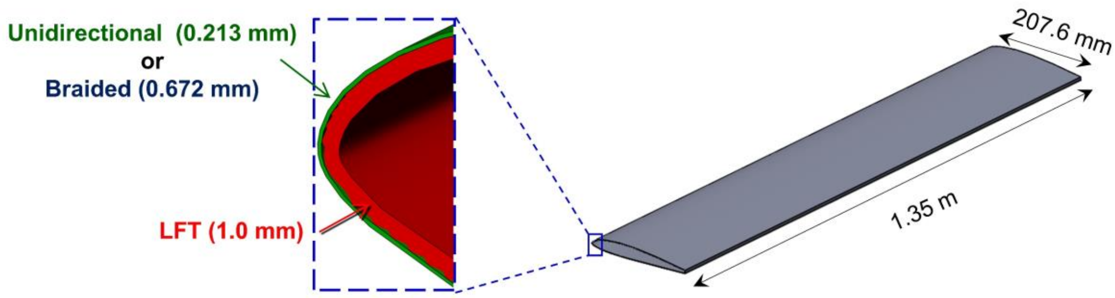

Figure 4.15: RC plane wing structure made of U-LFT or B-LFT and the dimensions.

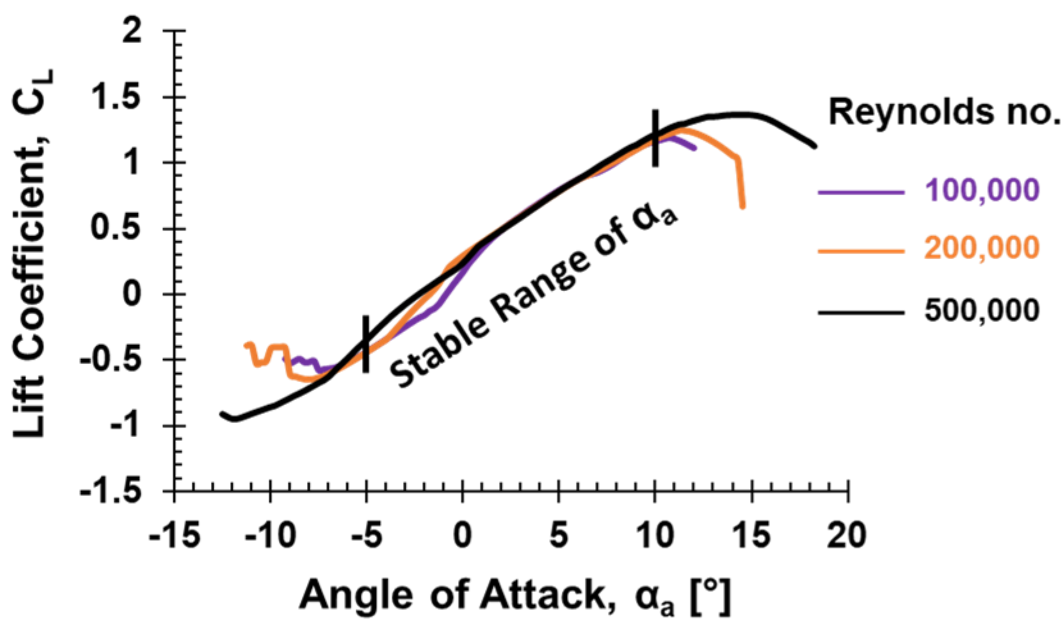

Figure 4.16: Lift coefficient as a function of the angle of attack for NACA 2410 showing stable range for laminar wing airflow. Adopted from reference [47].

When wing reaches the maximum angle of attack, lift begins to diminish rapidly. This is referred as stalling angle of attack which is an undesirable phenomenon for any airplane. Hence for any given wing, desired laminar airflow can be obtained from stable region of angle of attack (α_a = -5 to α_a =10) as shown in Figure 4.16 [47].

For simulation purpose, it was necessary to evaluate required wing lift forces (loading condition) for NACA 2410 airfoil designed with U-LFT and B-LFT material. The required lift force can be evaluated using the equation 4.5 and Figure 4.16 adopted from reference [47].

$$L = \frac{1}{2}\rho V^2 A_w C_L \qquad \text{(Eq 4.5)}$$

where L is the lift force, ρ is the fluid density (air density, 1.225 kg/m^3 [47]), V is the velocity (15 m/s [47]), A_w is the wing area (0.26 m^2), and C_L is lift coefficient which is evaluated from Figure 4.16.

As mentioned earlier, for desired laminar airflow, the value of C_L need to be chosen from stable range of angle of attack α_a = -5° and α_a = 10° (see Figure 4.15). Hence for the analysis, the value of C_L of 0.5 were chosen since it corresponds to the mid point of the stable range (α_a = 2.5°).

The calculated lift force L became 17.9 N which is roughly equivalent to 1.8 kg of mass. The mass of the wing is 0.95 kg for the U-LFT layup and 1.35 kg for the B-LFT layup. The parameters chosen in this study provided the lift force close to the equivalent weight after combining fuselage, battery, and other electric components.

Figure 4.17 (a) shows the load conditions and the boundary conditions. The pink surface in the figure will be attached to the fuselage, and therefore, a fixed boundary condition was applied. The fuselage area is located at the center of the wing, and the width is 93.4 mm. A uniform pressure of 34.4 Pa was applied to the surface in the lift direction. The surface of the wing was discretized into 24k shell element (S4R) with a reduced integration. The orthotropic material properties (taken from *Micromechanics Approach* section) were applied to the wing with the orientation direction (0° direction) parallel to the wing span direction as shown in Figure 4.17 (b). Two plies were applied to the shell elements with the LFT as the first ply with the layer thickness of 1 mm and unidirectional (0.213 mm thick) or the braided (0.672 mm thick) as the second ply.

Airfoil Simulation Results

The simulations were performed via ABAQUS (Ver. 2018) by SIMULIA. Figure 4.18 shows the results of the simulation. Figure 4.18 (a) is from the U-LFT wing and Figure 4.18 (b) is from the B-LFT wing. The maximum deflection at the tip are 0.272 mm and 0.207 mm for the U-LFT wing and the B-LFT wing, respectively. The performances of the two wing structures were compared to each other. The effective specific stiffness of the wing was obtained via the inverse of the maximum deflection divided by its weight.

The effective specific stiffness values from the U-LFT wing and the B-LFT wing are 7.73 $mm^{-1} \cdot kg^{-1}$ and 7.17 $mm^{-1} \cdot kg^{-1}$, respectively. Therefore, the U-LFT wing shows 8% higher performance than the B-LFT wing.

Katifes et al. [49] performed an analysis on a hypothetical design of an aircraft wing with no tapering and obtained the maximum deflection of 120 mm. If the material is replaced by U-LFT with the Young’s modulus of 133 GPa, the maximum deflection will be 42.4 mm.

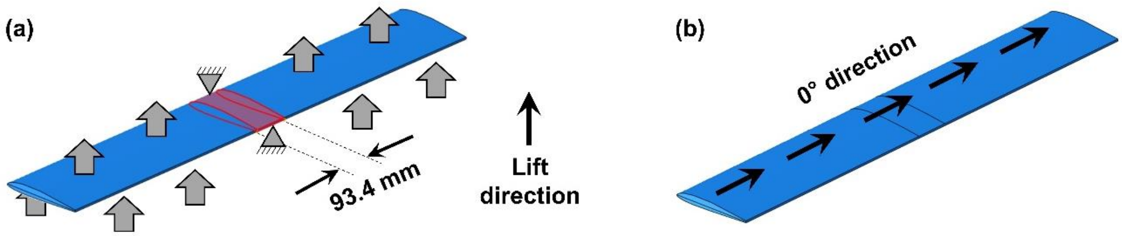

Figure 4.17: Model set up of RC wing for FEA (a) load and boundary conditions. The center of the wing will be attached to the fuselage, and therefore, a fixed boundary condition was applied. (b) The orientation direction (0° direction) of the orthotropic properties of the elements.

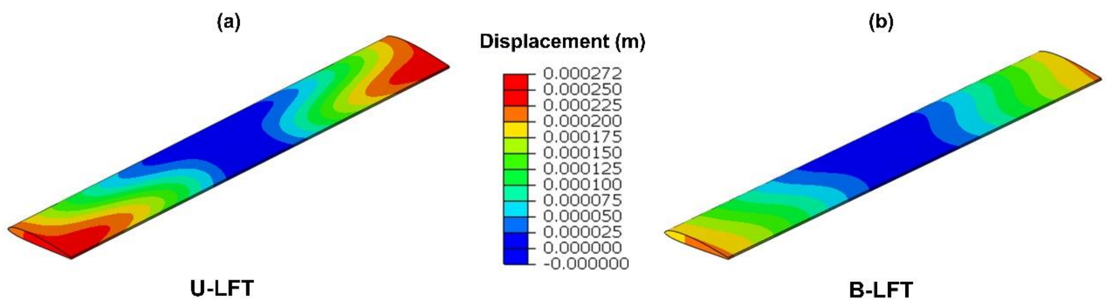

Figure 4.18: Simulation results from (a) U-LFT wing and (b) the B-LFT wing. The color map represents the displacement.

In FEA simulation section, NACA 2410 airfoil designed with U-LFT and B-LFT material. The required lift forces (loading condition) were evaluated from Figure 4.15 and equation 4.2. The loading and boundary conditions were applied and further the deflection of an RC plane wing was obtained. B-LFT wing shows less deflection than U-LFT wing. However, U-LFT wing shows 8% higher specific effective stiffness compared to B-LFT wing and it is due to 30% lower weight of U-LFT wing compared to B-LFT.

4.4 Summary

In this study, processing and molding conditions governed by DSC and TGA used during the manufacturing of PA6-CF overmolded sandwich composites. XPS analysis showed that no chemical reaction between comminlged skin(s) and LFT occurred during sandwich fabrication. Microscopic investigation provided evidence of mechanical interfacial bonding of the commingled skin(s) – LFT which is governed by interdiffusion of polymer chains, discontinuous-continuous fiber bridging and mechanical adhesion due to uneven surface at the interphase. Vibrational results of overmolded sandwich composite validated that comparable damping characteristics can be achieved along with balanced strength and stiffness.

In case of U-LFT and B-LFT the thermal expansion difference between skin and core is 16.24~11.36 μm/m.ºC which is 55.08%~50.82% lower than the reported foam and honeycomb based sandwich composites. The mechanical (bending and tensile) results illustrate that the sandwich produced via continuous commingled fiber overmolding process enhances the mechanical performance of LFT core by 105.43~147.14% on an average and it is dominated by continuous commingled fiber skin. The computational approach involved micromechanics with reverse engineering to obtain orthotropic stiffness tensors and FEA simulation of U-LFT wing and B-LFT wing. U-LFT wing shows 8% higher specific effective stiffness compared to B-LFT wing. The higher effective stiffness is attributed to 30% lower weight of U-LFT wing compared to B-LFT.

The innovative overmolding approach for sandwich fabrication provides ability to tailor stiffness, strength, design freedom, damage tolerance for a broad range of structural applications without considerable increase in weight and compelling cost savings.

References

[1] I. M. Daniel, E. E. Gdoutos, and Y. D. S. Rajapakse, Major accomplishments in composite materials and sandwich structures: An anthology of ONR sponsored research. 2009. doi: 10.1007/978-90-481-3141-9.

[2] D. M. Mcgowan and D. R. Ambur, “Damage-Tolerance Characteristics of Composite Fuselage Sandwich Structures With Thick Facesheets,” 1997.

[3] A. Alhajahmad and C. Mittelstedt, “Minimum weight design of curvilinearly grid-stiffened variable-stiffness composite fuselage panels considering buckling and manufacturing constraints,” Thin-Walled Structures, vol. 161, Apr. 2021, doi: 10.1016/j.tws.2021.107526.

[4] B. Hayman, “Approaches to damage assessment and damage tolerance for FRP sandwich structures,” Journal of Sandwich Structures and Materials, vol. 9, no. 6, 2007, doi: 10.1177/1099636207070853.

[5] H. Schwarts-Givli, O. Rabinovitch, and Y. Frostig, “High-order nonlinear contact effects in the dynamic behavior of delaminated sandwich panels with a flexible core,” International Journal of Solids and Structures, vol. 44, no. 1, 2007, doi: 10.1016/j.ijsolstr.2006.04.016.

[6] S. M. Huybrechts, T. E. Meink, P. M. Wegner, and J. M. Ganley, “Manufacturing theory for advanced grid stiffened structures,” Composites - Part A: Applied Science and Manufacturing, vol. 33, no. 2, 2002, doi: 10.1016/S1359-835X(01)00113-0.

[7] F. Kamareh, A. Farrokhabadi, and G. Rahimi, “Experimental and numerical investigation of skin/lattice stiffener debonding growth in composite panels under bending loading,” Engineering Fracture Mechanics, vol. 190, 2018, doi: 10.1016/j.engfracmech.2017.12.043.

[8] M. Mohamed, Z. Huo, S. Hawkins, K. Chandrashekhara, V. Birman, and J. Volz, “Moisture effects on performance of polyurethane composite sandwich panels manufactured using vartm,” 2013.

[9] G. Zhou, M. Hill, and N. Hookham, “Investigation of Parameters Dictating Damage and Energy Absorption Characteristics in Sandwich Panels,” in Sandwich Structures 7: Advancing with Sandwich Structures and Materials, 2005. doi: 10.1007/1-4020-3848-8_37.

[10] D. P. W. Horrigan, R. R. Aitken, and G. Moltschaniwskyj, “Modelling of Crushing Due to Impact in Honeycomb Sandwiches,” Journal of Sandwich Structures & Materials, vol. 2, no. 2, 2000, doi: 10.1177/109963620000200203.

[11] S. Shroff, E. Acar, and C. Kassapoglou, “Design, analysis, fabrication, and testing of composite grid-stiffened panels for aircraft structures,” Thin-Walled Structures, vol. 119, pp. 235–246, Oct. 2017, doi: 10.1016/J.TWS.2017.06.006.

[12] G. H. Rahimi, M. Zandi, and S. F. Rasouli, “Analysis of the effect of stiffener profile on buckling strength in composite isogrid stiffened shell under axial loading,” Aerospace Science and Technology, vol. 24, no. 1, 2013, doi: 10.1016/j.ast.2011.11.007.

[13] H. Ahmadi and G. Rahimi, “Analytical and experimental investigation of transverse loading on grid stiffened composite panels,” Composites Part B: Engineering, vol. 159, 2019, doi: 10.1016/j.compositesb.2018.09.040.

[14] E. Lamanna, N. Gupta, P. Cappa, O. M. Strbik, and K. Cho, “Evaluation of the dynamic properties of an aluminum syntactic foam core sandwich,” Journal of Alloys and Compounds, vol. 695, pp. 2987–2994, Feb. 2017, doi: 10.1016/J.JALLCOM.2016.11.361.

[15] U. K. Vaidya, S. Pillay, S. Bartus, C. A. Ulven, D. T. Grow, and B. Mathew, “Impact and post-impact vibration response of protective metal foam composite sandwich plates,” Materials Science and Engineering: A, vol. 428, no. 1–2, pp. 59–66, Jul. 2006, doi: 10.1016/J.MSEA.2006.04.114.

[16] S. Alwekar, P. Yeole, V. Kumar, A. A. Hassen, V. Kunc, and U. K. Vaidya, “Melt extruded versus extrusion compression molded glass-polypropylene long fiber thermoplastic composites,” Composites Part A: Applied Science and Manufacturing, vol. 144, p. 106349, May 2021, doi: 10.1016/j.compositesa.2021.106349.

[17] N. Wiegand and E. Mäder, “Commingled yarn spinning for thermoplastic/glass fiber composites,” Fibers, vol. 5, no. 3, 2017, doi: 10.3390/fib5030026.

[18] B.-D. Choi, O. Diestel, and P. Offermann, “Commingled CF/PEEK Hybrid Yarns for Use in Textile Reinforced High Performance Rotors,” 1999.

[19] S. Alwekar, R. Ogle, S. Kim, and U. Vaidya, “Manufacturing and characterization of continuous fiber-reinforced thermoplastic tape overmolded long fiber

thermoplastic," Composites Part B: Engineering, vol. 207, 2021, doi: 10.1016/j.compositesb.2020.108597.

[20] U. Vaidya, A. Goel, K. C.-A. Composites, and undefined 2009, "Fatigue and vibration response of long fiber reinforced thermoplastics," temp.speautomotive.com, Accessed: Aug. 27, 2021.

[21] ASTM, "Standard Test Method for Measuring Vibration-Damping Properties of Materials 1," Astm, vol. 05, no. Reapproved 2010, pp. 1–14, 2015.

[22] A. A. Hassen, P. Barfknecht, M. Shehadeh, and U. Vaidya, "Non-Destructive Characterization of Fiber Orientation in Long Fiber Thermoplastic Composites Using Vibration-Based Method," 2015.

[23] K. I. Budhwani, M. Janney, and U. K. Vaidya, "Vibration-based nondestructive testing to determine viability of parts produced with recycled thermoplastic composites," Materials Evaluation, vol. 74, no. 2, 2016.

[24] U. K. Vaidya, A. Goel, and K. Chawla, "Fatigue and vibration response of long fiber reinforced thermoplastics," 2009.

[25] S. Patanè, P. G. Gucciardi, M. Labardi, and M. Allegrini, "Apertureless near-field optical microscopy," Rivista del Nuovo Cimento, vol. 27, no. 1, 2004, doi: 10.3367/ufnr.2016.05.037817.

[26] H. Hartoni, J. Fajrin, B. Anshari, and A. D. Catur, "Effect of core and skin thicknesses of bamboo sandwich composite on bending strength," International Journal of Mechanical Engineering and Technology, vol. 8, no. 12, 2017.

[27] Uday. Vaidya, “Composites for automotive, truck and mass transit : materials, design, manufacturing,” p. 419, 2011.

[28] S. A. Suarez, R. F. Gibson, C. T. Sun, and S. K. Chaturvedi, “The influence of fiber length and fiber orientation on damping and stiffness of polymer composite materials,” Experimental Mechanics 1986 26:2, vol. 26, no. 2, pp. 175–184, Jun. 1986, doi: 10.1007/BF02320012.

[29] R. F. Gibson and A. Yau, “Complex Moduli of Chopped Fiber and Continuous Fiber Composites: Comparison of Measurements with Estimated Bounds:” http://dx.doi.org/10.1177/002199838001400207, vol. 14, no. 2, pp. 155–167, 1980, doi: 10.1177/002199838001400207.

[30] V. Arumuga prabu, M. Uthayakumar, V. Manikandan, N. Rajini, and P. Jeyaraj, “Influence of redmud on the mechanical, damping and chemical resistance properties of banana/polyester hybrid composites,” Materials and Design, vol. 64, 2014, doi: 10.1016/j.matdes.2014.07.020.

[31] S. Manoharan, B. Suresha, G. Ramadoss, and B. Bharath, “Effect of Short Fiber Reinforcement on Mechanical Properties of Hybrid Phenolic Composites,” Journal of Materials, vol. 2014, 2014, doi: 10.1155/2014/478549.

[32] R. Kulkarni and O. Ochoa, “Transverse and longitudinal CTE measurements of carbon fibers and their impact on interfacial residual stresses in composites,” Journal of Composite Materials, vol. 40, no. 8, 2006, doi: 10.1177/0021998305055545.

[33] “Polyamide - Nylon 6, 6 - 30% Carbon Fiber Reinforced Polymer - online catalog source - supplier of research materials in small quantities - Goodfellow.” http://www.goodfellow.com/A/Polyamide-Nylon-6-6-30-Carbon-Fiber-Reinforced-Polymer.html (accessed Aug. 24, 2021).

[34] “Thermal Properties of Plastic Materials Material Formula Coefficient of thermal expansion x10-6 K-1”.

[35] A. Tezvergil, L. V. J. Lassila, and P. K. Vallittu, “The effect of fiber orientation on the thermal expansion coefficients of fiber-reinforced composites,” Dental Materials, vol. 19, no. 6, pp. 471–477, Sep. 2003, doi: 10.1016/S0109-5641(02)00092-1.

[36] M. Rinker, M. Gutwinski, and R. Schäuble, “Experimental and Theoretical Investigation of Thermal Stress in CFRP Foam-core Sandwich Structures,” 2008.

[37] Chen H., Oakes D. W., and Wolff E. G., “Thermal expansion of honeycomb sandwich panels.” 1999. Accessed: Aug. 28, 2021.

[38] S. Kim et al., “Analysis on part distortion and residual stress in big area additive manufacturing with carbon fiber-reinforced thermoplastic using dehomogenization technique,” 2019.

[39] “RTP 200 A Nylon 6 (PA) Product Data Sheet - RTP Company.” http://web.rtpcompany.com/info/data/0200A/RTP200A.htm (accessed Aug. 29, 2021).

[40] J. C. Halpin and N. J. Pagano, “The Laminate Approximation for Randomly Oriented Fibrous Composites:” http://dx.doi.org/10.1177/002199836900300416, vol. 3, no. 4, pp. 720–724, Jul. 2016, doi: 10.1177/002199836900300416.

[41] H. Fukuda and K. Kawata, “On Young’s modulus of short fibre composites,” Fibre Science and Technology, vol. 7, no. 3, 1974, doi: 10.1016/0015-0568(74)90018-9.

[42] K. Jayaraman and M. T. Kortschot, “Correction to the Fukuda-Kawata Young’s modulus theory and the Fukuda-Chou strength theory for short fibre-reinforced composite materials,” Journal of Materials Science, vol. 31, no. 8, 1996, doi: 10.1007/BF00356627.

[43] C. Godines, S. DorMohammadi, F. Abdi, M. Villa Montero, D. Huang, and L. Minnetyan, “Damage tolerant composite design principles for aircraft components under static service loading using multi-scale progressive failure analysis,” Journal of Composite Materials, vol. 51, no. 10, 2017, doi: 10.1177/0021998316671575.

[44] C. T. Sun and J. L. Chen, “A micromechanical model for plastic behavior of fibrous composites,” Composites Science and Technology, vol. 40, no. 2, 1991, doi: 10.1016/0266-3538(91)90092-4.

[45] C. Kassapoglou, “Review of classical laminated plate theory,” Aerospace Series, 2013, doi: 10.1002/9781118536933.

[46] P. Chopra, “Effective mechanical properties of lattice materials,” 2011, doi: 10.14288/1.0072404.

[47] “NACA2410(naca2410-il).” http://airfoiltools.com/airfoil/details?airfoil=naca2410-il (accessed Aug. 29, 2021).

[48] I. H. Abbott, A. E. von Doenhoff, and L. S. , Jr. Stivers, “Summary of Airfoil Data,” 1945, Accessed: Sep. 04, 2021. [Online]. Available:https://digital.library.unt.edu/ark:/67531/metadc65534/

[49] “(PDF) Structural Analysis, Fatigue Analysis and Optimization of Aircraft Wings.” https://www.researchgate.net/publication/303855607_Structural_Analysis_Fatigue_Analysis_and_Optimization_of_Aircraft_Wings (accessed Aug. 29, 2021).

Overall Summary

In this study, long fiber thermoplastic (LFT) manufacturing techniques such as extrusion compression molding (ECM) , and melt extrusion were reviewed extensively. The review showed that existing manufacturing techniques provides different porosity content, fiber length distribution, and fiber orientation distribution which influences the mechanical, thermal, and microscopic properties of LFT composites. The fundamental study of process-microstructure-property relationships in LFT composites benefit to understand various processing methods in detail and its effect on performance of LFT composites. This work considered PP-GF LFT sheets processed via melt extrusion, which offers highly aligned fibers (referred to as “Tecnogor composites”), and PP-GF LFT composites produced via ECM, which offers a random distribution of fibers. Aligned fiber composites exhibited higher flexural strength (35%~65%), flexural modulus (132%~172%), tensile strength (39%~52%), tensile modulus (67%~75%), and Izod impact resistance (195%~220%) than the extrusion compression molded LFT composites. Based on the results, the study concluded that LFT composites can achieve superior mechanical performance by aligning the discontinuous fibers in polymer melt.

However, it is very laborious and almost impractical to achieve perfect alignment of discontinuous fibers in LFT composite. In conclusion, there is clear need of innovative composite manufacturing processes which can provide reduced processing complexity, reduced weight, superior crashworthiness, improved efficiency, and compelling cost element.

The study explored the innovative continuous fiber-reinforced thermoplastic (CFRTP) tape overmolding of LFTs as an efficient alternative manufacturing process to further enhance the mechanical performance of LFT composite. The overmolding approach, it uses pre-consolidated CFRTP tapes and LFTs. Pre-consolidated tapes were placed in discrete locations in the mold and followed by LFTs processed via ECM. For the tape overmolding study, PP-GF LFT and PP-GF CFRTP tape was considered to target low-cost automotive applications. The CFRTP tape overmolded LFT samples were characterized using nondestructive and destructive techniques to track fiber alignment, fiber distribution, manufacturing defects, interfacial bonding of the tape – LFT and effect of CFRTP tape on LFT.

The overmolded composite exhibited higher flexural strength (119~142%), flexural modulus (77~65%), Interlaminar shear strength (33~41%), and low velocity impact resistance (288~256%) compared to constituent LFT composite processed via ECM. The overmolding process demonstrated that it could provide numerous advantages such as synergy of constituents, namely LFT and continuous reinforcement, local reinforcement in only needed areas, potential to replace rib and grid structures, ability to enhance damage tolerance and crashworthiness in conjunction with reduced weight and recyclability.

The aerospace industry, civil-infrastructural applications, and high-end cars heavily uses the commingled fibers since it provides higher potential for advanced mechanical performance and ease of molding and processing. Also, there are currently zero overmolded structures used in aerospace structural applications which provides avenues for innovation. Hence the study was further conducted to investigate other forms of continuous fiber reinforcement such as unidirectional and braided commingled fibers for LFT overmolding to target structural applications.

The work considered PA6-CF LFT core overmolded with unidirectional and triaxial (0°/±60°) braided PA6-CF commingled fiber skin to produce sandwich composites. The overmolded sandwich composite samples were characterized using spectroscopic and microscopic techniques to evaluate interfacial bonding of the skin - LFT core. Unidirectional and braided fiber overmolded LFT sandwich composites exhibited higher flexural strength (130%~81%), flexural modulus (192%~94%), tensile strength (169%~125%), and tensile modulus (118%~49%) compared to constituent LFT composite, respectively. Finite element analysis (FEA) using ABAQUS was used to validate the sandwich concept (produced via overmolding technique) in a remote control (RC) airplane wing application. The study concludes that innovative overmolding approach can be used for sandwich fabrication since it provides the ability to tailor stiffness, strength, design freedom, damage tolerance for a broad range of structural applications without considerable increase in weight and compelling cost savings.

In summary, the mechanical, thermal, and microscopic properties of LFT composites can be tailored and enhanced by either aligning the fibers in polymer melt or by overmolding process depending on end-use applications.

Vita

Shailesh Alwekar was born in India. He obtained his Master of Science degree in Physics with Material Science as major from University of Pune, India in 2012. Upon completion of his graduate studies, Shailesh moved to the United States with the goal of pursing a PhD degree. He joined the University of Alabama at Birmingham to purse PhD degree in Materials Science and Engineering in May 2015. Upon learning about Institute for Advanced Composite Manufacturing and Innovation (IACMI) and Dr. Uday Vaidya's group work on advancing composite materials, he transferred his admission to Mechanical, Aerospace and Biomedical Engineering Department at the University of Tennessee, Knoxville in January 2016. He conducts the research in the area of advanced composites under the supervision of Dr. Uday Vaidya in collaboration with the Manufacturing Demonstration Facility (MDF) at Oak Ridge National Laboratory. Shailesh's Primary research focus has been on the development of extrusion compression molded long fiber thermoplastic composites for structural applications.